BODIPY dyes for singlet oxygen and optical limiting applications

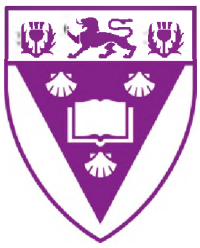

RHODES UNIVERSITY

Where leaders learn

A thesis submitted in fulfilment of the requirements

for the degree of

MASTER OF SCIENCE

of

RHODES UNIVERSITY

by

JESSICA HARRIS

July 2017

You are a child of the universe,
no less than the trees and the stars;
you have a right to be here.
And whether or not it is clear to you,
no doubt the universe is unfolding as it should.

(Max Ehrmann, Desiderata)

Acknowledgements

Firstly, I would like to thank my supervisor, Dr Mack, for the opportunities he has provided me, and for making this project a reality. I would also like to thank my co-supervisor, Prof Nyokong, for her support and encouragement. None of this would have been possible without the two of you.

To Gail Cobus, thank you for the administrative work that goes on behind the scenes, and for choreographing both of my international trips. On that note, I would like to thank Prof Zhen Shen (Nanjing University, China) whose kindness and hospitality will always be remembered. Thanks must also go to Maohu Shi and Lizhi Gai who took me under their wing during my stay in Nanjing, and taught me a great deal about synthetic techniques. Further thanks must go to my hosts in the UK: Prof MacRobert, of the UCL Department of General Surgery and Interventional Sciences, and Dr Nomikou.

Dr Britton, thank you for all you do to keep our laboratory running smoothly. Dr Ngoy, I thank you for all your help in developing both my synthetic and separation skills; for letting me make my own mistakes but being there to help me understand where I went wrong. Marcel Louzada, thank you for letting me pick your brain for everything related to NLO.

I thank my S22 lab mates, especially Muthumuni Managa and Gugu Kubheka: for being such strong role models, for teaching me resilience, and for being as excited about my successes as I am.

To my family and friends who have picked me up and dusted me off along the way, I would not be here without your support and encouragement. Special mention must go to Mark, Anne and Amy Harris, and Charlie O'Donoghue, for their faith and unfailing love and support.

Financial support from the Pearson-Young Memorial Trust is gratefully acknowledged.

Abstract

A series of structurally related BODIPY dyes were synthesised and characterised. Their photophysical properties were studied in order to determine whether they would be suitable candidates for use as photosensitisers in the photodynamic therapy (PDT) treatment of cancer. The synthesis of two highly fluorescent BODIPY cores was achieved via the acid-catalysed condensation of a pyrrole and a functionalised aldehyde. In order to promote intersystem crossing, and hence improve the singlet oxygen generation of these dyes, bromine atoms were added at the 2,6-positions of the BODIPY core. These dibrominated analogues showed good singlet oxygen quantum yields, and excellent photostability in ethanol. In order to red-shift the main spectral bands of the BODIPY dyes towards the therapeutic window, vinyl/ styryl groups were introduced at the 3-, 5-, and 7-positions via a modified Knoevengal condensation reaction. The addition of vinyl/ styryl groups to the BODIPY core caused an increase in fluorescence quantum yield as well as a decrease in singlet oxygen quantum yield with respect to the dibrominated analogues. However, two of the red-shifted BODIPY dyes still showed moderate singlet oxygen quantum yields.

The use of BODIPY dyes in nonlinear optics (NLO) was explored. The nonlinear optical characterisations and optical limiting properties of a series of 3,5-dithienylenevinylene BODIPY dyes were studied, both in dimethylformamide (DMF) solution and when embedded in poly(bisphenol A carbonate) (PBC) as thin films. The 3,5-dithienylenevinylene BODIPY dyes showed typical nonlinear absorption behaviour, with reverse saturable absorption (RSA) profiles, indicating that they have potential as optical limiters. The second-order hyperpolarizability (γ), and third-order nonlinear susceptibility ($Im[\chi^{(3)}]$) values are also reported for these dyes. The optical limiting values of one of the BODIPY dyes in solution, and two of the BODIPY-embedded PBC films, were below the maximum threshold of 0.95 J·cm^{-2}.

The effect of addition of substituents on the electronic structure of the BODIPY dyes was investigated using TD-DFT calculations. The calculated trends closely followed those determined experimentally.

Table of Contents

List of Schemes

List of Figures

List of Tables

List of Symbols

β	Nonlinear absorption coefficient
ε	Molar extinction coefficient
F	Integrated fluorescence emission
γ	Second-order hyperpolarizability
I_{lim}	Optical limiting threshold
$Im[\chi^{(3)}]$	Third-order nonlinear susceptibility
η	Refractive index
$^1O_2$	Singlet oxygen
S_0	Singlet ground state
S_1	First singlet excited state
SDD	Gaussian09 default basis set
Φ_Δ	Singlet oxygen quantum yield
Φ_F	Fluorescence quantum yield
t	Time
T_1	First triplet excited state
τ_F	Fluorescence lifetime
λ	Wavelength

List of Abbreviations

A	Absorbance
Abs	Absorption
B3LYP	Becke 3-Parameter, Lee, Yang and Parr
BODIPY	4,4'-difluoro-4-bora-3a,4a-diaza-*s*-indacene
CAM-B3LYP	Coulomb-attenuating method — Becke 3-Parameter, Lee, Yang and Parr
DCM	Dichloromethane
DDQ	2,3-Dichloro-5,6-dicyano-1,4-benzoquinone
DFT	Density functional theory
DMF	Dimethylformamide
DMSO	Dimethyl sulfoxide
DPBF	1,3-Diphenylisobenzofuran
Em	Emission
ESA	Excited state absorption
EWG	Electron withdrawing group
Exc	Excitation
F	Fluorescence
FT-IR	Fourier transformation Infra-red spectroscopy
HF	Hartree–Fock
HOMO	Highest occupied molecular orbital
HSAB	Hard and soft (Lewis) acids and bases
ISC	Intersystem-crossing
LUMO	Lowest unoccupied molecular orbital
MALDI-TOF	Matrix-assisted laser desorption/ionisation-time of flight
MO	Molecular orbital

MS	Mass spectrometry
NBS	N-bromosuccinamide
Nd:YAG	Neodynium-doped yttrimium aluminium garnet
NLO	Nonlinear optics
NMR	Nuclear magnetic resonance spectroscopy
OL	Optical limiter
P	Phosphorescence
PBC	Poly(bisphenol A carbonate)
Pc	Phthalocyanine
PDT	Photodynamic therapy
RSA	Reverse saturable absorption
r.t.	Room temperature
SA	Saturable absorption
SEM	Scanning electron microscopy
TCSPC	Time-correlated single photon counting
TD-DFT	Time-dependent density functional theory
TEA	Triethylamine
TFA	Trifluoroacetic acid
THF	Tetrahydrofuran
TLC	Thin layer chromatography
TPA	Two-photon absorption
UV/Vis	Ultraviolet/ visible

Chapter 1: Introduction

1.1 BODIPY dyes in photodynamic therapy (PDT)

Highly fluorescent 4,4'-difluoro-4-bora-3a,4a-diaza-*s*-indacene (BODIPY) dyes were first reported by Treibs and Kreuzer in 1968 [1–3]. These dyes possess excellent thermal and photochemical stability, high fluorescence quantum yield, negligible triplet-state formation, intense absorption profile, good solubility, and negligible sensitivity to solvent polarity [2, 4]. However, BODIPYs received relatively little attention until the end of the 1980s [4], when it was demonstrated that they could be used for fluorescence imaging [5]. BODIPYs have also been used extensively as tunable laser dyes [2, 4, 6]. While the strong fluorescence of BODIPY dyes in the visible region makes them suitable for use in these applications, it also limits their efficacy in other applications, such as photodynamic therapy. However, due to the versatility of the fluorophore [2, 4], appropriate structural modifications to the BODIPY core may be employed to yield BODIPY dyes that are suitable candidates for use in photodynamic therapy [2, 7, 8].

1.1.1 Background and working principle

The therapeutic properties of light have been known for thousands of years, with phototherapy being used to treat ailments such as rickets, rheumatism, scurvy and muscle weakness [9, 10]. However, it was only in the last century that photodynamic therapy (PDT) was developed [9–11]. Phototherapy involves the use of light alone for therapeutic purposes [9]. In contrast, PDT requires the presence of three factors: a chemical photosensitiser, light, and oxygen [9, 12, 13]. PDT is a non-invasive method for the treatment of, amongst other things, solid cancer tumours [9–14]. Photosensitisers are typically introduced systemically, via injection into the bloodstream, although some may be applied topically in the treatment of skin cancer [12]. After a period of equilibration, the photosensitiser accumulates in the tumour cells. Thereafter, the tumour region is irradiated with light, leading to excitation of the photosensitiser and the production of cytotoxic singlet oxygen ($^1O_2$). As the photosensitiser accumulates selectively in the tumour, damage to healthy cells is minimised [9]. This is due to the fact that singlet $^1O_2$ can diffuse less than 0.02 µm from the site of production [9, 15]. The localisation of the therapeutic effect makes

PDT very different from conventional cancer treatments such as chemotherapy, which involves damaging both healthy and diseased cells [16].

The first study of the effect of porphyrin photosensitisers on humans was conducted by Meyer-Betz, who injected himself intravenously with haematoporphyrin [9, 10]. Upon exposure to light, a photosensitised reaction occurred, resulting in reddening and swelling of the areas of his body that had been exposed to the light [17]. While considered foolhardy in terms of modern health and safety, this experiment did demonstrate the photodynamic effect of porphyrin sensitisers in human beings [17]. The first light sources used in PDT were noncoherent light sources (e.g. conventional arc lamps) [11]. However, the disadvantages of using conventional lamps include significant thermal effect, low light intensity and difficulty in controlling the light dose. Nowadays, the most commonly used PDT light sources are lasers, which produce high energy monochromatic light of a specific wavelength for a given photosensitiser [11].

PDT involves the use of light exposure to excite a photosensitiser from its ground state (S_0) to its first excited state (S_1). The photosensitiser then undergoes intersystem crossing (ISC) to the triplet excited state (T_1). The longer lifetime of the T_1 state allows for the interaction of the excited photosensitiser with the surrounding molecules [18]. At this stage, two reaction processes involving molecular oxygen may occur. Type I processes result in the production of radicals, which can react with ground state oxygen ($^3O_2$) to produce reactive oxygen species (ROS) such as superoxide anion (O_2^-) and hydrogen peroxide (H_2O_2) [16, 18, 19]. In the second process, Type II, energy from T_1 is transferred directly to $^3O_2$ [18, 20], exciting it to singlet oxygen ($^1O_2$), as illustrated in **Fig. 1** [13, 21]. The singlet oxygen then oxidises DNA in the cancer cell, or reacts with water molecules to form highly reactive oxygen species which collide with the tumour cells, resulting in cell death [22, 23]. Type II is the dominant process in PDT [19] and hence the efficiency of a photosensitiser may largely be determined by calculating its singlet oxygen quantum yield (Φ_Δ) [21, 24].

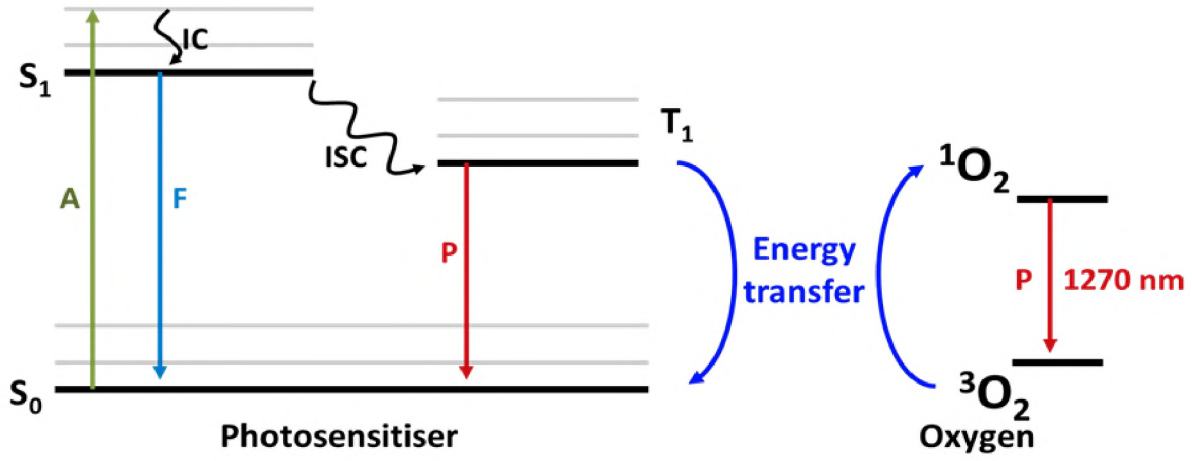

Figure 1. Jablonski diagram showing the mechanism of formation of singlet oxygen ($^1O_2$). When a photosensitiser decays from the T_1 excited state to the S_0 ground state, a quantum-forbidden spin flip is required; spin is conserved by an energy transfer to molecular oxygen present in the tissue, resulting in the production of highly reactive singlet oxygen [20].

1.1.2 Reported photosensitisers and their applications

PDT has been tested in the clinic for use in oncology to treat a variety of cancers [10] and has now reached the level of being an acceptable form of treatment in many countries [9] (**Table 1**). PDT studies have been done for cancers of the head and neck, brain, lung, pancreas, intraperitoneal cavity, breast, prostate and skin [10], which are all – importantly – *solid* tumours. As PDT requires the accumulation of a photosensitiser in a tumour, it cannot be used for cancers of the blood or lymphatic system, or for cancers that have spread extensively; its primary use is for the treatment of localised tumours [10]. Additionally, it can only be used to treat tumours that can be reached using laser light, externally or internally (via endoscope or bronchoscope) as a conventional argon laser can only penetrate about 1 cm into the skin [10].

Porfimer sodium (Photofrin®), a hemtoporphyrin derivative (HpD), was the first photosensitiser to receive approval, and is now licenced for use in the treatment of a number of cancers (**Table 1**). However, it is only moderately active in tissue, as its absorption band in the red region of the visible spectrum is very weak. Photofrin® and other HpD are known as first generation sensitisers

mainly because they exist as complex mixtures of monomeric, dimeric, and oligomeric structures, and the intensity of light absorption at the maximum wavelength is low [19]. The long-term skin phototoxicity lasts six to ten weeks, during which time sunlight and strong artificial light exposure should be avoided [19].

Second-generation synthetic photosensitisers were developed to address the issues of unfavourable skin phototoxicity, low absorption in the red region of the visible spectrum, as well as the complex mixtures arising from synthetic methods. Second-generation photosensitisers have shorter periods of photosensitivity, longer activation wavelengths that allow for deeper penetration of tissue, higher singlet oxygen quantum yields, and better selectivity [12]. The groups that have been most actively investigated are the chlorins, texaphyrins, purpurins, and phthalocyanines. It is worth noting that as of 2013, no non-porphyrin sensitiser had been approved for PDT applications [19]. Porphyrinoid compounds include chlorins, bacteriochlorins, phthalocyanines, and other related structures [19].

Table 1. Properties of some photosensitiser dyes approved for PDT treatment and used in PDT-related clinical trials.

Compound	Trademark	Φ_Δ	Application	Ref
Porfimer sodium	Photofrin®	0.89	Canada (1993) – bladder cancer; USA (1995) – oesophageal cancer; USA (1998) – lung cancer; USA (2003) – Barrett's Oesophagus; Japan – cervical cancer; Europe, Canada, Japan, USA, UK – endobronchial cancer.	[8, 18, 25]
5-Aminolevulinic acid (ALA)	Levulan®	0.56	USA (1999) – actinic keratosis	[16, 18, 19]
Benzoporphyrin derivative monoacid ring A (BPD-MA)	Visudyne	0.78	USA (1999) – age-related macular degeneration	[26, 27]
N-aspartyl chlorin e6 (NPe6)	Laserphyrin, Litx	0.77	Japan (2003) – lung cancer	[19, 28]
Silicon phthalocyanine (Pc4)	-	0.43	Clinical trials – actinic keratosis, Bowen's disease, skin cancer, mycosis fungoides	[16, 19, 29]
Aluminium phthalocyanine tetrasulfonate (AlPcS4)	Photosens	0.43	Russia (2001) – stomach, skin, lips, oral cavity, tongue, breast cancer	[18, 30]

1.1.3 Properties of a good photosensitiser

The ideal PDT photosensitiser has the following characteristics [2, 13, 18, 19]:

(a) available in pure form, of known chemical composition;
(b) synthesisable from available precursors and easily reproduced;
(c) high ISC to triplet state and low fluorescence, to allow for efficient energy transfer to ground state oxygen, for a high singlet oxygen quantum yield (Φ_Δ);
(d) strong absorption in the biological window in the 650–1000 nm region, to allow for deeper penetration of laser light;
(e) high photostability, so the photosensitiser does not degrade upon irradiation;
(f) effective accumulation in tumour tissue and possession of low dark toxicity for both photosensitiser and its metabolites;
(g) stable and soluble in the body's tissue fluids, and easy delivery to the body via injection or other methods;
(h) excreted from the body upon completion of treatment, to avoid long-term light sensitivity.

1.2 4,4'-Difluoro-4-bora-3*a*,4*a*-diaza-*s*-indacene (BODIPY) dyes

BODIPY dyes possess a number of the characteristics of a good photosensitiser: they are isolable in pure form, show good photostability, and have reproducible synthesis. While BODIPY dyes typically possess properties that make them unsuitable for use as photosensitisers, such as high fluorescence quantum yields and spectral bands that lie outside of the therapeutic window, their properties may be tuned by making relatively simple structural modifications.

1.2.1 History and structure

4,4'-difluoro-4-bora-3a,4a-diaza-*s*-indacene (also known as boron-dipyrromethene, BDP or BODIPY) dyes are a class of fluorescent dyes closely related to the porphyrins [2]. The structure of BODIPY dyes is in fact analogous to half a porphyrin molecule, which has resulted in them being referred to as "porphyrin's little sister" (**Fig. 2**) [4]. These highly coloured compounds often

show high fluorescence, and are highly stable [31]. Additionally, their properties are largely independent of solvent polarity [31].

The synthesis of BODIPY dyes was first described by Treibs and Kreuzer in 1968 [1–3]. Following the attempted acylation of 2, 4-dimethyl pyrrole with acetic anhydride using BF_3 as a catalyst, a highly fluorescent product was observed, rather than the desired pyrrole. This product, the BODIPY, arose from the acid catalysed condensation of the two pyrrole units [3]. While the dipyrromethene is not fluorescent, complexation with a boron difluoride unit results in a rigid planar structure that is highly fluorescent due to the low rate of nonradiative decay [2, 32].

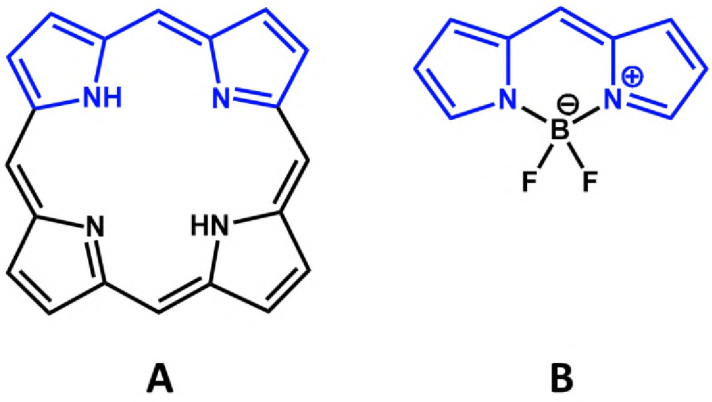

Figure 2. Comparison of the structures of (A) porphyrin and its structural analogue, (B) BODIPY, highlighting the structural similarities.

In 1989, Monsma et al. demonstrated the potential use of BODIPYs dyes for fluorescence imaging of cells [5], which spurred substantial interest in these dyes. Monsma was the first to abbreviate "4,4-difluoro-4-bora-3a,4a-diaza-*s*-indacene" to the now more familiar "BODIPY" [5]. While the spectral properties of the classic BODIPY chromophore are typically limited to the 470–530 nm region, significant red-shifts of the absorption and emission maxima are readily achieved via a variety of structural modifications [2, 31]. The BODIPY core (**Fig. 3**) is particularly versatile [33], and additional structural modifications may be employed to enhance the generation of singlet oxygen, allowing for research into their potential as photosensitisers for photodynamic therapy (PDT) [8, 34, 35].

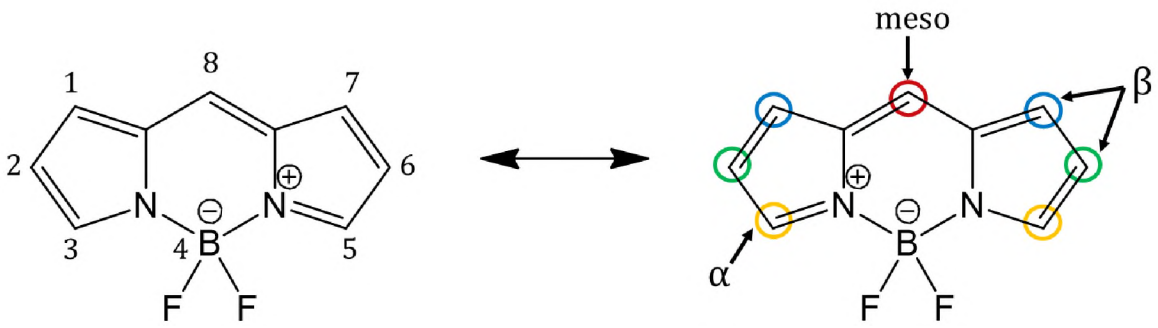

Figure 3. The structure of the BODIPY core and its IUPAC numbering system. Delocalised resonance structures of BODIPY are provided with the formal charges indicated.

1.2.2 Properties of BODIPY dyes

BODIPY dyes display properties similar to those of aromatic π-systems, despite the fact that they do not obey Hückel's rule for aromaticity. This pseudo-aromatic behaviour is due to the fact that, upon coordination of the boron atom, the dipyrromethene ligand is held in a rigid, planar structure [2, 36]. The π-MOs associated with the indacene plane can be compared to those of an aromatic $C_{12}H_{12}^{2-}$ cyclic perimeter, which has MOs arranged in an M_L = 0, ±1, ±2, ±3, ±4, ±5, 6 sequence in ascending energy terms [2, 37, 38]. As the magnetic quantum number (M_L) describes the number of nodal planes present in a given MO, and nodal planes, in turn, are representative of destabilising antibonding character, MO energy increases with increasing M_L [39]. The C_{2V} symmetry of the boron-coordinated dipyrromethene results in a marked lifting of the degeneracies of the MO energies, resulting in the HOMO and LUMO being well-separated from the other π-system MOs [40]. Theoretical calculations predict that the lowest $S_0 \rightarrow S_1$ transition is almost entirely associated with the HOMO → LUMO transition. Experimentally, this results in the absorption spectrum of a BODIPY dye being dominated by a single absorption band. A shoulder is typically observed on the high-energy side of the main absorption band in the 475–485 nm region due to a 01 vibrational transition [2].

The nodal patterns of the HOMO and LUMO of an unsubstituted BODIPY model compound are shown in **Fig. 4**. In order to red-shift the main BODIPY spectral bands, structural changes that

result in the alteration of the energies of the two frontier π-MOs in such a way that the HOMO–LUMO gap is narrowed [2]. If the MO coefficient at a given position is significantly different for the HOMO and LUMO, this will result in the energies of these MOs being affected to different extents upon substitution at this position, providing scope for narrowing the HOMO–LUMO gap.

BODIPY dyes are highly coloured and typically display narrow absorption bands. The intense colour often seen for dilute solutions is because of the high ε_{max} values that tend to be in the range 12 000–110 000 M^{-1} cm^{-1} [33]. BODIPY dyes typically display a small Stokes shift as a result of their rigid structure, which prevents non-radiative decay [32, 41]. The restricted flexibility of the BODIPY core also leads to unusually high fluorescence quantum yields (Φ_F) [31]. This does, however, depend on the substituents present on the BODIPY core; Φ_F values can vary from near zero to almost 1.0 depending on the nature of the substituents on the core, and the chemical environment [32]. The fluorescence lifetime of BODIPY dyes is typically in the single-digit nanosecond ($3–7 \times 10^{-9}$ s) range [42].

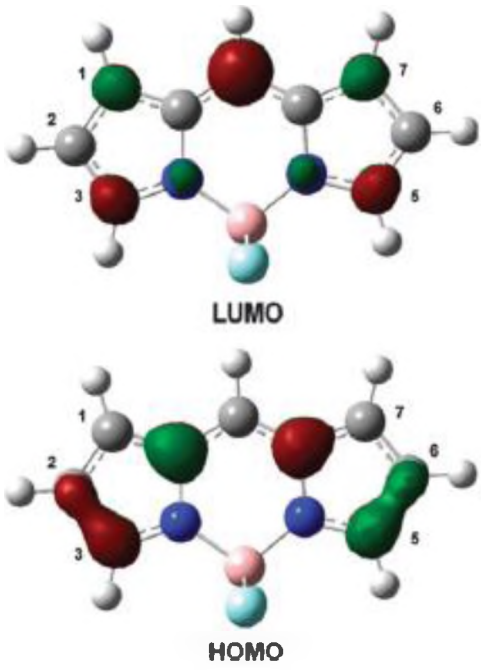

Figure 4. Nodal patterns of the HOMO and LUMO of an unsubstituted BODIPY model compound at an isosurface value of 0.07 a.u. Reprinted with permission from ref. 2. Copyright Royal Society of Chemistry, 2014.

1.2.3 Synthesis and functionalisation of the BODIPY core

BODIPYs are typically formed via condensation reactions between a highly electrophilic carbonyl compound (for example, acid anhydride [1], acyl chloride [32, 43], or aldehyde [32, 44, 45]) and two pyrrole units. The approach used in this work is the acid catalysed condensation of aldehydes with a pyrrole, which is based on chemistry that has been studied extensively in the context of porphyrins [4]. Synthesis of a BODIPY core requires several steps (**Scheme 1**). Initially, the acid-catalysed condensation of an aldehyde and pyrrole results in the formation of a dipyrromethane unit (**Scheme 1 A**). The dipyrromethane is then oxidised using 2,3-dichloro-5,6-dicyano-1,4-benzoquinone (DDQ) or *p*-chloranil to yield the corresponding dipyrromethene (**Scheme 1 B**). As the dipyrromethene is unstable, it is quickly complexed with boron trifluoride diethyl etherate ($BF_3{\cdot}OEt_2$) in the presence of a tertiary amine, such as triethylamine [41], to give a simple BODIPY core (**Scheme 1 C**) [44–48].

While the preparation of the dipyrromethene precursor may be performed in organic solvents (typically DCM) [44, 45], an efficient synthesis of aryldipyrromethanes in water has been described, which yields the aryldipyrromethane product as a precipitate which can then be isolated from the reaction mixture by simple filtration [49]. Substituted pyrroles, such as the dimethyl pyrrole shown in **Scheme 1**, allow for more selective formation of the BODIPY product, as the substituents prevent the polymerisation of the pyrrole units that would result in the formation of tripyrromethane or porphyrin [4].

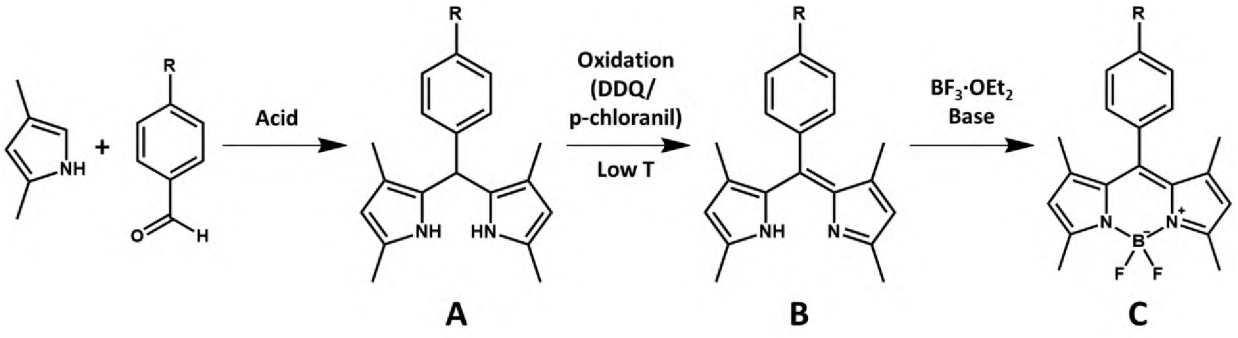

Scheme 1. The acid catalysed condensation of aldehyde with pyrrole for the fabrication of a BODIPY core.

1.2.3.1 Functionalisation *via* the *meso* substituent

In addition to preventing polymerisation of the pyrrole units, the methyl substituents also prevent rotation of phenyl rings at the *meso*-carbon. This restricts the rotation of aromatic groups attached at the 8-position, and the resultant orthogonal geometry serves to minimise electronic coupling between the dye and the *meso*-substituent [4]. Although substitution at the *para*-position of the *meso*-substituent has little effect on the absorption properties of the dye [45], it is ideal for linking with other macromolecules [50, 51], water solubilising groups or nanomaterials [52–54].

The substituent at the 8-position may be readily varied by changing the substituent present on the starting aldehyde [45]. Having a bromine atom at the *para*-position of the *meso*-substituent enables functionalisation at a later stage [55], while in other cases, aldehydes containing the desired functional groups may be used directly [45].

1.2.3.2 Halogenation

Unsubstituted BODIPYs tend to have high fluorescence quantum yields, which is undesirable for PDT applications, as most of the energy absorbed on excitation does not undergo ISC to the triplet state. Consequently, BODIPYs for PDT must be modified to reduce fluorescence and enhance ISC [8]. It has been demonstrated that the spin-selection rule may be relaxed by attaching a halogen atom to the BODIPY core, thus producing BODIPYs that undergo ISC and can generate singlet oxygen [8, 34].

The addition of halogen atoms at the 2,6-positions has also been shown to cause a red shift of the main spectral bands [34, 56]. Although halogen atoms are EWGs, they possess lone pairs of electrons and thus act as resonance donators. When added at the 2,6-positions of the BODIPY core, halogens cause destabilisation of the HOMO with respect to the LUMO, resulting in narrowing of the HOMO–LUMO band gap. The LUMO is not affected by substitutions at these positions due to the fact that they lie along an antinode (**Fig. 4**).

Bromination has been shown to cause a red shift of the BODIPY absorption band, and results in the quenching of fluorescence quantum yield *via* the heavy atom effect [32]. The heavy atom effect may be enhanced by using larger halogen atoms (such as iodine [45, 57]), or by increasing the number of halogen atoms attached to the BODIPY core [58]. However, it has been noted the relationship between the number of halogen atoms and the corresponding effect is in fact nonlinear, with the addition of more than four halogens resulting in no discernible change in the photophysical properties of the BODIPY. [58]. In the absence of steric crowding, the 3,5-positions have been identified as the favoured positions for halogenation, followed by the 2,6- and 1,7-positions respectively. However, due to the blocking effects of 1,3,5,7-tetramethyl substituents, the 2,6-positions are favoured for halogenation in the context of this study [58].

There are three common strategies to achieve the halogenation of a BODIPY core:

i. Incorporation of halogens onto the pyrrole starting material [59];
ii. Incorporation of halogen atoms onto the dipyrrin precursors (only for aza-BODIPYs, whose *meso*-carbon is replaced by a nitrogen atom); and
iii. Direct electrophilic addition of halogen atoms to the BODIPY core *via* exploitation of its electron deficient nature [60], which is the approach used in this work.

1.2.3.3 Substitution of active methyl groups

In order for BODIPYs to be used in biological and medical applications, it is necessary to shift the BODIPY absorbance to the red/NIR region of the spectrum – the "biological window" – where absorption by water, cells and tissues is minimised. Obtaining BODIPY dyes that fluoresce in this region of the spectrum requires the presence of an extended delocalisation pathway [4, 61], which occurs in a highly conjugated system [31, 33, 62].

Due to the presence of unevenly distributed MO coefficients at the 3,5-positions (**Fig. 4**), substitution at these positions has a larger effect on the energy of the HOMO than that of the LUMO. Extending the π-conjugation at these positions causes a net destabilisation of the HOMO with respect to the LUMO, resulting in narrowing of the HOMO–LUMO gap and hence a red-shift of the main absorption band.

The most direct method to extend the delocalisation pathway is to synthesise pyrrole derivatives bearing phenyl, vinyl, or thiophene groups at the 3-position [4, 62, 63]. However, it is also possible to add one or more styryl groups to 1,3,5,7-tetramethyl-BODIPY due to the acidity of the methyl groups [4, 62, 64]. This is achieved by condensation of 3,5-dimethyl-BODIPYs with aromatic aldehydes [32, 62], using a modified Knoevenagel condensation reaction [7, 61, 64]. These reactions normally take place under basic conditions, and require the removal of water from the mixture. This can be done by azeotropic removal of the water by a Dean-Stark apparatus, or by using molecular sieves [64, 65]. This condensation process provides direct access to BODIPY derivatives that have red-shifted fluorescence properties [32, 65].

Substitution at the 3,5-positions is of further interest in this work in terms of providing functionality [32]. The inclusion of functional groups at these positions allows for the possibility of conjugation to nanoparticles [66, 67], which may be exploited for drug delivery. In particular, BODIPYs with sulfur-containing substituents at the 3,5-positions have been used to form BODIPY-gold nanoparticle conjugates, as sulfur and gold have a great affinity for each other based on the HSAB theory [66].

1.2.4 BODIPY dyes synthesised in this work

A series of increasingly complex BODIPY dyes were synthesised from two parent BODIPY cores, **(1)** and **(5)**. BODIPYs **(2)** and **(6)** are substituted at the 2,6-positions with bromine; the presence of these heavy atoms promotes intersystem crossing from the singlet to the triplet excited state by enhanced spin-orbit coupling. The π-conjugation of these dyes was then extended by the inclusion of vinyl/ styryl groups at the 3-, 5-, and 7-positions. **Scheme 2** and **Scheme 3** summarise the structures of the BODIPY dyes synthesised in this work.

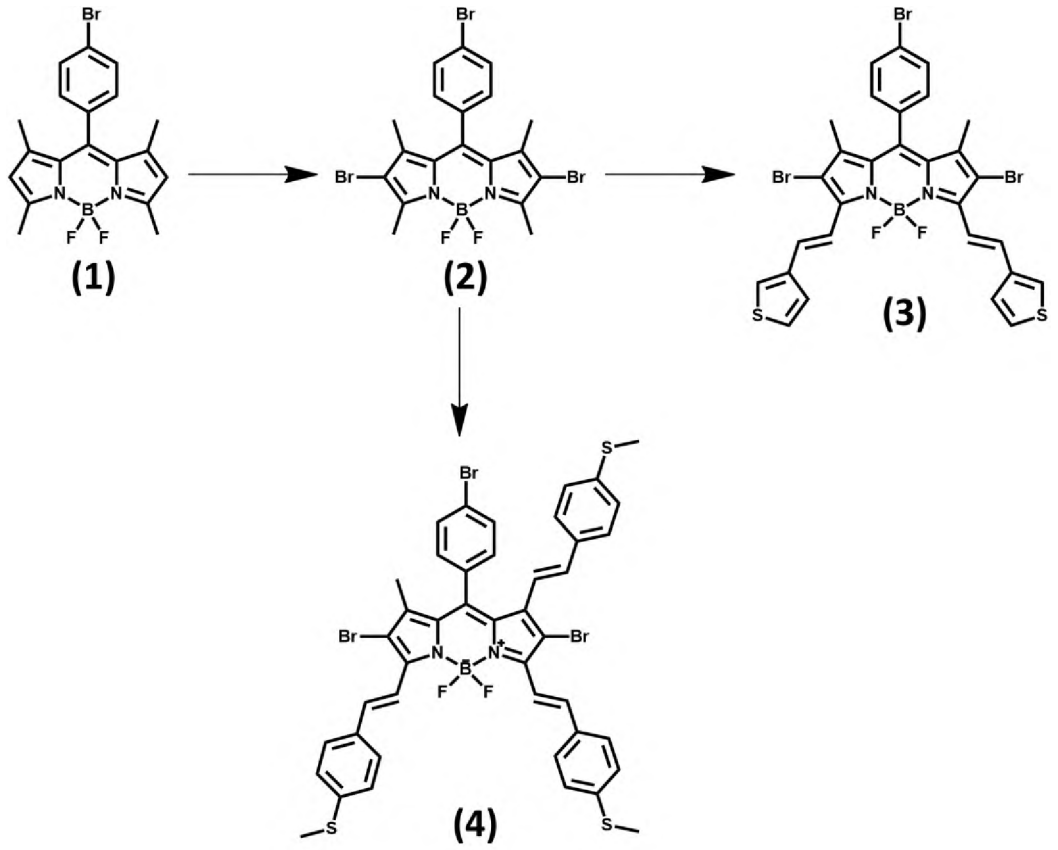

Scheme 2. A series of increasingly complex BODIPY dyes synthesised by first preparing BODIPY **(1)** using 2,4-dimethylpyrrole and 4-bromobenzaldehyde.

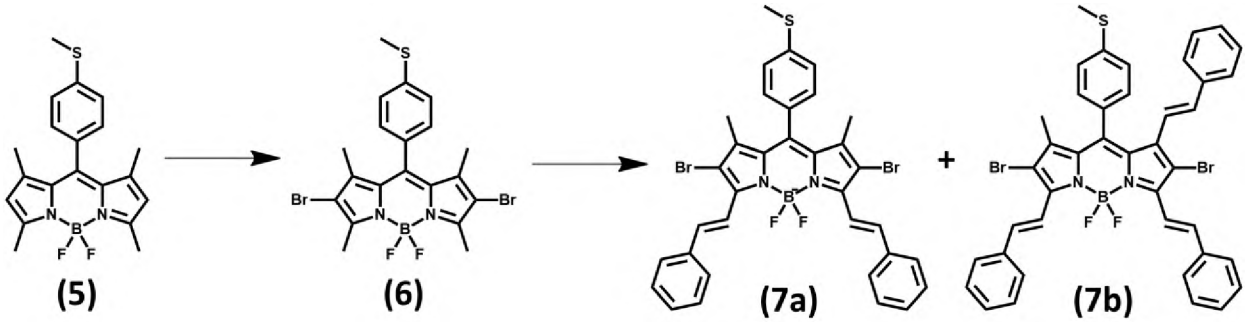

Scheme 3. A series of increasingly complex BODIPY dyes synthesised by first preparing BODIPY **(5)** using 2,4-dimethylpyrrole and 4-(methylthio)benzaldehyde.

1.3 BODIPY dyes in nonlinear optics (NLO)

Nonlinear optics (NLO) is a branch of physics that is concerned with changes in the optical properties of materials upon irradiation with light of varying intensities. Optical limiting (OL) is a research area of applied NLO, intended for the development of techniques to protect human eyes and other optical sensors from high-intensity laser irradiation [68, 69]. Optical limiters exhibit decreasing transmittance as a function of intensity and so, upon exposure to high intensity light such as that from a laser, attenuate the intensity, allowing only a beam of safe intensity to pass through (**Fig. 5**) [69]. Hence, optical limiting devices can be used to protect human eyes and other optical sensors from high-intensity laser irradiation [68–71].

Coloured safety goggles used for laser safety in laboratories act as filters, completely blocking out all light of a certain wavelength. An ideal optical limiter differs from a filter in that is transparent to normal, safe intensity light and only restricts high-intensity light that may cause damage. An ideal optical limiter allows for the linear transmittance of low-intensity light up to a limiting intensity, I_{lim}, but thereafter serves to attenuate the intensity (**Fig. 6**) *via* a number of NLO mechanisms. Hence, only a reduced intensity is successfully transmitted. An ideal optical limiter would have some critical intensity or threshold at which the transmittance changes abruptly, effectively clamping the output at some value that would presumably be less than the amount required to damage the sensor [72]. However, in most cases, the limiting does not occur with a sharp threshold as indicated by **Fig. 6** but changes gradually from high to low transmittance [70, 72].

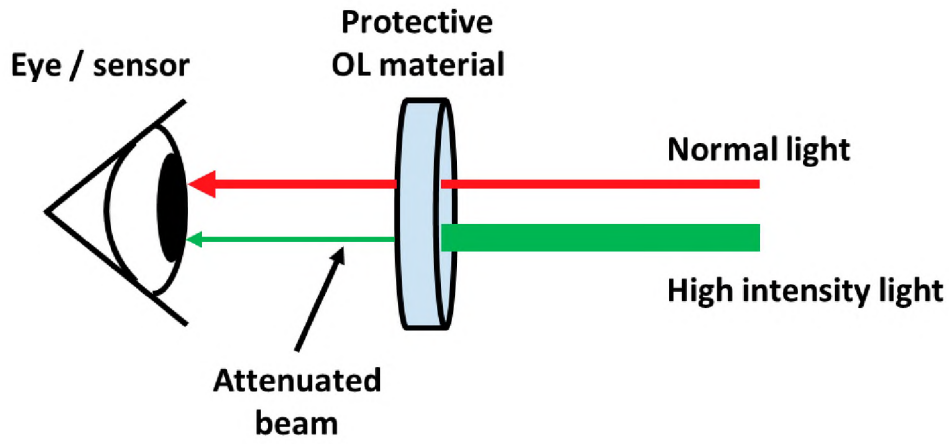

Figure 5. Schematic representation of the ideal functioning of an optical limiting material under normal and high-intensity light.

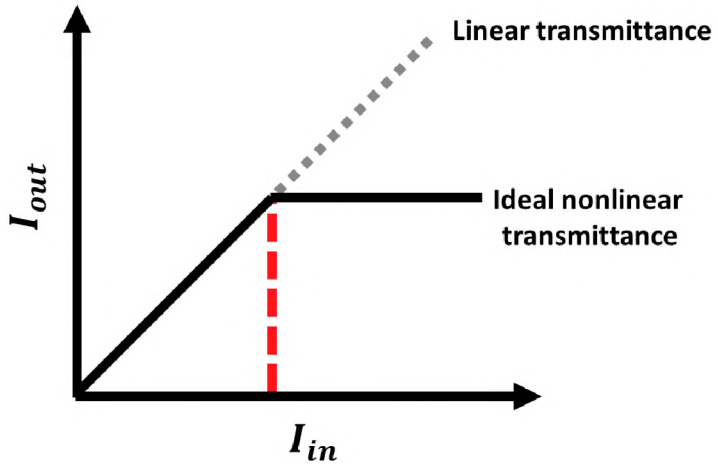

Figure 6. The response of an ideal optical limiter. The point at which the transmittance deviates from linearity is known as the limiting intensity (*dashed red line*). I_{in} and I_{out} are incident and transmitted intensities, respectively.

Optical limiting devices fall into one of two general categories: active or passive. Active OL devices often involve the use of moving parts in order to regulate the amount of light. Typically, active optical limiters rely on an internal feedback mechanism: an increase in intensity is detected, triggering a response which then results in physical changes that result in regulation of the intensity [70]. In these types of devices, the thermally-induced change in refractive index often plays a major role [68]. However, a system that relies on heating to change the optical properties is problematic, as the heat generated may cause irreparable damage before the optical change has become effective [68].

Passive optical limiters, on the other hand, rely on the nonlinear absorption properties of a given material. This mechanism does not involve the use of any feedback systems and is instead reliant on the fact that some nonlinearly absorbing materials respond by decreasing transmissivity when input laser intensity is increased [68]. Hence, passive OL devices have the advantage of an extremely fast response time, as the OL response is dependent on the physical properties of a material and not on the response time of moving parts [70]. This making passive optical limiters more suitable for the purpose of protecting sensitive detectors and eyes.

A number of organic dyes, including phthalocyanines (Pcs), have been investigated for use in optical limiting due to their inherent nonlinear absorption properties [73–76]. Macrocyclic complexes such as Pcs and their derivatives have been of interest in NLO applications due to their extended π-electron systems, which allow for delocalisation of electrons and hence polarisation [77]. Strong nonlinearities in organic molecules usually arise from highly delocalised π-electron systems [77, 78], and the highly conjugated structures of Pcs and their analogues allow for rapid charge redistribution upon interaction with intense laser radiation [75]. Furthermore, modifications of the Pc that reduce the symmetry serve to increase the polarizability of the compound [78]. Phthalocyanines containing metal centres with higher oxidation numbers can be axially substituted with a range of ligands; the axial group induces asymmetry, providing the molecule with an axial dipole moment [78]. A similar effect is observed for Pcs with large central metals that exist in a shuttlecock arrangement, as the metal is too large to fit in the cavity [74]. These axially-substituted, and shuttlecock Pcs have reduced symmetry (C_{4v}) compared to Pcs with

smaller metal centres that lie in the plane (D_{4h} for symmetrically substituted Pcs) (**Fig. 7**) [79]. It would then seem that using an organic dye with even lower symmetry might result in enhanced nonlinear absorption. As BODIPYs have a C_{2V} symmetry and are hence intrinsically lower in symmetry than Pc, they might prove to be strong candidates for use in optical limiting. However, comparatively little research has been done regarding the nonlinear optical behaviour of BODIPY dyes (**Table 2**).

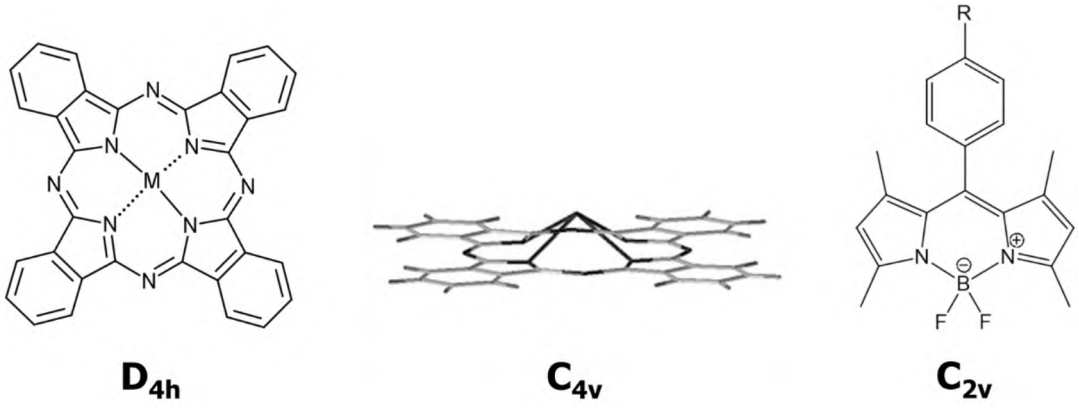

Figure 7. Structures and symmetries of a planar phthalocyanine (D_{4h}), a phthalocyanine in shuttlecock arrangement (C_{4v}) and a BODIPY (C_{2V}).

Table 2. BODIPY dyes whose nonlinear properties have been reported in the literature.

BODIPY	Method	Solvent/ matrix	NLO behaviour	λ /nm	Ref
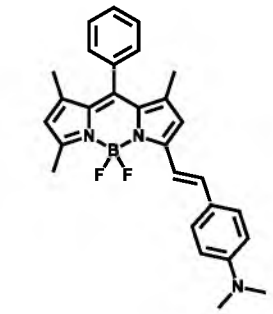	Z-scan	THF	RSA	532	[80]
	Second harmonic generation response: Rotational Maker fringe technique Third harmonic response: Comparative model	Polymethyl-methacrylate (PMMA) thin film		1064	[81]
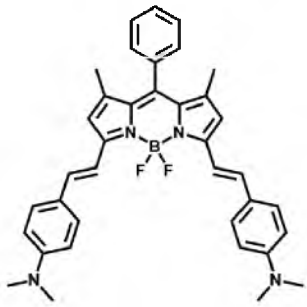	Z-scan	THF	RSA	532	[80]
	Second harmonic generation response: Rotational Maker fringe technique Third harmonic response: Comparative model	Polymethyl-methacrylate (PMMA) thin film		1064	[81]
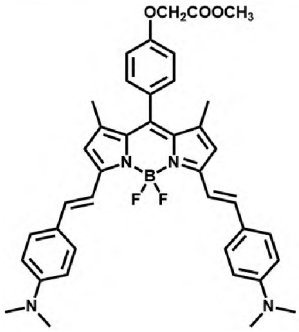	Direct nonlinear transmission method (NTM) in femto-second (fs) regime	DCM	RSA	1310	[82]
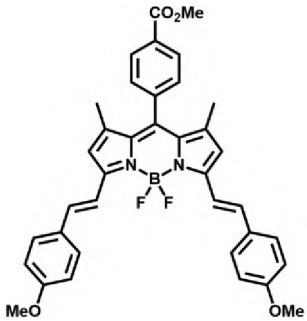	Optical and photoacoustic Z-scan	Acetonitrile	RSA	532	[83]

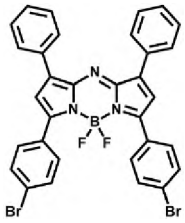	fs-Z-scan	DCM	No TPA response	1200 – 1600	[84]
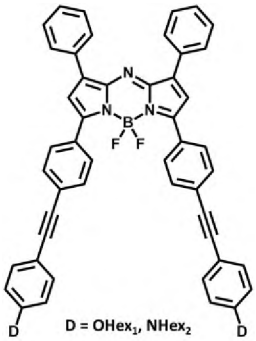	fs-Z-scan	DCM	RSA, TPA	1200 – 1600	[84]
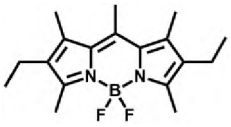	Z-scan	DCM	Saturable absorption (SA)	532, 1064	[85]
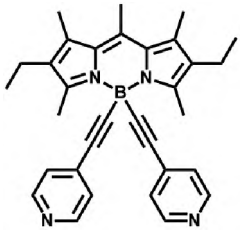	Z-scan	DCM	SA	532, 1064	[85]
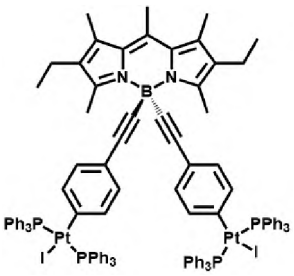	Z-scan	DCM	SA	532, 1064	[85]
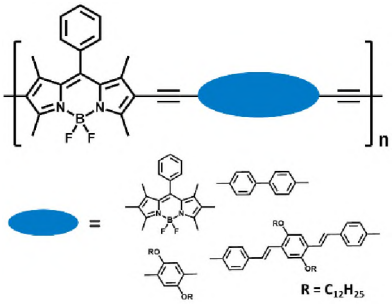	Z-scan	Toluene	RSA	532	[86]

1.3.1 Mechanisms in optical limiting

Nonlinear absorption, nonlinear scattering and nonlinear refraction (**Fig. 8**) are the main processes that contribute to passive optical limiting, with most OL devices generally employing a combination thereof. Nonlinear refraction occurs due to several diverse physical effects, including thermal lensing, while nonlinear scattering may play the biggest role for optical phenomena involving nanomaterials [87]. This study focuses on determining OL activity due to nonlinear absorption. Nonlinear absorption itself can occur due to a combination of processes, including two-photon absorption (2PA) and excited state absorption (ESA) (**Fig. 9**).

Nonlinear absorption refers to the change in transmittance of a material as a function of intensity or fluence. At sufficiently high intensities, the probability of a material absorbing more than one photon before relaxing to the ground state can be significantly enhanced, resulting in population redistribution [72]. This is manifested optically in a reduced (saturable) or increased (reverse saturable) absorption [72]. RSA describes materials that behave as optical limiters, and occurs when the excited state absorption cross section of a material is greater than its ground state absorption cross section [88].

Two photon absorption (2PA) occurs when 2 photons are absorbed simultaneously by a molecule (**Fig. 9**). The use of a femtosecond laser pulse would allow for specific determination of the 2PA but because a longer pulse was used (τ = 10 ns), there could technically be more than 2 photons involved. Hence, multiphoton absorption is considered; multiphoton absorption refers to the simultaneous absorption of *n* photons [72]. On the other hand, excited state absorption (ESA) occurs when an excited electron is promoted to a higher-lying state before relaxing back to the ground state (**Fig. 9**) [72]. For BODIPYs that undergo intersystem crossing (ISC) to the triplet excited state, ESA may occur in the triplet manifold (**Fig. 9 A**). However, this cannot be the optical limiting mechanism for BODIPYs without halogen substituents to promote ISC. For these unhalogenated BODIPYs, OL activity is likely due to ESA in the singlet manifold (**Fig. 9 B**).

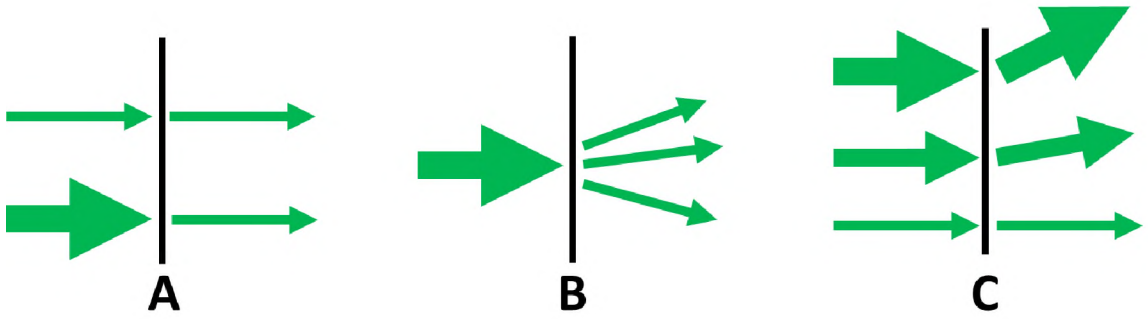

Figure 8. The nonlinear processes which result in OL activity: (A) nonlinear absorption, (B) nonlinear scattering and (C) nonlinear refraction.

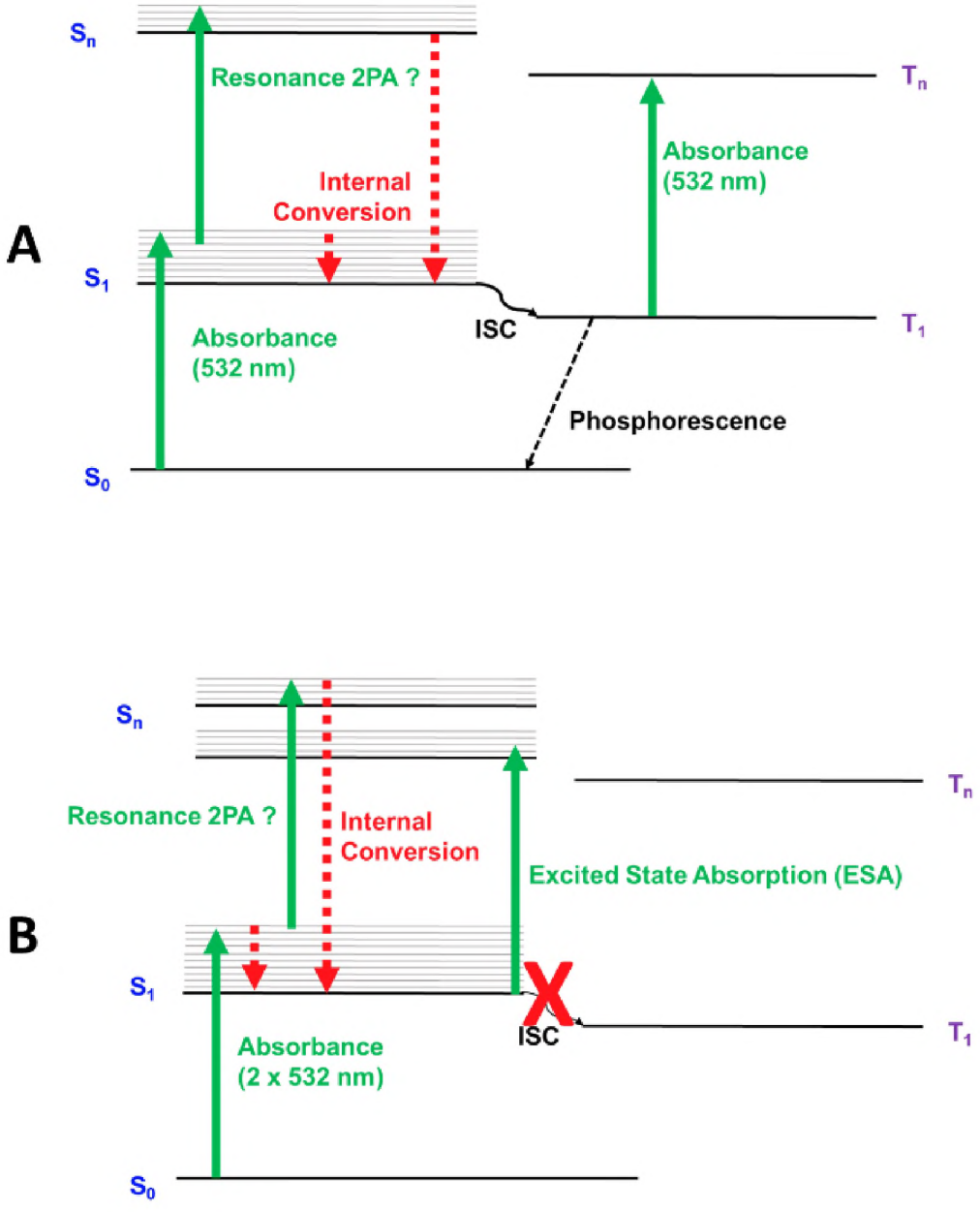

Figure 9. Jablonski diagrams showing potential mechanisms for (A) BODIPYs with halogens at the 2,6-positions that are likely to have a populated triplet excited state and (B) non-halogenated BODIPYs that do not undergo intersystem crossing to the triplet excited state.

1.3.2 Optical limiting parameters (z-scan technique)

Optical limiting (OL) parameters can be determined using simple and sensitive single-beam z-scan experiments according to the methods described by Sheik-Bahae [89–91]. Using a closed-aperture setup, as shown in **Fig. 10**, information about the nonlinear refractive and nonlinear absorptive properties of a material can be extracted. In short, the sample is moved along the z direction of a focussed Gaussian beam while the pulsed laser is held fixed (**Fig. 10**). The resultant plot of transmittance through an aperture in the far field yields a dispersion-shaped curve from which the nonlinear refractive index is easily calculated [90]. The nonlinear absorption may be separately evaluated by performing a second z-scan with the aperture removed [70, 90]. In this work, only the nonlinear absorptive properties were under consideration and hence an open aperture setup was employed.

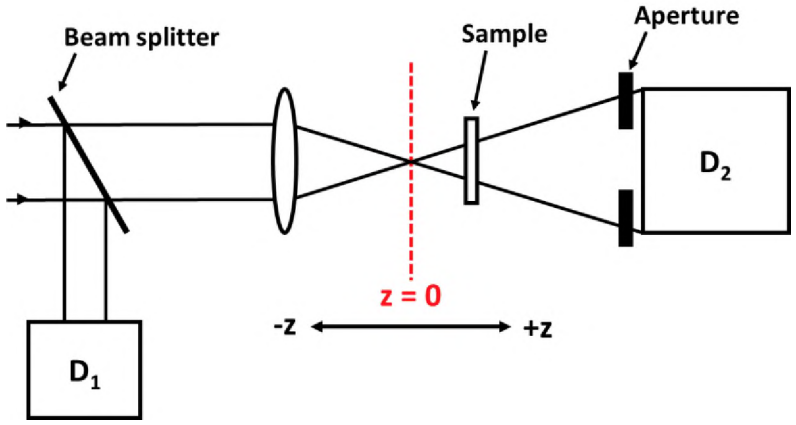

Figure 10. Schematic diagram of z-scan experimental apparatus in which the transmittance ratio D_2/D_1 is recorded as a function of the sample position, z.

The measured quantity in an open-aperture z-scan experiment is the normalised transmittance, given by **Equation 1** [90, 92] for a Gaussian pulse.

$$T(z) = \frac{1}{\sqrt{\pi} q_0(z)} \int_{-\infty}^{\infty} \ln[1 + q_0(z)\, e^{-\tau^2}] d\tau \qquad (1)$$

where $q_0(z)$ is a parameter characterising the strength of the nonlinearity and is given by **Equation 2** when using a circular Gaussian beam [90, 92].

$$q_0(z) = \frac{2\beta P_0 L_{eff}}{\pi w^2(z)} \quad (2)$$

where β is the nonlinear absorption coefficient of the material, P_0 is the peak power of the pulses and L_{eff} is the effective path length in the sample of length L, given by **Equation 3**:

$$L_{eff} = \frac{1-e^{-\alpha L}}{\alpha} \quad (3)$$

where α is the linear absorption coefficient (cm^{-1}). For applications of these materials, α should always be measured at the intended wavelength [93]: in this case, 532 nm. In **Equation 2**, $w(z)$ is the beam width as a function of the sample position, and is given by [69]

$$w(z) = w_0 \cdot \sqrt{1 + \left(\frac{z}{z_0}\right)^2} \quad (4)$$

where w_0 is the beam waist at the focus ($z = 0$), defined as the distance from the beam centre to the point where the intensity reduces to $1/e^2$ of its axis value; while z and z_0 are the translation distance of the sample relative to the focus, and Rayleigh length, respectively. The Rayleigh length is defined as $\pi w_0^2 / \lambda$ where λ is the wavelength of the laser. **Equations 1–4** are used to determine the nonlinear absorption coefficient (β) from experimentally measured normalised transmittance. Tsigaridas et al. [92] have produced an analytical formula given by **Equation 5**:

$$q_0(z) = \begin{cases} a_0 + a_1 T(z) + a_2 T^2(z) + a_3 T^3(z) \ \ for \ \ T(z) \leq 0.75 \\ c_0 + c_1 [T(z)]^{c_2} \ for \ T(z) \geq 0.75 \end{cases} \quad (5)$$

where the coefficients $a_0, a_1, a_2, a_3, c_0, c_1$ and c_2 for Gaussian pulses are given as 15.66, -37.45, 30.76, -8.97, -2.301, 2.156 and -1.563 respectively [92]. **Equation 5** provides values of $q_0$directly from the normalised transmittance $T(z)$. Substituting **Equation 4** into **Equation 2** gives $q_0(z)$ as follows:

$$q_0(z) = \frac{Q_0}{1+\left(\frac{z}{z_0}\right)^2} \quad (6)$$

where

$$Q_0 = \frac{2\beta P_0 L_{eff}}{\pi w^2(z)} = \frac{2\beta P_0 L_{eff}}{\lambda z_0} \quad (7)$$

Equation 5 gives a Gaussian plot with Q_0 as the maximum value at the beam waist ($z = 0$). The peak value and the FWHM of the plot give values of Q_0 and z_0 respectively. The nonlinear absorption coefficient (β) may then be calculated using **Equation 8** [92].

$$\beta = \frac{\lambda z_0 Q_0}{2P_0 L_{eff}} \quad (8)$$

The imaginary component of the third order susceptibility, $Im[\chi^{(3)}]$, is directly proportional to β, as seen in **Equation 9**:

$$Im[\chi^{(3)}] = \frac{\eta^2 \varepsilon_0 c \lambda \beta}{2\pi} \quad (9)$$

where η and c are the linear refractive index and speed of light, respectively, and ε_0 is the permittivity of free space. The terms λ and β are described above. The third-order nonlinear optical susceptibility is used to describe ultrafast responses [70], with nonlinear absorption being described by the imaginary component, while the real component is representative of the nonlinear refraction of the material. Values of $Im[\chi^{(3)}]$ reported for BODIPYs in literature range from 10^{-11} – 10^{-13} esu [85], which is comparable to those reported for Pcs [94]. While $Im[\chi^{(3)}]$ describes the response of the material, the behaviour at a molecular level may be described using hyperpolarizability (γ), which describes the nonlinear absorption per mole of the OL compound, and is useful when comparing efficiencies of different optical limiters. The correlation between $Im[\chi^{(3)}]$ and γ is shown in **Equation 10:**

$$\gamma = \frac{Im[\chi^{(3)}]}{f^4 C_{mol} N_A} \quad (10)$$

where N_A is Avogadro's constant, C_{mol} is the concentration of the active species in the triplet state per mole, and f is the Lorentz local field factor, $f = (\eta^2 + 2)/3$ [95]. Values of γ reported in literature for organic molecules are on the scale of 10^{-29} – 10^{-34} esu [85, 96].

The limiting intensity (I_{lim}) is a threshold intensity/ fluence at which the transmittance is 50 % of the linear transmittance [75, 97]. It is possible to approximate the value of I_{lim} experimentally,

using a plot of output fluence (I_{out}) vs input fluence (I_{in}). While there is currently no defined optimal range for I_{lim} values, it makes sense that a good optical limiter would be those compounds exhibiting lower I_{lim} values, as this means that the limiting would occur at a lower intensity, allowing for more cautious protection of sensors. As a guideline on limits of exposure to radiation, the International Commission on Non-Ionising Radiation Protection has published a guideline [98] giving insight into exposure limits for a variety of lasers. This work deals with 10 ns laser pulses from the second harmonic of an Nd:YAG laser at 532 nm and, as such, its exposure limit can be determined from **Equation 11**, which gives the exposure limit as a function of time.

$$2.7\ C_A t^{0.75}\ \mathrm{J/cm^2} \tag{11}$$

C_A is a correction factor (= 1 for lasers with wavelengths of 400–700 nm). For this work, the exposure limit was determined to be 0.95 J/cm^2 assuming a 0.25 s exposure time. This exposure time was selected as it is the average human response time (blink reflex) to a sudden flux of light into the eye [76].

Fluence has units of W/cm^2, with the maximum fluence occurring at the focus ($z = 0$). The maximum fluence may be calculated using **Equation 12**.

$$I_{00} = \frac{E}{\tau \cdot \pi \cdot {w_0}^2} \tag{12}$$

where E is maximum laser energy (J), τ is the length of the laser pulse (s) and w_0 is beam waist (cm). Note that π is unitless. As $1\,J/s = 1\,W$, the maximum fluence has units of $\frac{W}{cm^2}$. For any given z-scan experiment, the laser energy (J) remains constant. Hence, the overall laser power ($J/s = W$) remains constant. However, the fluence $\left(\frac{W}{cm^2}\right)$ will vary with z, as the beam width depends on the distance from the focus. The cross-sectional area of the beam is circular and hence equal to $\pi \cdot w(z)^2$. Multiplying the fluence by the corresponding beam area gives the laser power, P. At the focus ($z = 0$), P is given by **Equation 13**.

$$P = I_{00} \cdot \pi w_0^2 \tag{13}$$

At any other z position, P is given by **Equation 14**.

$$P = I_{in}(z) \cdot \pi w(z)^2 \quad (14)$$

As P remains constant throughout any given z-scan run, **Eq. 13** and **Eq. 14** may be combined and simplified as shown in **Equation 15**:

$$I_{in}(z) = I_{00} \cdot \left(\frac{w_0}{w(z)}\right)^2 \quad (15)$$

As the transmittance gives the percentage of light that passes through a material, the output fluence $(I_{out}(z))$ may be calculated by finding the product of $I_{in}(z)$ and the transmittance corresponding to each z position $(T(z))$ (**Equation 16**).

$$I_{out}(z) = I_{in}(z) \cdot T(z) \quad (16)$$

1.3.3 BODIPY dyes used in this work for NLO studies

The NLO properties of four 3,5-dithienylenevinylene BODIPY dyes were investigated. These dyes have increased π-conjugation due to substitution with thiophene-containing groups at the 3,5-positions. BODIPY **(3)** was synthesised in this work, while purified samples of BODIPYs **(8–10)** were provided by Dr. Lizhi Gai and Prof. Zhen Shen of Nanjing University. BODIPYs **(3)** and **(10)** are substituted at the 2,6-positions with bromine and iodine, respectively. The presence of these heavy atoms promotes intersystem crossing from the singlet to the triplet excited state by enhanced spin-orbit coupling. BODIPY **(3)** is substituted with 3-thiophene groups at the 3,5-positions of the BODIPY core, while BODIPYs **(8–10)** are substituted with 2-thiophene groups at these positions. **Fig. 11** summarises the structures of the 3,5-dithienylenevinylene BODIPY dyes employed in this study.

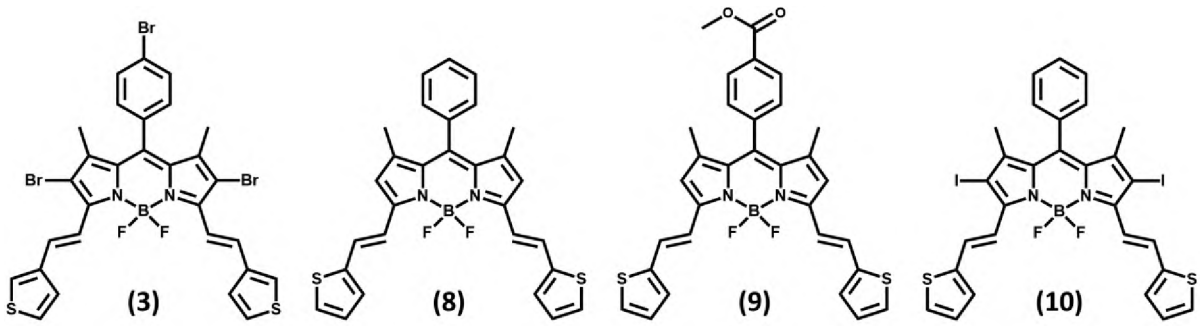

Figure 11. BODIPY dyes used in this work for NLO studies.

1.3.4 Thin films

Although the use of solutions is convenient for investigating the optical limiting properties of compounds, for the purpose of application it is necessary for the OL materials to be cast in the solid state [99]. Practically, these compounds will have to be incorporated into safety visors or Perspex™ windshields in order to be applicable in real world situations. Hence, BODIPYs **(3)**, **(8)**, **(9)** and **(10)** were embedded in polymer thin films for NLO studies [74, 100]. In this work, the polymer chosen was poly(bisphenol carbonate A) (PBC) (**Fig. 12**). Polycarbonates have been used for making safety visors [101], as well as in the manufacture of eyewear, protective sportswear and other safety products [74].

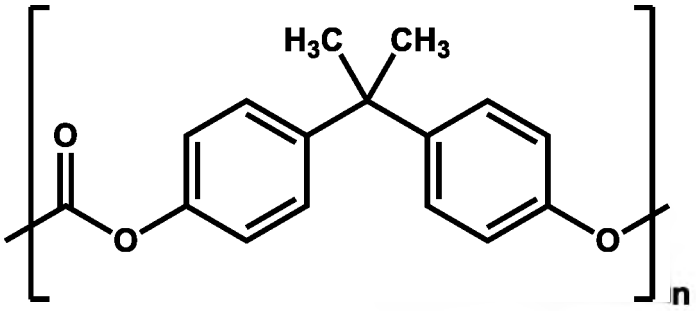

Figure 12. The structure of a unit of poly(bisphenol carbonate A) (PBC).

1.4 Summary of aims

The aim of this work is the synthesis of red-shifted, singlet oxygen-producing BODIPY dyes that have the potential to be used in PDT applications. However, unsubstituted BODIPY dyes are typically highly fluorescent, and have main spectral bands in the region of ca. 500 nm. Hence, some structural modifications must be implemented in order to produce BODIPY dyes that are suitable for use in PDT: firstly, the addition of bromine atoms at the 2,6-positions of the BODIPY core reduces the fluorescence quantum yield of the BODIPY and increases its ability to generate singlet oxygen. Secondly, the π-delocalisation must be extended by substitution at the acidic methyl groups present at the 1-,3-,5-,7-positions of the BODIPY core, causing a red-shift of the main spectral bands of the BODIPY dye to within the biological window. BODIPYs with sulfur-containing substituents may be used for attachment to gold nanoparticle drug carriers. Hence, 4-(methylthio) or 3-thiophene groups were included in the structures of the target BODIPYs.

The use of BODIPYs in nonlinear optics is also investigated, as an alternative application for these dyes. As BODIPY dyes have an inherently lower symmetry than their porphyrin and phthalocyanine counterparts and can, with suitable modification, possess a highly-conjugated π-electron system, they could be strong candidates for use in optical limiting.

The aims of this thesis are summarised below:

1. Synthesis, characterisation and photophysicochemical studies of a series of BODIPY dyes with increasing complexity, with a special focus on the position of their absorption maxima, and their ability to generate singlet oxygen.

2. A study of the nonlinear optical behaviour of four 3,5-dithienylenevinylene BODIPYs in solution and embedded in PBC as thin films.

3. Modelling of BODIPYs for (i) PDT and (ii) NLO to better understand the structure–property relationships of these compounds.

Chapter 2: Experimental

Equipment, Materials, Synthesis and Methods

2.1 Equipment

1. Ground state electronic absorption spectra were performed on a Shimadzu UV-2550 spectrophotometer.
2. Fluorescence excitation and emission spectra were recorded on a Varian Eclipse fluorescence spectrofluorimeter.
3. Elemental analyses for CHNS were done using a Vario-Elementar Microcube ELIII Series.
4. Mass spectral data were collected with a Bruker AutoFLEX III Smartbeam TOF/TOF Mass spectrometer. The instrument was operated in positive ion mode using an m/z range of 400 – 3000 amu. The voltage of the ion sources was set at 19 and 16.7 kV for ion sources 1 and 2 respectively, while the lens was set at 8.50 kV. The reflector 1 and 2 voltages were set at 21 and 9.7 kV respectively. The spectra were acquired using α-cyano-4-hydroxycinnamic acid as the MALDI matrix and a 354 nm nitrogen laser as the ionising source.
5. ^{1}H-nuclear magnetic resonance spectra (^{1}H -NMR) were recorded in deuterated solvents ($CDCl_3$, Acetone-d_6 or THF-d_8) using Bruker AMX600 MHz spectrometer.
6. Fourier Transform Infrared (FT-IR) spectra were recorded on a Perkin Elmer Spectrum 100 FT-IR spectrometer.
7. Fluorescence lifetimes were measured using a FluoTime 300 'EasyTau' spectrometer (PicoQuant GmbH) using a time-correlated single photon counting (TCSPC) technique. BODIPYs **(1)**, **(2)**, **(5)**, and **(6)** were excited at 485 nm using a LDH-P-C-485 laser head driven by PDL 800-B single channel driver (10 MHz repetition rate), while red-shifted BODIPYs **(3)**, **(4)**, **(7a)** and **(7b)** were excited at 670 nm with a diode laser (LDH-P-670, 20 MHz repetition rate, 44 ps pulse width, PicoQuant GmbH). A monochromator with a spectral width of about 8 nm was used to select the required emission wavelength band. The response function of the system, which was measured with a scattering Ludox solution (DuPont), had a full width at half-maximum (FWHM) of about 300 ps. All luminescence decay curves were measured at the maximum of the emission peak. The fluorescence

lifetimes were obtained by deconvolution of the decay curves using the FluoFit Software program (PicoQuant GmbH, Germany).

8. Photo-irradiation for determination of singlet oxygen quantum yields (Φ_Δ) was done using a tunable laser system consisting of a Quanta-Ray Nd:YAG laser (532 nm, 400 mJ, 9 ns pulses at 10 Hz) pumping an Ekspla NT-342B-20-AW laser equipped with an optical parametric oscillator (OPO) system (0–7 mJ), with a wavelength range of 420–2300 nm. Solutions of sensitiser (absorbance of ca. 0.5 at the irradiation wavelength) containing DPBF were prepared in the dark and irradiated using the setup described above. Degradation of the DPBF peak was monitored. For red-shifted samples whose crossover with the standard occurred at wavelengths above 660 nm, the laser setup used for singlet oxygen determination was a Nd:YAG laser pumping a Lambda-Physik FL3002 dye laser (Pyridin 1 dye in methanol), with a pulse period of 7 ns and repetition rate of 10 Hz.
9. The film thickness and morphology were determined by the TESCAN Vega TS 5136LM scanning electron microscopy (SEM) instrument.
10. All Z-scan experiments described in this study were performed using a frequency-doubled Nd:YAG laser (Quanta-Ray, 1.5 J /10 ns FWHM pulse duration) as the excitation source. The laser was operated in a near Gaussian transverse mode at 532 nm (second harmonic), with a pulse repetition rate of 10 Hz and energy range of 0.1 μJ – 0.1 mJ, limited by the energy detectors (Coherent J5-09). The low repetition rate of the laser prevents cumulative thermal nonlinearities. The beam was spatially filtered to remove the higher order modes and tightly focused with a 15 cm focal length lens. No damage was detected between runs since the sample was moved or replaced (**Fig. 13**).

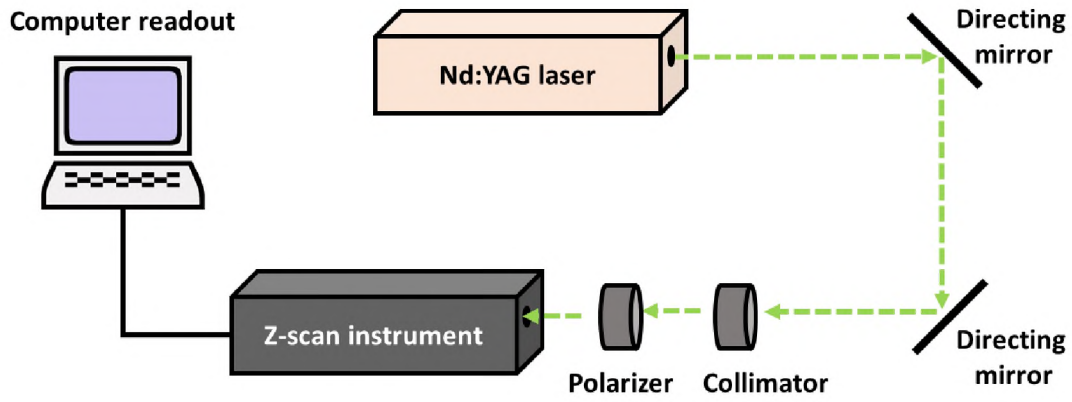

Figure 13. Schematic diagram of laser setup for z-scan.

11. The Gaussian 09 software package [102] running on an Intel/Linux cluster was used to perform all calculations. Geometry optimisations were carried out at the B3LYP level of theory with SDD basis sets. TD-DFT calculations employed the CAM-B3LYP level of theory with SDD basis sets. Avogadro [103, 104] was used for all visualisations of molecular orbitals.

2.2 Materials

Benzaldehyde, trifluoroacetic acid (TFA), triethylamine (TEA), boron trifluoride diethyl etherate ($BF_3{\cdot}Et_2O$), N-bromosuccinimide (NBS), 4-(methylthio)benzaldehyde, 3-thiophenecarboxaldehyde, benzene, Rhodamine 6G and zinc phthalocyanine were purchased from Sigma Aldrich. 4-Bromobenzaldehyde, 2, 4-dimethylpyrrole and p-chloranil (tetrachloro-1,4-benzoquinone) were obtained from Aldrich. Piperidine was purchased from Riedel-de Haen AG. Poly(bisphenol A carbonate) (PBC) and Bengal Rose B were obtained from Fluka Chemika. Hydrochloric acid (HCl, 32 %), glacial acetic acid, DCM, ethyl acetate, petroleum ether and hexane were obtained from local suppliers.

2.3 Photophysical and Photochemical Methods

2.3.1 Fluorescence quantum yield (Φ_F)

Fluorescence quantum yield (Φ_F) is defined as the number of photons emitted relative to the number of photons absorbed. The fluorescence quantum yield of the BODIPY dyes and their conjugates were obtained using the comparative method, using **Eq. 17** [105]:

$$\phi_F = \phi_{F(std)} \frac{F \cdot A_{std} \cdot \eta^2}{F_{std} \cdot A \cdot \eta_{std}^2} \quad (17)$$

where F and F_{std} are the integrated fluorescence intensities of the BODIPY dye and the standard, respectively. The integrated fluorescence intensity is equal to the area beneath a fluorescence emission curve. A and A_{std} are the absorbances of the samples and standard respectively. ZnPc (Φ_F in DMSO = 0.20 [106]; Φ_F in DMF = 0.28 [107, 108]), and Rhodamine (Φ_F in EtOH = 0.95 [109, 110]) were used as standards. The standard and samples were both excited at the same wavelength and the maximum absorbances of the solutions were kept below 0.05 to avoid any filter effects.

2.3.2 Fluorescence lifetime (τ_F)

Fluorescence lifetime (τ_F) is the time a molecule spends in the excited singlet state (S_1) before returning to the S_0 state *via* fluorescence. A time-correlated single photon counting (TCSPC) technique is used to calculate the fluorescence lifetime of a sample [111]. This is achieved by measuring the time-dependent fluorescence intensity profile of emitted light upon excitation by a pulsed laser [112]. However, as the intensity of the light is very low, the probability of detecting one photon in a single period is consequently also very low. Hence, periods in which more than one photon is observed are very rare. The time elapsed between excitation by the laser pulse and the detection of a fluorescence photon is measured and is referred to as the 'start-stop' time or the time delay (τ). With many repetitions, a distribution of time differences may be acquired, with events being binned based on their respective time differences [113, 114]. Fitting an exponential curve to this distribution can be used to calculate τ_F, the time it takes for the intensity to fall to 1/e of its initial value [112].

Highly dilute solutions are used in order to prevent fluorescence being reabsorbed by neighbouring molecules. However, it is also necessary as this technique relies on the detection of *single* photons [112]. It is necessary, from a detection standpoint, to maintain a low probability of registering more than one photon per cycle. This is because detectors, and the associated electronics, have a "dead" time [114, 115], which lasts a number of nanoseconds following a photon event. During this time, another event cannot be processed. Hence, if the number of photons per cycle was to exceed 1, the system would register the first event but miss any subsequent ones, leading to an over-representation of early photons in the histogram, an effect referred to as "pile-up" [111, 112].

2.3.3 Singlet oxygen quantum yield (Φ_Δ)

As the mechanism for PDT depends upon the formation of singlet oxygen ($^1O_2$) in order to achieve cell death, it is necessary to quantify the amount of singlet oxygen that can be produced by a compound in order to determine its efficacy as a photosensitiser. The singlet oxygen quantum yield (Φ_Δ) is typically described as the number of singlet oxygen molecules generated for every photon absorbed by a photosensitiser (**Eq. 18**). In an ideal situation, the absorption of a single photon has the capacity to generate only one molecule of singlet oxygen. Hence, the Φ_Δ of a photosensitiser, which can be determined using a relative method by comparison with a standard whose Φ_Δ is known [21, 24, 116], is a value between zero and one.

$$\phi_\Delta = \frac{number\ of\ molecules\ of\ singlet\ oxygen\ formed}{number\ of\ photons\ absorbed} \qquad (18)$$

The singlet oxygen quantum yield (Φ_Δ) of BODIPY dyes was studied in a spectrophotometric cell of 1 cm pathlength. Quantum yields of singlet oxygen photogeneration were determined in solution (in air without bubbling oxygen) using the relative method with zinc Pc (ZnPc) or Rose Bengal as a reference, and DPBF (1,3-diphenylisobenzofuran) as a chemical quencher for singlet oxygen [117, 118]. Solutions of the sample and reference sensitisers (absorbance below 0.5 at irradiation wavelength) containing DPBF were prepared in the dark and irradiated at the crossover wavelength – the wavelength at which the absorbances of the sample and standard

solutions are equal – using a laser. The decay of the DPBF absorption peak was monitored spectroscopically with time of irradiation [119]. The values of Φ_Δ were calculated using **Equation 19** [120]:

$$\phi_\Delta = \phi_\Delta{}^{Std} \cdot \frac{I_{abs}}{I_{abs}{}^{Std}} \quad (19)$$

where $\phi_\Delta{}^{Std}$ is the singlet oxygen quantum yield of the standard. I_{abs} and $I_{abs}{}^{Std}$ are the rates of light absorption by the sample and standard, respectively. The initial DPBF concentrations were kept the same for both the reference and the sample. Zinc phthalocyanine (Φ_Δ in DMSO = 0.67 [121]; Φ_Δ in EtOH = 0.53 [27, 121]; Φ_Δ in DMF = 0.56 [27, 107, 122, 123]) and Rose Bengal (Φ_Δ in DMSO = 0.76 [13, 124]; Φ_Δ in EtOH = 0.86 [27, 125]) were used as standards.

2.4 Synthesis and characterisation of BODIPYs

2.4.1 4,4'-Difluoro-8-(4-bromophenyl)-1,3,5,7-tetramethyl-4-bora-3a,4a-diaza-*s*-indacene **(1)**

The synthesis followed a one-pot reaction procedure adapted from literature [44, 46]. Despite the apparent step-wise nature of these reactions, only the final product was isolated and characterised.

4-Bromobenzaldehyde (0.648 g, 3.5 mmol, 1 mole eq.) and 2, 4-dimethylpyrrole (2 mole eq., ρ = 0.924 $g.mol^{-1}$) were added to DCM (50 mL) under Ar/N_2 with stirring. TFA (2-3 drops) was slowly added to the solution. The reaction was carried out at room temperature for 3 h under Ar/N_2 with vigorous stirring in the dark. Thin layer chromatography (TLC) confirmed the absence of the aldehyde and the formation of the appropriate dipyrromethane. The mixture was cooled to 0°C after which a solution of p-chloranil (1.2 mole eq.) in DCM (10 mL) was added dropwise. The solution was allowed to warm up to room temperature and the reaction was left to proceed for 30 min under Ar/N_2 with stirring. A deep purple colour was observed and TLC confirmed the synthesis of the dipyrromethene. The mixture was again cooled to 0°C. TEA (7 mole eq.) and $BF_3{\cdot}Et_2O$ (11 mole eq.) were cooled to 0°C and added dropwise into the dipyrromethene solution. The mixture was left to stir under Ar/N_2 at room temperature for 12 h. The resulting mixture was washed twice with water (2 × 30 mL) and once with brine (30 mL). The organic phase was then dried and separated *via* column chromatography with ethyl acetate and hexane (1:4) as the eluent.

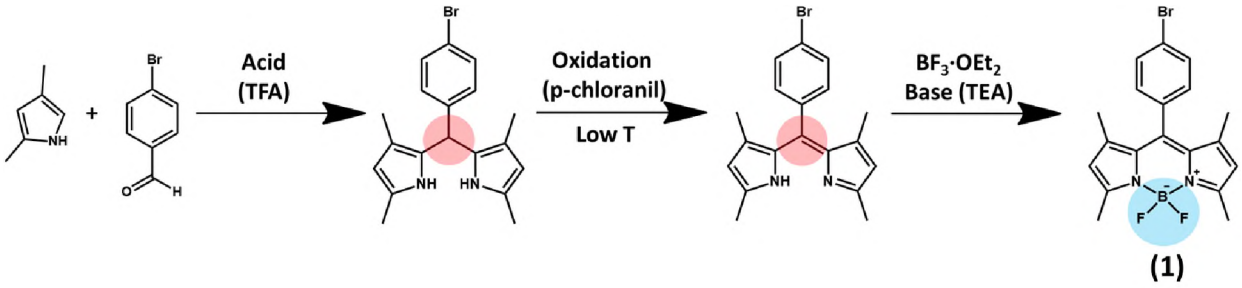

Scheme 4. The acid catalysed synthesis of 4,4'-difluoro-8-(4-bromophenyl)-1,3,5,7-tetramethyl-4-bora-3a,4a-diaza-*s*-indacene **(1)** *via* the classic "one-pot three-step" method, highlighting the structural changes that occur at each step.

(1) Eluent: ethyl acetate/hexane (1:4). Obtained: Orange crystalline powder. Yield: 409 mg (29 %). ^{1}H-NMR (600 MHz, $CDCl_3$) δ 7.67 (d, *J* = 8.4 Hz, 2H), 7.21 (d, *J* = 8.4 Hz, 2H), 6.02 (s, 2H), 2.58 (s, 6H), 1.44 (s, 6H). FT-IR (cm^{-1}): 1500 (C-C in ring stretch), 1300 (C-N stretch), 1183 (C-N stretch), 1061 (C-N stretch), 969 (=C-H bend), 816, 751, 688 (C-Br stretch), 463. Calc. for $C_{19}H_{18}BBrF_2N_2$: Expected: C, 56.62; H, 4.50; N, 6.95. Found: C, 56.98; H, 5.00; N, 6.78.

2.4.2 4,4'-Difluoro-8-(4-bromophenyl)-1,3,5,7-tetramethyl-2,6-dibromo-4-bora-3a,4a-diaza-*s*-indacene **(2)**

(1) (409 mg) and N-bromosuccinimide (NBS) (2.5 mole eq.) were dissolved in DCM (100 mL). The mixture was left to stir under Ar/N_2 at room temperature for 2 h. The reaction was quenched with water and the organic phase was dried and separated *via* column chromatography using silica gel with ethyl acetate/petroleum ether (1:4) as the eluent.

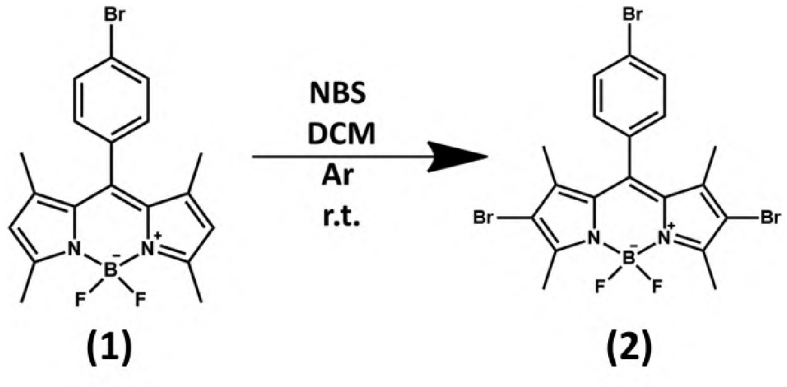

Scheme 5. Synthesis of 4,4'-Difluoro-8-(4-bromophenyl)-1,3,5,7-tetramethyl-2,6-dibromo-4-bora-3a,4a-diaza-*s*-indacene **(2)** *via* nucleophilic addition of bromine to BODIPY **(1)**.

(2) Eluent: ethyl acetate/petroleum ether (1:4). Obtained: deep red crystalline powder. Yield: 465 mg (82.2 %). ^{1}H NMR (600 MHz, $CDCl_3$) δ 7.71 (d, *J* = 8.5 Hz, 2H), 7.18 (d, *J* = 8.4 Hz, 2H), 2.63 (s, 6H), 1.43 (s, 6H). FT-IR (cm^{-1}): 1534 (C-C in ring stretch), 1342 (C-N stretch), 1175 (C-N stretch), 1069 (C-N stretch), 993 (=C-H bend), 746, 683, 585, 522 (C-Br stretch). Calc. for $C_{19}H_{16}BBr_3F_2N_2$: Expected: C, 40.69; H, 2.88; N, 4.99. Found: C, 40.29; H, 3.07; N, 4.75. MALDI-TOF MS: m/z calc. for $C_{19}H_{16}BBr_3F_2N_2$: 559.89; found: 560.52 $[M]^+$.

2.4.3 4,4'-Difluoro-8-(4-bromophenyl)-1,7-dimethyl-2,6-dibromo-3,5-di(thiophen-3-yl)vinyl-4-bora-3a,4a-diaza-*s*-indacene **(3)**

(2) (370 mg, 1 mole eq.), 3-thiophenecarboxaldehyde (3 mole eq.) and glacial acetic acid (0.4 mL) were dissolved in dry benzene (20 mL) under Ar with stirring. Piperidine (0.4 mL) was added slowly and the solution was heated to reflux for 3 h under Ar. A Dean-Stark trap was employed for the azeotropic removal of water formed during the condensation reaction. The reaction was quenched with water and the organic phase was dried and separated using column chromatography with silica gel and ethyl acetate/petroleum ether (1:9) as the eluent.

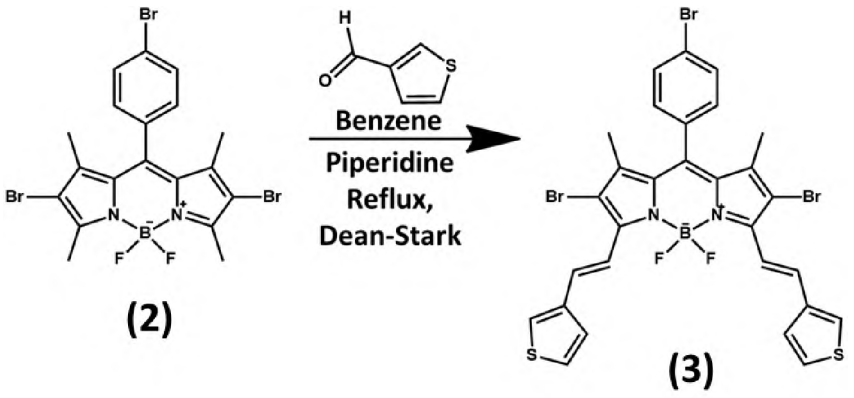

Scheme 6. Synthesis of 4,4'-Difluoro-8-(4-bromophenyl)-1,7-dimethyl-2,6-dibromo-3,5-di(thiophen-3-yl)vinyl-4-bora-3a,4a-diaza-*s*-indacene **(3)** *via* Knoevenagel condensation of 3-thiophenecarboxaldehyde and **(2)**.

(3) Eluent: ethyl acetate/petroleum ether (1:9). Obtained: blue powder. Yield: (55 mg, 11.2 %). 1H NMR (600 MHz, THF-d_8) δ 8.31 (d, J = 16.6 Hz, 2H), 7.92 (d, J = 6.6 Hz, 2H), 7.81 (s, 2H), 7.73 (d, J = 16.7 Hz, 2H), 7.62 (d, J = 2.0 Hz, 4H), 7.51 (d, J = 8.3 Hz, 2H), 1.62 (s, 6H). Calc. for $C_{29}H_{20}BBr_3F_2N_2S_2$: Expected: C, 46.50; H, 2.69; N, 3.74; S, 8.56. Found: C, 45.97; H, 2.88; N, 3.44; S, 7.48. MALDI-TOF MS: m/z calc. for $C_{29}H_{20}BBr_3F_2N_2S_2$: 747.87; found: 749.41 $[M+H]^+$.

2.4.4 4,4'-Difluoro-8-(4-bromophenyl)-1-methyl-2,6-dibromo-3,5,7-tri-styryl-(4'-methylthio)-4-bora-3a,4a-diaza-*s*-indacene **(4)**

(2) (0.178 mmol, 1 mole eq.), 4-(methylthio)benzaldehyde (0.535 mmol, 3 mole eq.) and glacial acetic acid (0.4 mL) were dissolved in dry benzene (20 mL) under Ar with stirring. Piperidine (0.4 mL) was added slowly and the solution was heated to reflux for 2 h under Ar. A Dean-Stark trap was employed for the azeotropic removal of water formed during the condensation reaction. The reaction was quenched with water and the organic phase was dried and separated using column chromatography with silica gel and ethyl acetate/hexane (1:4).

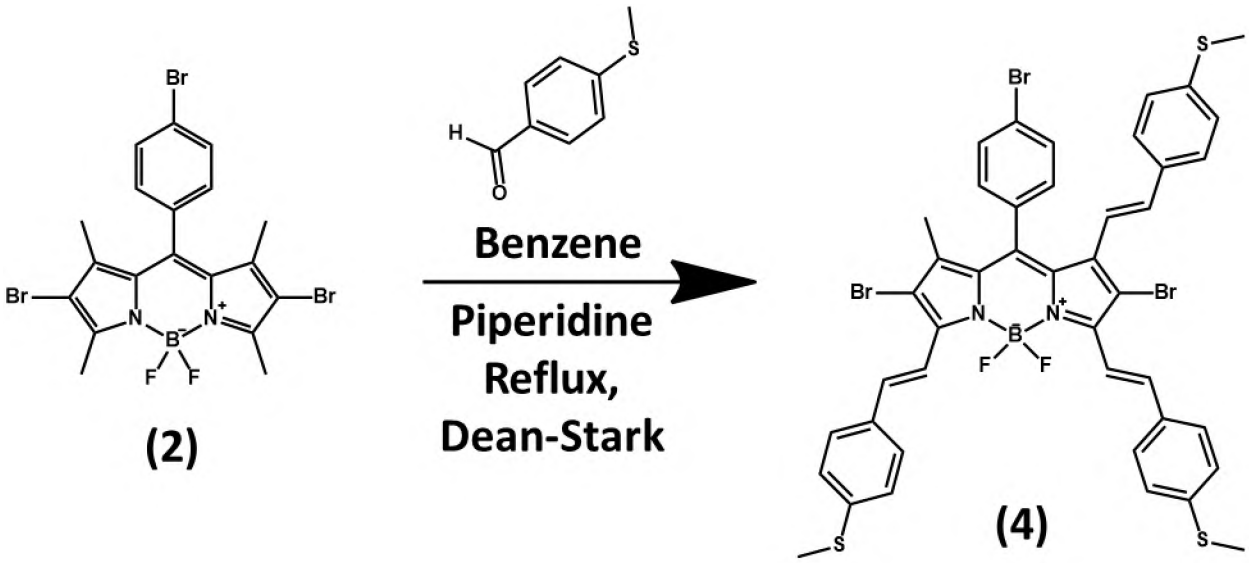

Scheme 7. Knoevenagel condensation of 4-(methylthio)benzaldehyde and **(2)** resulting in the synthesis of tri-(4-methylthio)styryl BODIPY **(4).**

(4) Eluent: Ethyl acetate/hexane (1:4). Obtained: green powder. Yield: 21.6 mg (8.5 %). ^{1}H NMR (600 MHz, $CDCl_3$) δ 8.18 (d, *J* = 16.6 Hz, 1H), 8.06 (d, *J* = 16.6 Hz, 1H), 7.69 (dd, *J* = 16.5 Hz, 2H), 7.55 (dd, *J* = 8.1, 1.8 Hz, 1H), 7.36 (dd, *J* = 8.0, 1.8 Hz, 1H), 7.30 (dd, *J* = 8.4, 3.5 Hz, 5H), 7.21 (dd, *J* = 8.1, 2.0 Hz, 1H), 7.05 (dd, *J* = 8.0, 2.0 Hz, 1H), 6.82 (d, *J* = 8.1 Hz, 2H), 2.56 (s, 9H), 2.50 (s, 3H). MALDI-TOF MS: m/z calc. for $C_{43}H_{34}BBr_3F_2N_2S_3$: 963.95; found: 963.69 $[M]^+$.

2.4.5 4,4'-Difluoro-8-(4-methylthiophenyl)-1,3,5,7-tetramethyl-4-bora-3a,4a-diaza-*s*-indacene **(5)**

Initially, a method described in the literature for the synthesis of aryldipyrromethanes in an aqueous medium by acid-catalysed (HCl) condensation of aromatic aldehydes with pyrrole at room temperature was used to form (4-methylthio)aryldipyrromethane **(5a)** [49]. The aryldipyrromethane is afforded as a precipitate, which may then be filtered and washed, and used in a subsequent one-pot synthesis adapted from literature [44, 46] to afford the corresponding BODIPY dye.

4-(Methylthio)benzaldehyde (1.142 g, 1 mole eq.) and 2,4-dimethylpyrrole (3 mole eq., ρ = 0.924 $g.mol^{-1}$) were added to a stirred 0.18 M HCl solution (50 mL) under Ar. The reaction was carried out at room temperature for 4 h under Ar with vigorous stirring, and the reaction progress was followed by thin layer chromatography (TLC). The precipitated dipyrromethane product **(5a)** was filtered off and washed with water and petroleum ether.

The dipyrromethane product (1.46 g, 6.55 mmol, 1 mole eq.) was then dissolved in DCM (40 mL) and cooled to 0°C before addition of p-chloranil (1.2 mole eq.) in DCM (10 mL). The solution was allowed to warm up to room temperature and the reaction was left to proceed for 20 min under Ar/N_2 with stirring. A deep purple colour was observed and TLC confirmed the synthesis of the dipyrromethene. The mixture was again cooled to 0°C. TEA (7 mole eq.) and $BF_3{\cdot}Et_2O$ (11 mole eq.) were cooled to 0°C and added dropwise into the dipyrromethene solution. The mixture was left to stir under Ar at room temperature for 12 h. The resulting mixture was washed twice with water (2 × 30 mL) and once with brine (30 mL). The organic phase was then dried and separated *via* column chromatography with ethyl acetate and hexane (1:4) as the eluent, yielding BODIPY **(5)**.

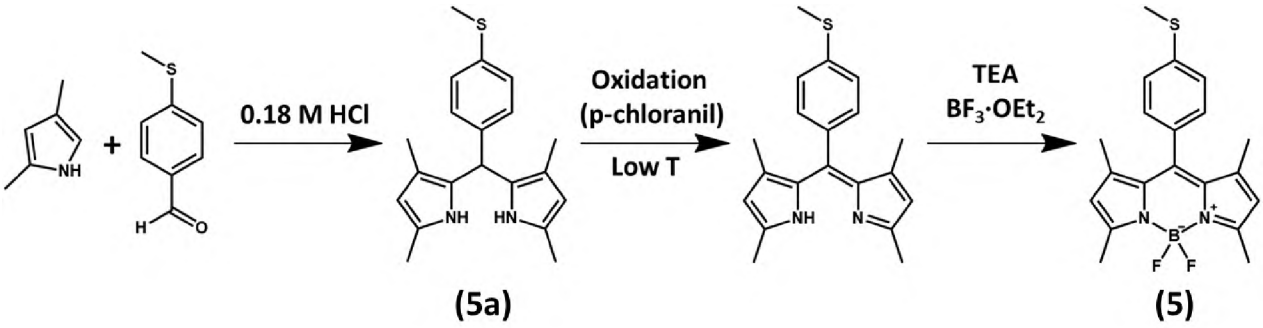

Scheme 8. Synthesis of 4,4'-Difluoro-8-(4-methylthiophenyl)-1,3,5,7-tetramethyl-4-bora-3a,4a-diaza-*s*-indacene **(5)** *via* the water method synthesis of **(5a)** and subsequent one-pot reaction.

(5a) Obtained: dark brown solid. Yield: 2.28 g (93.7 %). ^{1}H NMR (600 MHz, $CDCl_3$) δ 7.21 (d, *J* = 8.4 Hz, 2H), 7.09 (d, *J* = 8.4 Hz, 2H), 5.73 (s, 2H), 5.42 (s, 1H), 2.57 (s, 1H), 2.50 (s, 3H), 2.18 (s, 6H), 1.84 (s, 6H). FT-IR (cm^{-1}): 3419 (pyrrole N-H), 2915, 2858, 1665, 1587, 1489, 1433, 1389, 1389, 1289, 1219, 1088, 1015, 959, 787, 636 (C-S stretch), 505. Calc. for $C_{20}H_{24}N_2S$: Expected: C, 74.03; H, 7.46; N, 8.63; S, 9.88. Found: C, 73.89; H, 7.22; N, 7.63; S, 9.83.

(5) Eluent: ethyl acetate/hexane (1:4) Obtained: Bright orange crystalline powder. Yield: (374 mg, 21 % based on **(5a)**; 13.5 % based on starting aldehyde). ^{1}H NMR (600 MHz, $CDCl_3$) δ 7.37 (d, *J* = 8.4 Hz, 2H), 7.21 (d, *J* = 8.4 Hz, 2H), 6.00 (s, 2H), 2.58 (s, 6H), 2.57 (s, 3H), 1.46 (s, 6H). FT-IR (cm^{-1}): 2918 (C-H stretch), 1500 (C-C in ring stretch), 1297 (C-N stretch), 1059 (C-N stretch), 967 (=C-H bend), 817, 750, 691 (C-S stretch), 466. Calc. for $C_{20}H_{21}BF_2N_2S$: Expected: C, 64.88; H, 5.72; N, 7.57; S, 8.66. Found: C, 65.69; H, 6.46; N, 7.26; S, 8.02.

2.4.6 4,4'-Difluoro-8-(4-methylthiophenyl)-1,3,5,7-tetramethyl-2,6-dibromo-4-bora-3a,4a-diaza-*s*-indacene **(6)**

BODIPY **(6)** was synthesised according to the same method as **(2)**, using **(5)** (100 mg, 1 mole eq.) as the BODIPY core starting material. BODIPY **(6)** was separated *via* column chromatography using silica gel with DCM as the eluent.

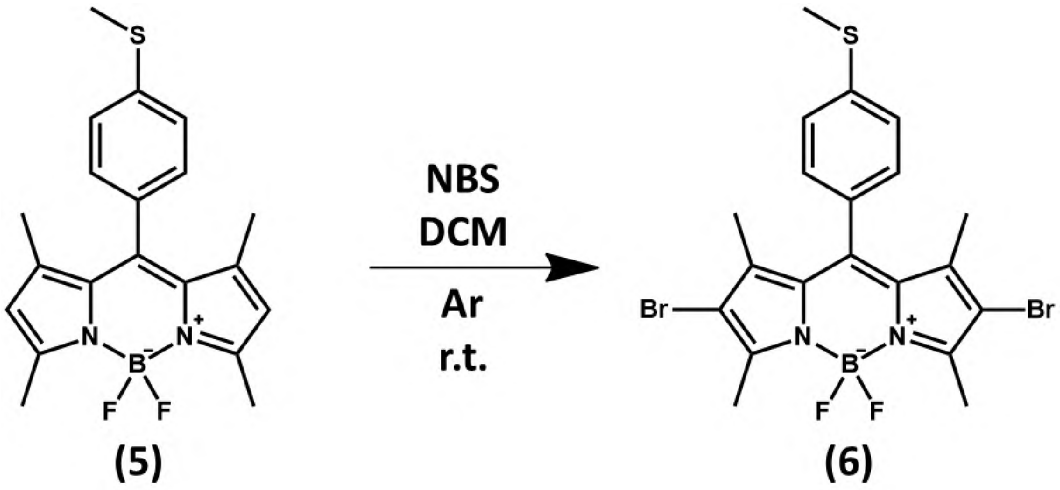

Scheme 9. Synthesis of 4,4'-Difluoro-8-(4-methylthiophenyl)-1,3,5,7-tetramethyl-2,6-dibromo-4-bora-3a,4a-diaza-*s*-indacene **(6)** *via* nucleophilic addition of bromine to BODIPY **(5)**.

(6) Eluent: DCM. Obtained: red powder. Yield: 119 mg (76.8 %). ^{1}H NMR (600 MHz, $CDCl_3$) δ 7.39 (d, *J* = 8.4 Hz, 2H), 7.18 (d, *J* = 8.4 Hz, 2H), 2.62 (s, 6H), 2.58 (s, 3H), 1.45 (s, 6H). FT-IR (cm^{-1}): 2916 (C-H stretch), 2850 (C-H stretch), 1532 (C-C in ring stretch), 1456, 1396, 1345, 1305, 1175 (C-N stretch), 1080 (C-N stretch), 998 (=C-H bend), 821, 744, 691 (C-Br stretch), 587, 523 (C-Br stretch). Calc. for $C_{20}H_{19}BBr_2F_2N_2S$: Expected: C, 45.49; H, 3.63; N, 5.30; S, 6.07. Found: C, 45.47; H, 3.59; N, 5.03; S, 5.52. MALDI-TOF MS: m/z calc. for $C_{20}H_{19}BBr_2F_2N_2S$: 527.97; found: 528.64 $[M]^+$.

2.4.7 4,4'-Difluoro-8-(4-methylthiophenyl)-1-methyl-2,6-dibromo-3,5,7-tri-styryl-4-bora-3a,4a-diaza-*s*-indacene (7)

The synthesis of BODIPYs **(7a)** and **(7b)** was synthesised following the same method as **(4)**, using **(6)** (100 mg, 1 mole eq.) as the starting material. Both the di-**(7a)** and tri-**(7b)** styryl fractions were isolated *via* column chromatography using silica gel, with ethyl acetate/petroleum ether (1:9) as the eluent.

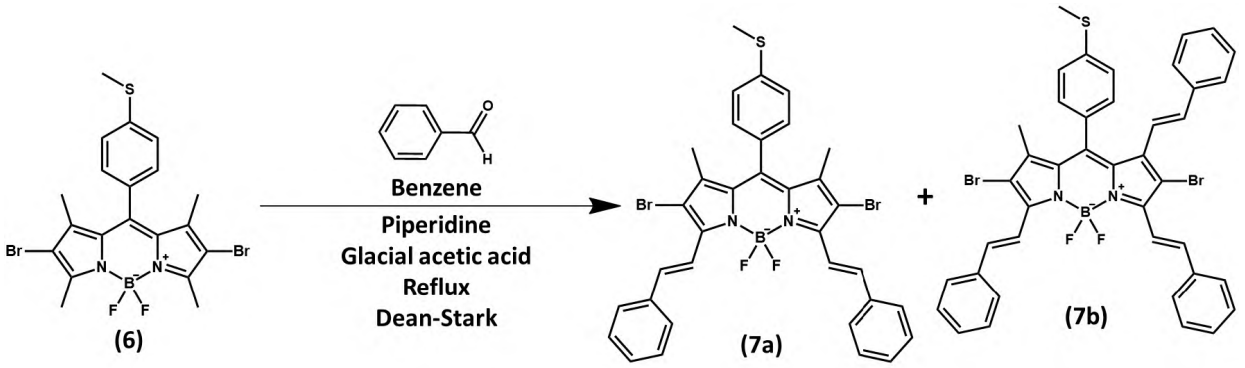

Scheme 10. Knoevenagel condensation of benzaldehyde and **(6)** resulting in the synthesis of di-**(7a)** and tri-**(7b)** styryl BODIPY dyes.

(7a) Eluent: Ethyl acetate/ petroleum ether (1:9). Obtained: blue powder. Yield: 7 mg (5.3 %). ^{1}H NMR (600 MHz, $CDCl_3$) δ 7.78–7.64 (m, 7H), 7.48–7.41 (m, 5H), 7.41–7.35 (m, 3H), 7.27–7.17 (m, 6H), 7.07 (s, 2H), 6.92 (d, *J* = 7.0 Hz, 2H), 2.43 (s, 3H), 1.39 (s, 3H). MALDI-TOF MS: m/z calc. for $C_{34}H_{27}BBr_2F_2N_2S$: 704.03; found: 704.74 $[M]^+$.

(7b) Eluent: ethyl acetate/ petroleum ether (1:9). Obtained: Green-blue powder. Yield: 16 mg (10.7 %). ^{1}H NMR (600 MHz, $CDCl_3$) δ 8.15 (d, *J* = 16.8 Hz, 1H), 8.08 (d, *J* = 16.7 Hz, 1H), 7.74 (dd, *J* = 16.6, 12.2 Hz, 2H), 7.71–7.67 (m, 4H), 7.47–7.42 (m, 5H), 7.38 (dd, *J* = 11.7, 7.2 Hz, 3H), 7.26–7.19 (m, 5H), 7.07 (s, 2H), 6.92 (d, *J* = 7.0 Hz, 2H), 2.43 (s, 3H), 1.39 (s, 3H). MALDI-TOF MS: m/z calc. for $C_{41}H_{31}BBr_2F_2N_2S$: 792.06; found: 792.74 $[M]^+$.

2.4.8 3,5-Dithienylenevinylene BODIPYs **(8)**, **(9)**, and **(10)**

4,4'-Difluoro-8-phenyl-1,7-dimethyl-3,5-di(thiophen-2-yl)vinyl-4-bora-3a,4a-diaza-*s*-indacene **(8)**; 4,4'-difluoro-8-(4-carbomethoxyphenyl)-1,7-dimethyl-3,5-di(thiophen-2-yl)vinyl-4-bora-3a,4a-diaza-*s*-indacene **(9)**; and 4,4'-difluoro-8-phenyl-1,7-dimethyl-2,6-diiodo-3,5-di(thiophen-2-yl)vinyl-4-bora-3a,4a-diaza-*s*-indacene **(10)** (**Fig. 14**) were synthesised and purified by Dr. Lizhi Gai [126].

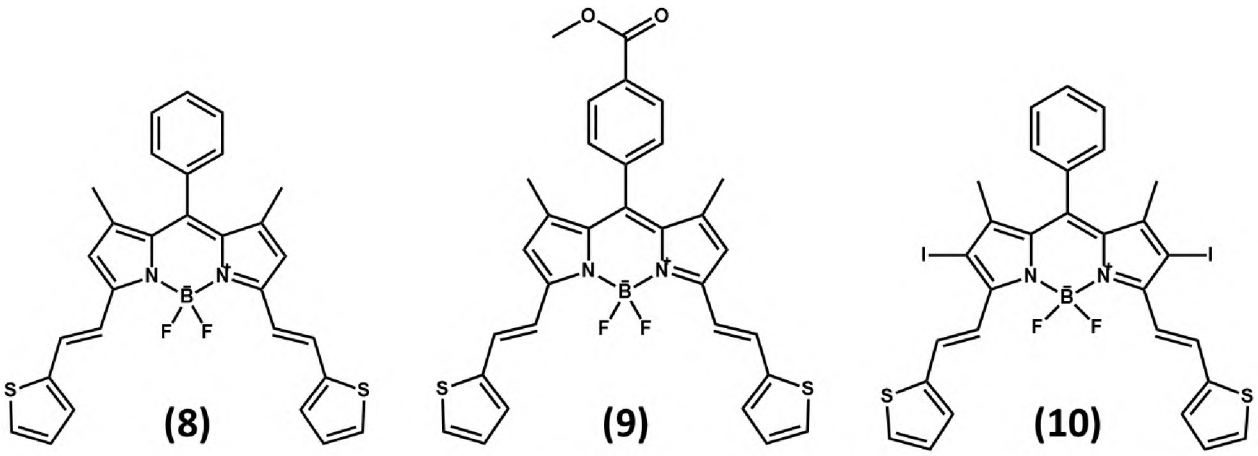

Figure 14. Structures of BODIPYs **(8)**, **(9)**, and **(10)**.

(8) ^{1}H NMR (600 MHz, Acetone) δ 7.73 (d, *J* = 16.1 Hz, 2H), 7.67–7.58 (m, 5H), 7.51 (dd, *J* = 21.4, 11.5 Hz, 4H), 7.35 (d, *J* = 3.4 Hz, 2H), 7.20–7.14 (m, 2H), 6.89 (s, 2H), 1.48 (s, 6H). MALDI-TOF MS: m/z calc. for $C_{29}H_{23}BF_2N_2S_2$: 512.14; found: 511.96 $[M]^+$.

(9) ^{1}H NMR (600 MHz, Acetone) δ 8.26 (d, *J* = 8.0 Hz, 2H), 7.76 (s, 1H), 7.74 (s, 1H), 7.69 (d, *J* = 8.1 Hz, 2H), 7.61 (d, *J* = 5.0 Hz, 2H), 7.53 (d, *J* = 16.2 Hz, 2H), 7.36 (d, *J* = 3.4 Hz, 2H), 7.18–7.15 (m, 2H), 6.91 (s, 2H), 3.98 (s, 3H), 1.48 (s, 6H). MALDI-TOF MS: m/z calc. for $C_{31}H_{25}BF_2N_2O_2S_2$: 570.14; found: 570.10 $[M]^+$.

(10) ^{1}H NMR (600 MHz, THF) δ 8.44 (d, *J* = 16.4 Hz, 2H), 7.62 (dd, *J* = 8.2, 6.7 Hz, 4H), 7.59–7.55 (m, 3H), 7.47–7.44 (m, 2H), 7.37 (d, *J* = 3.5 Hz, 2H), 7.13 (dd, *J* = 5.0, 3.7 Hz, 2H), 1.51 (s, 6H). MALDI-TOF MS: m/z calc. for $C_{29}H_{21}BF_2I_2N_2S_2$: 763.93; found: 764.45 $[M]^+$.

2.5 Preparation of thin films

Poly(bisphenol A carbonate) (PBC) (110 mg) and 0.1 mg of 3,5-dithienylenevinylene BODIPYs **(3)**, **(8)**, **(9)**, and **(10)** were respectively dissolved in DCM (1.5 mL) and sonicated until a homogeneous mixture of BODIPY–polymer solution was obtained. The BODIPY–PBC solutions were dropped on glass substrates placed in a Petri dish and the solvent was allowed to evaporate at room temperature. The average film thickness was determined to be ca. 17, 21, 21 and 17 µm for BODIPY **(3)–**, **(8)–**, **(9)–**, and **(10)–PBC** respectively, using SEM.

Chapter 3:

Synthesis and Spectroscopic Characterisation of BODIPY Dyes

Introduction

This chapter explores the synthesis of two BODIPY dyes; their 2,6-dibrominated analogues; and their 3,5- or 3,5,7-substituted, red-shifted analogues.

BODIPY **(1)** has a *para*-bromo substituent on the *meso*-phenyl group of the BODIPY core and has been reported [45]. Its 2,6-dibrominated analogue, BODIPY **(2)**, has also been reported [127, 128]. However, its 3,5-di(thiophen-3-yl)vinyl **(3)** and 3, 5, 7-tri (4-methylthio)styryl **(4)** derivatives have not been reported to date.

To the best of our knowledge, neither BODIPY **(5)**, which has a *para*-methylthio substituent on the *meso*-phenyl group of the BODIPY core, nor its corresponding aryldipyrromethane **(5a)** has been reported to date. Its 2,6-dibrominated analogue, BODIPY **(6)**; and 3,5-distyryl **(7a)** and 3,5,7-tristyryl **(7b)** derivatives have also not been reported.

BODIPY **(1)** was synthesised according to the classic "one-pot three-step" acid catalysed condensation reaction, while BODIPY **(5)** was prepared *via* the synthesis of the relevant aryldipyrromethane in an aqueous medium by acid-catalysed (HCl) condensation of aromatic aldehydes. In the case of the latter, the aryldipyrromethane precipitate was filtered and washed, and used in subsequent one-pot synthesis adapted from literature, as per BODIPY **(1)**.

The BODIPY cores, **(1)** and **(5)**, were prepared for use in further reactions, to produce BODIPY dyes with increasingly complex structures. Bromination of these two BODIPYs at the 2,6-positions yielded BODIPYs **(2)** and **(6)**, respectively. Thereafter, the acidic methyl groups at the 3,5,7-positions of BODIPYs **(2)** and **(6)** were exploited for the attachment of groups intended to extend the π-conjugation of the BODIPY dyes, resulting in BODIPYs **(3)**, **(4)**, **(7a)** and **(7b)**, whose main spectral bands are red-shifted. The photophysical properties of the 2,6-dibrominated BODIPY dyes, and their red-shifted analogues, were investigated with a special focus on their singlet oxygen-generating capability.

3.1 4,4'-Difluoro-8-(4-bromophenyl)-1,3,5,7-tetramethyl-4-bora-3a,4a-diaza-*s*-indacene **(1)**

3.1.1 Synthesis of BODIPY **(1)**

Although previously reported, BODIPY **(1)** was synthesised as a precursor for a more complex BODIPY dye intended for use in PDT. Additionally, it was used for comparison purposes. BODIPY **(1)** was synthesised *via* the "one-pot three-step" trifluoroacetic acid-catalysed condensation of 2,4-dimethylpyrrole and 4-bromobenzaldehyde in DCM (**Scheme 11**). The methyl groups on the pyrrole served to sterically block the 2,4-position carbons, reducing unwanted polymerisation of the pyrrole unit and hence improving the overall yield of the reaction.

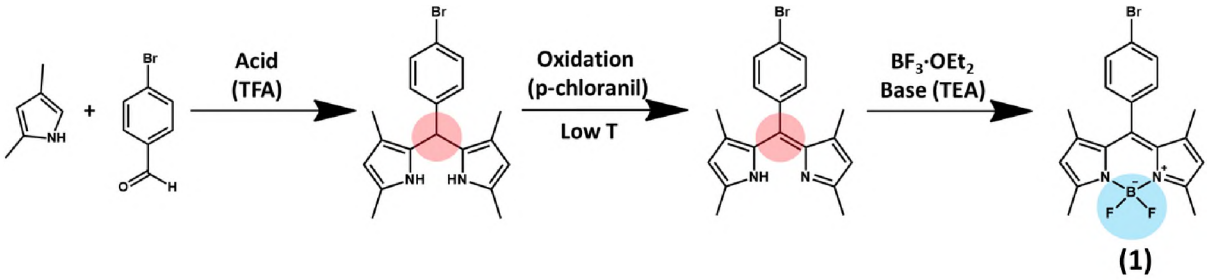

Scheme 11. The acid catalysed synthesis of 4,4'-difluoro-8-(4-bromophenyl)-1,3,5,7-tetramethyl-4-bora-3a,4a-diaza-*s*-indacene **(1)** *via* the classic "one-pot" method, highlighting the structural changes that occur at each step.

3.1.2 Structural analysis of BODIPY **(1)**

All eighteen protons can be readily identified in the ^{1}H NMR spectrum of BODIPY **(1)** (**Fig. 15**). The two doublets between 7.21–7.67 ppm each integrate as two protons and can hence be attributed to the four phenyl protons. The singlet at 6.02 ppm, integrating to two protons, was attributed to the protons at the 2,6-positions of the BODIPY core. The singlets at 2.58 and 1.44 ppm each integrate to 6 protons. The singlet at 2.58 ppm may be attributed to the methyl groups positioned adjacent to the *meso*-phenyl, while the singlet occurring upfield at 1.44 ppm is attributed to the methyl groups at the 3,5-positions, which experience shielding due to their proximity to the

pyrrolic nitrogens, which carry a partial positive charge due to the delocalised resonance structure (**Fig. 15**). The solvent residual peak of $CDCl_3$ occurs at 7.26 ppm while H_2O peak is visible at 1.56 ppm [129].

CHNS elemental analysis for this compound was in good agreement with expected values. FT-IR analysis of BODIPY **(1)** showed peaks that are in good agreement with the vibrations of the BODIPY skeleton that have been reported in the literature [61]. A number of C–N stretch bands, attributed to the pyrrolic nitrogen atoms, lie in the 1060–1300 cm^{-1} region, while a C–Br stretch is visible at 688 cm^{-1} (**Fig. 16**).

Small orange crystals of BODIPY **(1)** were obtained. Even under ambient light, some yellow-green solid state fluorescence may be observed (**Fig. 17**).

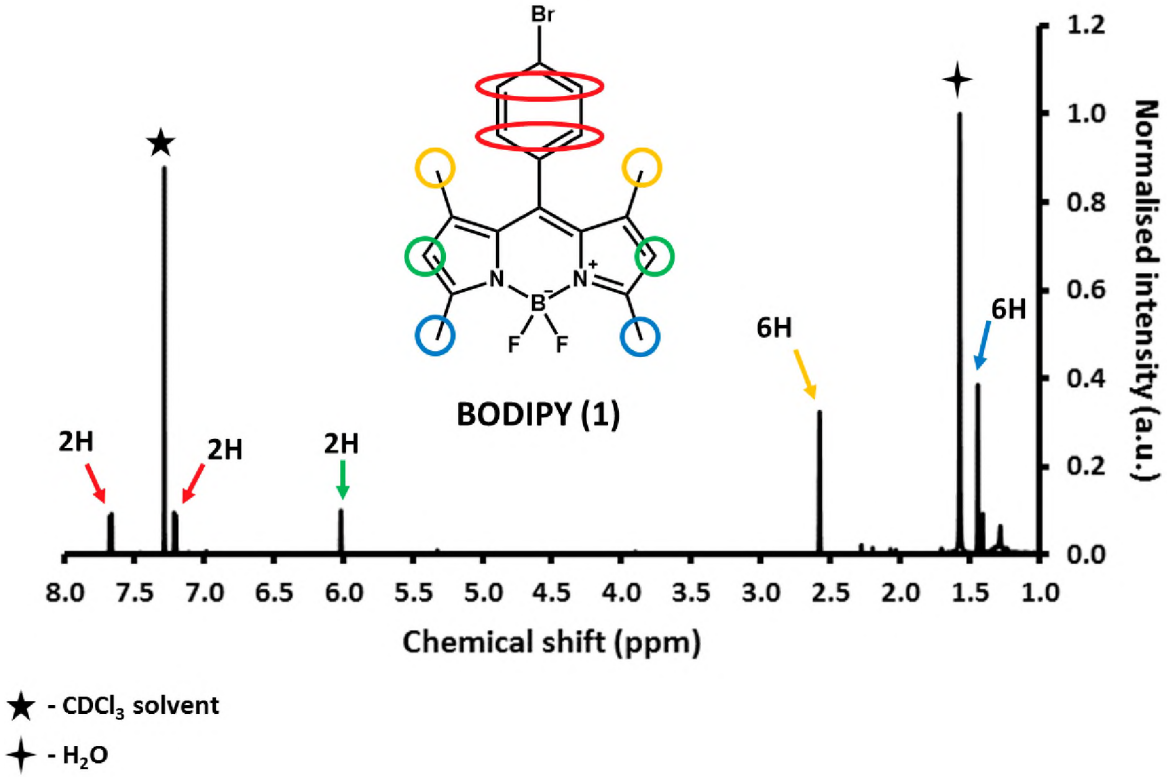

Figure 15. ^1H NMR spectrum of BODIPY **(1)** in $CDCl_3$. The stars indicate the solvent and water peaks, respectively.

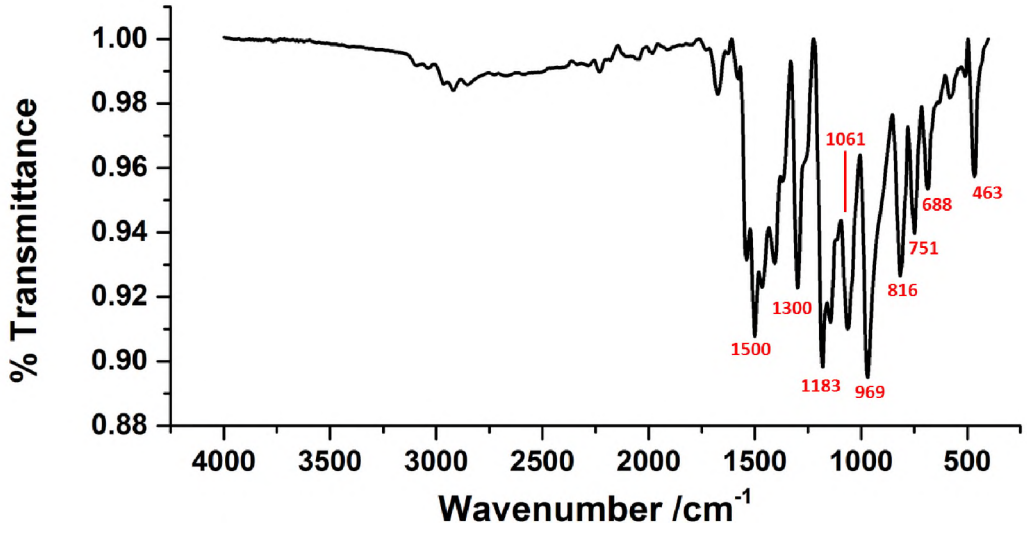

Figure 16. The FT-IR spectrum of BODIPY **(1)**, highlighting the BODIPY vibrational skeleton.

Figure 17. Orange crystals of BODIPY **(1)** under ambient light.

3.1.3 Spectroscopic properties of BODIPY **(1)**

The electronic absorption spectrum for BODIPY **(1)** is typical of that of a *meso*-substituted BODIPY, with an absorbance maximum at 503 nm in DMSO (**Fig. 18**) that similar to that which has been previously reported [127]. The emission spectrum is typical for a tetra-methyl BODIPY (**Fig. 18**) [2]. **Table 3** summarises the absorption, excitation and emission band wavelength maxima for BODIPY **(1)** in a number of different solvents. BODIPY **(1)** is highly soluble in a range of solvents, and did not show signs of aggregation. BODIPY **(1)** is highly fluorescent due to its lack of ISC and its rigid π-system, which limits the rate of nonradiative decay [2]. The low rate of ISC also results in very low singlet oxygen quantum yields (**Table 3**). Singlet oxygen quantum yields (Φ_Δ) were determined using the comparative method, using DPBF as a chemical trap for singlet oxygen. The rate at which DPBF is decreased in the presence of BODIPY **(1)** was compared to that of a standard – Rose Bengal – in order to determine its Φ_Δ. BODIPY **(1)** shows no measurable decrease in the main absorption band upon irradiation, indicating good photostability.

The log ε value of 4.83 obtained for BODIPY **(1)** in DMF corresponds closely with the reported values of 4.84 (in DCM) and 4.90 (in THF) [45]. The fluorescence quantum yield (Φ_F) of 0.82 in DMSO was comparable to the literature value of 0.84, recorded in DCM [45].

Table 3. Photophysical data for BODIPY **(1)** in a number of different solvents.

Solvent	Solvent polarity	log ε	λ_{abs} /nm	λ_{exc} /nm	λ_{em} /nm	Δ Stokes /nm	Φ_F ± 0.01	τ_F /ns	Φ_Δ
DMSO	7.2	–	503	503	517	14	0.82	3.46	0.06
DMF	6.4	4.83	503	503	514	11	–	–	–
Ethanol	5.2	–	501	501	511	10	–	–	–
THF [a]	4.0	4.90	502	–	511	9	0.53	–	–
DCM [a]	3.1	4.84	503	–	513	10	0.84	–	–

[a] Values reported in the literature [45]

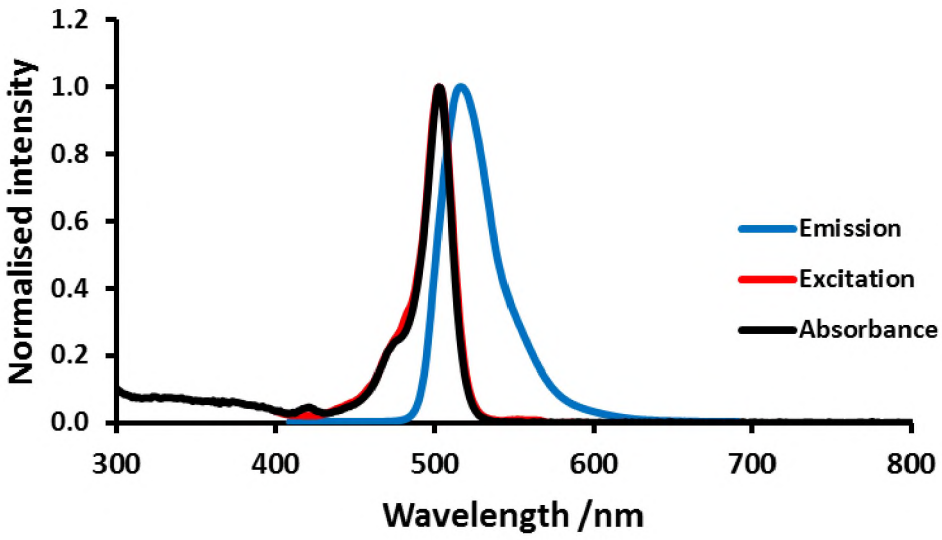

Figure 18. Normalised absorption (*black*), excitation (*red*) and emission (*blue*) spectra of BODIPY **(1)** in DMSO.

3.2 4,4'-Difluoro-8-(4-bromophenyl)-1,3,5,7-tetramethyl-2,6-dibromo-4-bora-3a,4a-diaza-*s*-indacene **(2)**

3.2.1 Synthesis of BODIPY **(2)**

Halogenation of the BODIPY core is a simple method whereby the spectroscopic properties of the molecule may be tuned. However, the primary motivation for bromination, in this work, is to promote ISC, thereby increasing the ability of the BODIPY to produce singlet oxygen. The 2,6-positions of a tetramethyl BODIPY have been shown to be the most vulnerable to nucleophilic attack [58]. Hence, BODIPY **(2)**, a compound that has been reported in the literature [127, 128], was synthesised *via* bromination of **(1)** using N-bromosuccinimide (NBS).

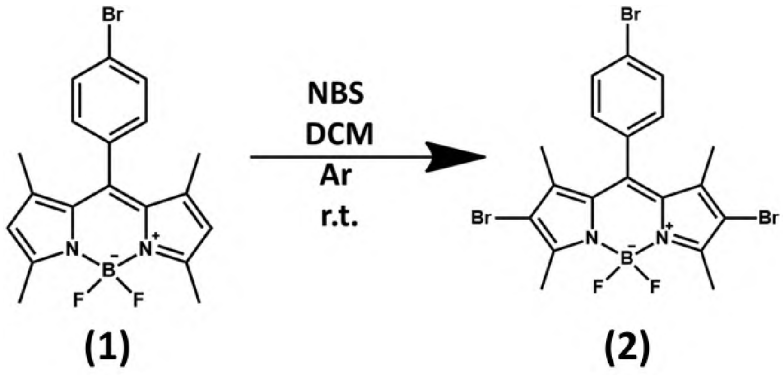

Scheme 12. Synthesis of 4,4'-Difluoro-8-(4-bromophenyl)-1,3,5,7-tetramethyl-2,6-dibromo-4-bora-3a,4a-diaza-*s*-indacene **(2)** *via* nucleophilic addition of bromine to BODIPY **(1)**.

3.2.2 Structural analysis of BODIPY **(2)**

All sixteen protons can be readily identified in the ^{1}H NMR spectrum of BODIPY **(2)**. The two doublets between 7.18–7.71 ppm each integrate as two protons and can hence be attributed to the four phenyl protons. The singlets at 2.63 and 1.43 ppm each integrate to 6 protons. The singlet at 2.63 ppm may be attributed to the methyl groups positioned adjacent to the *meso*-phenyl, while the singlet occurring upfield at 1.43 ppm is attributed to the methyl groups at the 3,5-positions, which experience shielding due to their proximity to the pyrrolic nitrogens. The

absence of the singlet at 6.02 ppm confirms that the hydrogen atoms present at the 2,6-positions of BODIPY **(1)** have been replaced with bromine atoms.

CHNS elemental analysis for this compound was in good agreement with expected values.

The FT-IR spectrum for BODIPY **(2)** shows broadly similar vibrations to that of BODIPY **(1)**, confirming that the BODIPY core remains intact upon bromination.

The predicted molecular mass of 560.86 for BODIPY **(2)** was confirmed by MALDI-TOF mass spectrometry as the primary peak occurred at 560.52.

3.2.3 Spectroscopic properties of BODIPY (2)

The electronic absorption spectrum for BODIPY **(2)** is typical of a BODIPY dye, with the absorbance maximum occurring at 530 nm in DMSO (**Fig. 19**): a red-shift of ca. 30 nm with respect to its parent dye, BODIPY **(1)**. Attachment of bromine atoms at the 2,6-positions causes a destabilisation of the HOMO with respect to the LUMO, resulting in a reduced HOMO–LUMO gap, and hence a red shift of the main spectral bands. **Table 4** summarises the absorption, excitation and emission band wavelength maxima for BODIPY **(2)** in a number of different solvents. BODIPY **(2)** is highly soluble in a range of solvents, and did not show signs of aggregation. A small blue shift of the main spectral bands was observed when moving from DMSO (polarity index = 7.2) to the less polar ethanol (polarity index = 5.2). The presence of bromine atoms at the 2,6-positions of BODIPY **(2)** increases the rate of ISC by relaxation of the spin-selection rule due to the heavy atom effect. This, in turn, increases the ability of the BODIPY dye to produce singlet oxygen. Hence, BODIPY **(2)** shows a significantly higher Φ_{Δ} value than BODIPY **(1)** (**Table 4**).

Table 4. Photophysical data for BODIPY **(2)**.

Solvent	log ε	λ_{abs} /nm	λ_{exc} /nm	λ_{em} /nm	Δ Stokes /nm	Φ_F ± 0.01	τ_F /ns[a]	Φ_Δ
DMSO	–	530	529	547	18	0.14	1.26 (0.98) 7.06 (0.02)	–
DMF	4.99	529	528	545	17	–	–	–
Ethanol	–	528	528	543	15	–	–	0.76
DCM [b]	4.76	528	–	551	23	0.08	–	–

[a] Abundances in brackets, [b] Values reported in the literature [128]

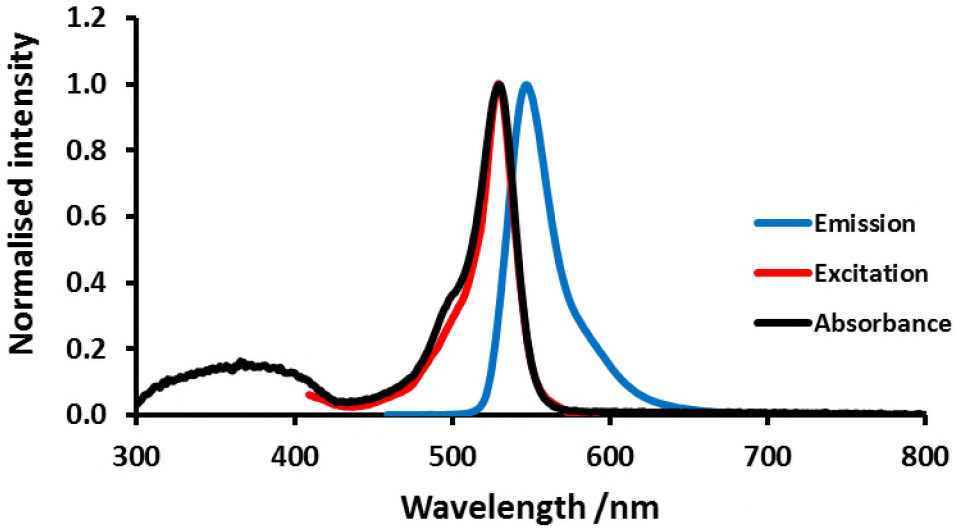

Figure 19. Normalised absorption (*black*), excitation (*red*) and emission (*blue*) spectra of BODIPY **(2)** in DMSO.

3.3 4,4'-Difluoro-8-(4-bromophenyl)-1,7-dimethyl-2,6-dibromo-3,5-di(thiophen-3-yl)vinyl-4-bora-3a,4a-diaza-*s*-indacene **(3)**

3.3.1 Synthesis of BODIPY **(3)**

BODIPY **(3)** was synthesised using a modified Knoevenagel condensation reaction [7, 61, 64]. Substitution at the acidic methyl groups served a twofold purpose in the context of this work. Firstly, the main absorption bands of the BODIPY can be red-shifted due to the extension of the delocalisation pathway. Secondly, substitution at these positions served as a means for providing functionality. In this case, the incorporation of the thiophene groups introduced sulfur atoms, which could potentially be used for conjugation to gold nanoparticles for drug delivery.

BODIPY **(3)** was obtained by column chromatography using ethyl acetate/ petroleum ether (1:9) as eluent (**Fig. 20**). The product was afforded as a blue powder.

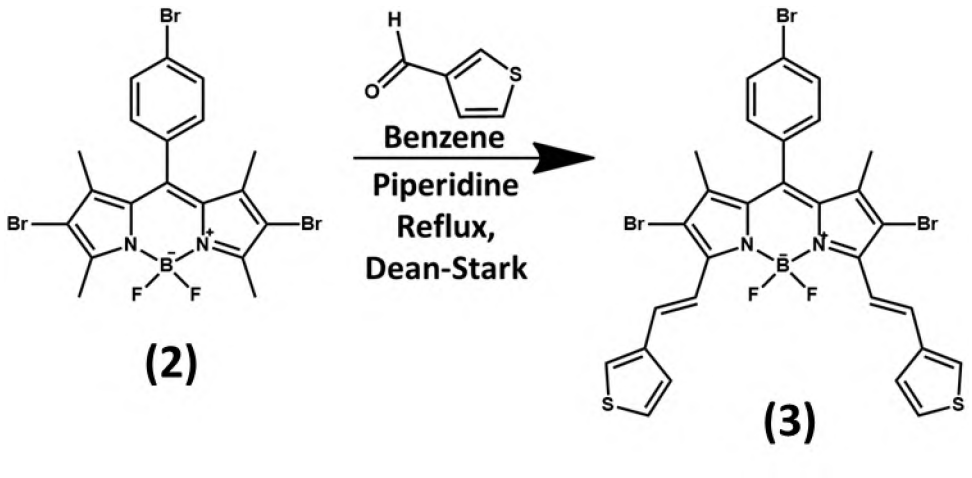

Scheme 13. Knoevenagel condensation of 3-thiophenecarboxaldehyde and **(2)** resulting in the synthesis of BODIPY **(3)**.

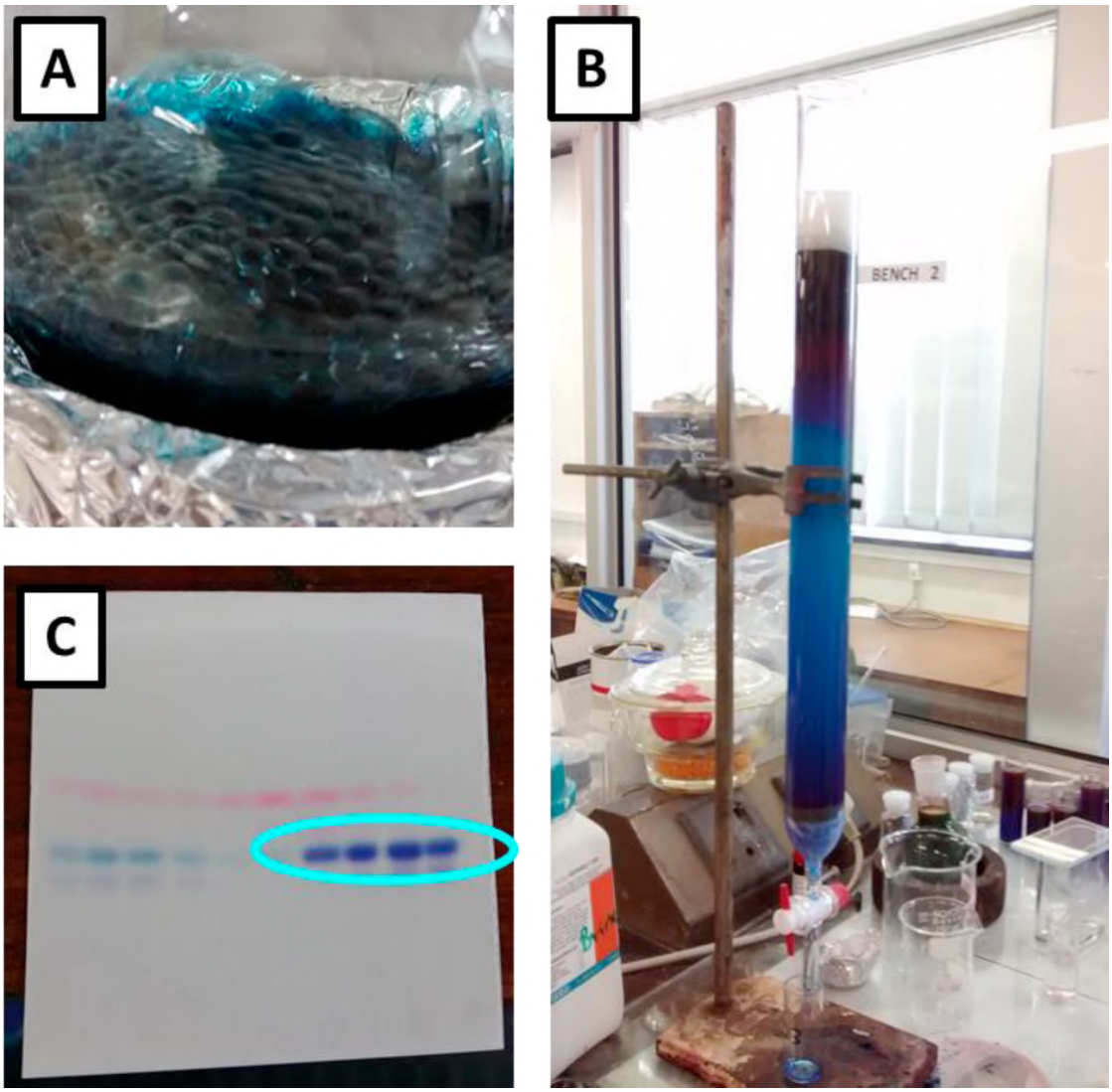

Figure 20. The reaction mixture of BODIPY **(3)** was blue in colour (A), and was purified by column chromatography using silica gel, with ethyl acetate/ petroleum ether (1:9) as eluent (B). TLC was used to identify fractions containing BODIPY **(3)** (C).

3.3.2 Structural analysis of BODIPY **(3)**

All twenty protons can be identified in the ^{1}H NMR spectrum of BODIPY **(3)** (**Fig. 21**). In the aromatic region, in the range of 8.5–7.5 ppm, there are a number of peaks that integrate to 14 protons – the expected number of protons for this region. The singlet at 1.62 ppm integrates to 6 protons and is attributed to the two methyl groups present at the 1, 7-positions of the BODIPY

core. The solvent residual peaks of THF occur at 1.72 and 3.58 ppm, while the H_2O peak is typically seen at 2.46 ppm [130].

The predicted molecular mass of 749.13 for BODIPY **(3)** was confirmed by MALDI-TOF mass spectrometry. Although the primary peak occurred at 752.92 $[M+4H]^+$ **(Fig. 22**), there was a peak at 749.41, corresponding $[M+H]^+$. As the structure of BODIPY **(3)** has multiple points at which fragmentation can occur, it is not unexpected that the mass spectrum shows several different peaks. CHNS elemental analysis for this compound was in good agreement with expected values.

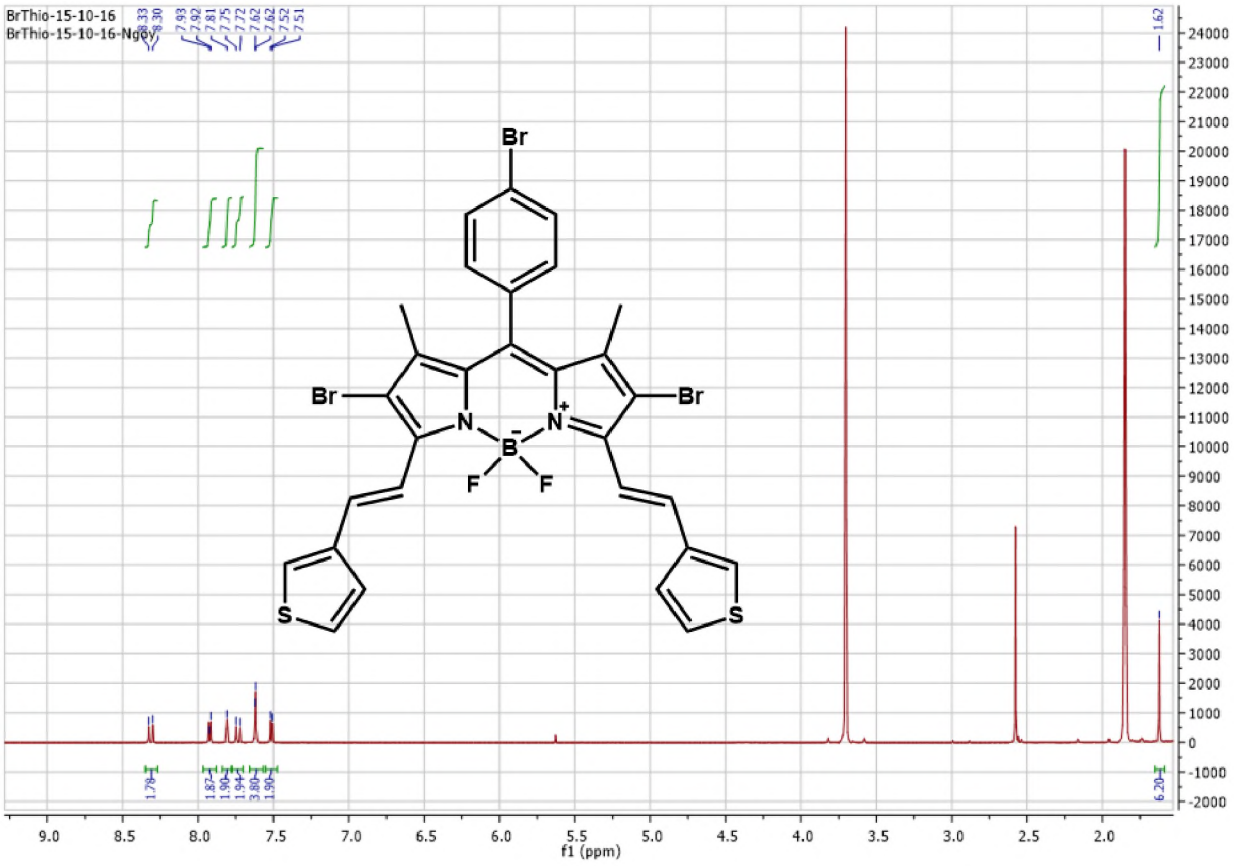

Figure 21. ^{1}H NMR spectrum of BODIPY **(3)** in THF.

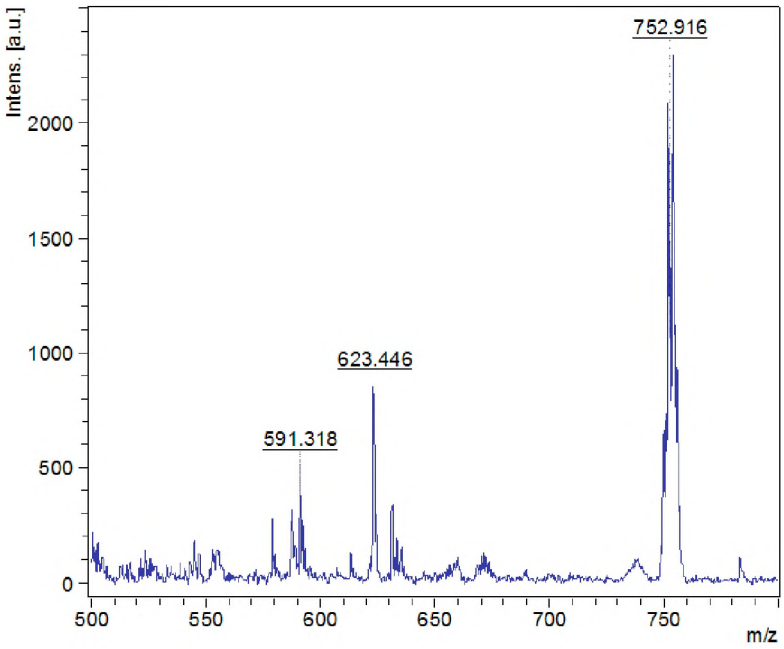

Figure 22. Mass spectrum of BODIPY **(3)**. The primary peak was observed at 752.92 $[M+4H]^+$.

3.3.3 Spectroscopic properties of BODIPY **(3)**

BODIPY **(3)** is a blue dye (**Fig. 23**) with an electronic absorption spectrum that is typical of a BODIPY dye, with the absorbance maximum occurring at 650 nm in DMF (**Fig. 24**). The absorption maximum of BODIPY **(3)** is red-shifted by ca. 147 nm when compared to its parent dye, BODIPY **(1)**, and by 121 nm with respect to BODIPY **(2)**. As the main spectral bands of BODIPY **(3)** are red-shifted to the edge of the therapeutic window, it has potential for use in PDT.

Table 5 summarises the absorption, excitation and emission band wavelength maxima for BODIPY **(3)** in DMSO, DMF and ethanol. The position of the spectral maxima of BODIPY **(3)** were not particularly affected by the change in solvent, with variations of only 3 nm occurring.

The singlet oxygen quantum yield of BODIPY **(3)** was determined by monitoring the photocatalytic degradation of DPBF using ZnPc as standard. Although the presence of bromine atoms at the 2,6-positions of BODIPY **(3)** increases the rate of ISC by relaxation of the spin-selection rule, the singlet oxygen quantum yield of BODIPY **(3)** (**Table 5**) is not as high as that of BODIPY **(2)** due to the increased molecular flexibility, which provides pathways for nonradiative decay.

Table 5. Photophysical data for BODIPY **(3)**.

Solvent	**log ε**	**λ_{abs} /nm**	**λ_{exc} /nm**	**λ_{em} /nm**	**Δ Stokes /nm**	**Φ_F ± 0.01**	**τ_F /ns**	**Φ_Δ**
DMSO	–	652	652	673	21	–	–	–
DMF	4.92	650	650	670	20	0.44	4.00	0.28
Ethanol	–	650	650	670	20	–	–	–

Figure 23. BODIPY **(3)** under ambient light.

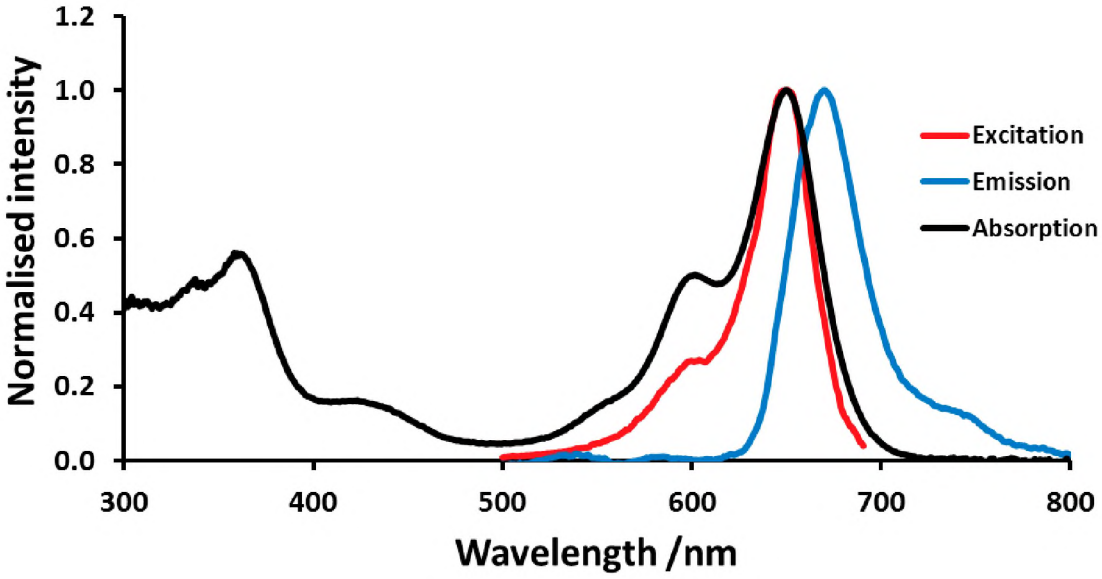

Figure 24. Normalised absorption (*black*), excitation (*red*) and emission (*blue*) spectra of BODIPY **(3)** in DMF.

3.4 4,4'-Difluoro-8-(4-bromophenyl)-1-methyl-2,6-dibromo-3,5,7-tri-styryl-(4'-methylthio)-4-bora-3a,4a-diaza-s-indacene **(4)**

3.4.1 Synthesis of BODIPY **(4)**

BODIPY **(4)** was synthesised using a modified Knoevenagel condensation reaction [7, 61, 64], in a similar manner to that described for BODIPY **(3)**.

BODIPY **(4)** was obtained by column chromatography using ethyl acetate/ petroleum ether (1:9) as eluent (**Fig. 25**). The product was afforded as a green powder.

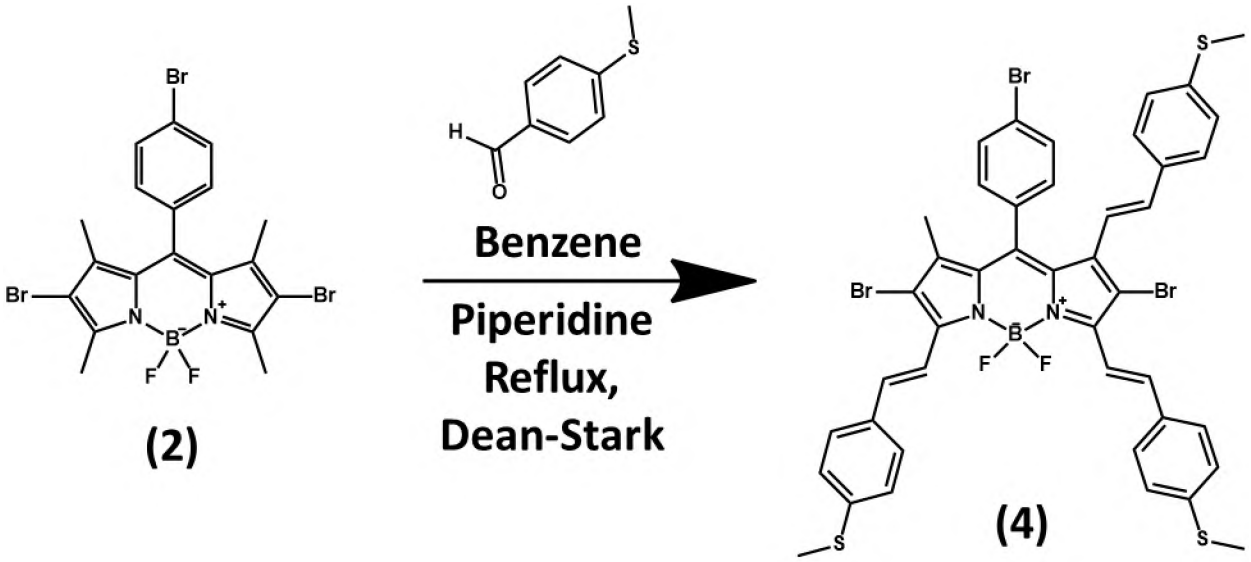

Scheme 14. Knoevenagel condensation of 4-(methylthio)benzaldehyde and **(2)** resulting in the synthesis of tri-(4-methylthio)styryl BODIPY **(4)**.

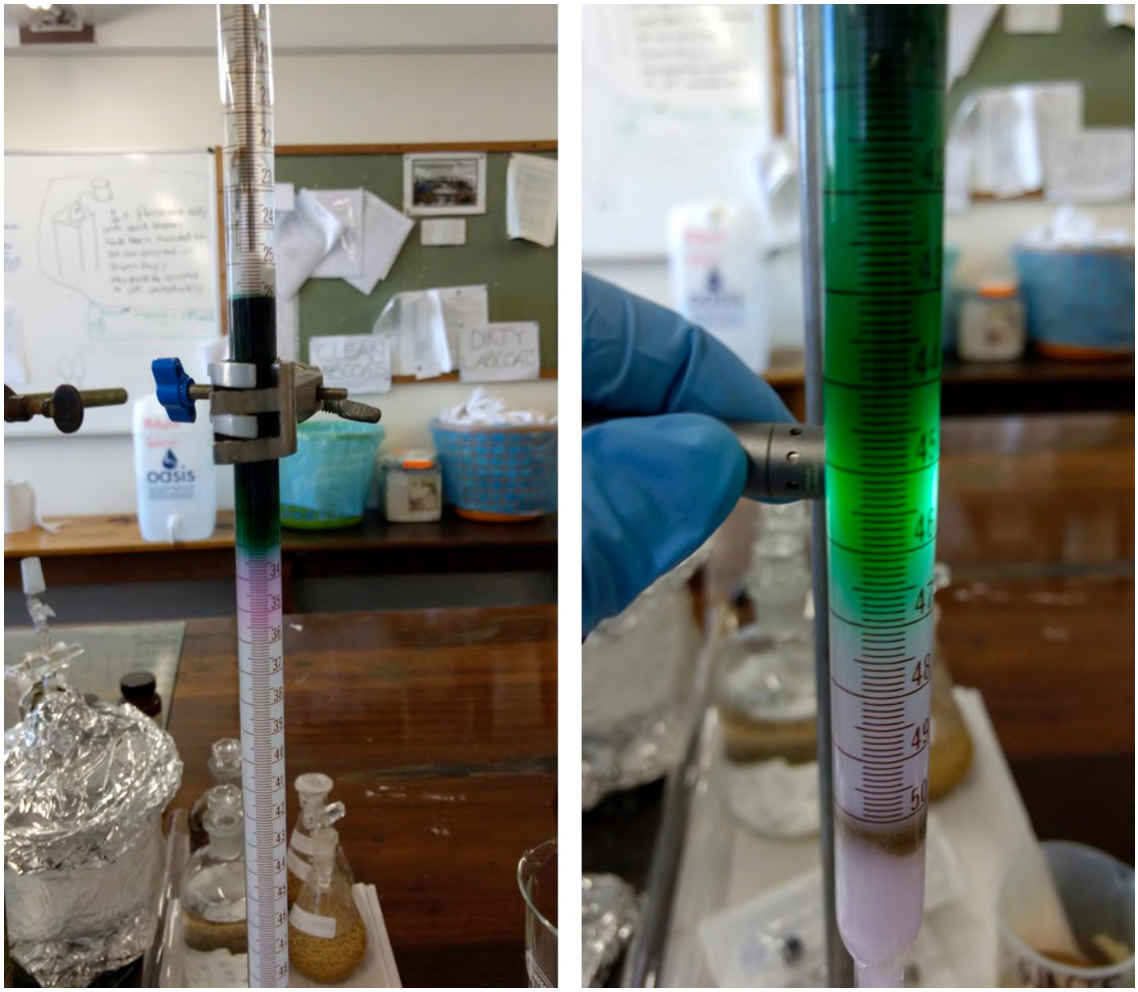

Figure 25. BODIPY **(4)** was purified by column chromatography using silica gel, with ethyl acetate/ petroleum ether (1:9) as eluent.

3.4.2 Structural analysis of BODIPY **(4)**

All thirty-four protons can be identified in the ^{1}H NMR spectrum of BODIPY **(4)** (**Fig. 26 A**). In the aromatic region, in the range of 8.2–6.5 ppm, there are a number of doublets and doublets of doublets that all integrate to give 22 protons – the expected number of protons for this region. In circumstances where a proton may be coupled to two protons by different coupling constants, a doublet of doublets is observed (**Fig. 26 B**). This is particularly common in aromatic compounds, where both the *ortho*- and *meta*- couplings are large enough to see. The remaining protons are accounted for by singlets at 1.35 and 2.56 ppm. The singlet at 2.56 ppm integrates to 9 protons and is attributed to the three S-methyl groups, while the singlet further upfield at 1.35 ppm, integrating to 3 protons, is assigned to the 1-methyl group. The intense TMS peak is visible at 0.09, the solvent residual peak of $CDCl_3$ occurs at 7.28 ppm, and the H_2O peak is visible at 1.61 ppm.

The predicted molecular mass of 963.46 for BODIPY **(4)** was confirmed by MALDI-TOF mass spectrometry, as the primary peak occurred at 963.69. The structure of BODIPY **(4)** has multiple points at which fragmentation can occur and hence it is not unexpected that the mass spectrum should show a fairly large number of peaks. Additional peaks correspond to [**(4)**-Br] and [**(4)**+Br], for example.

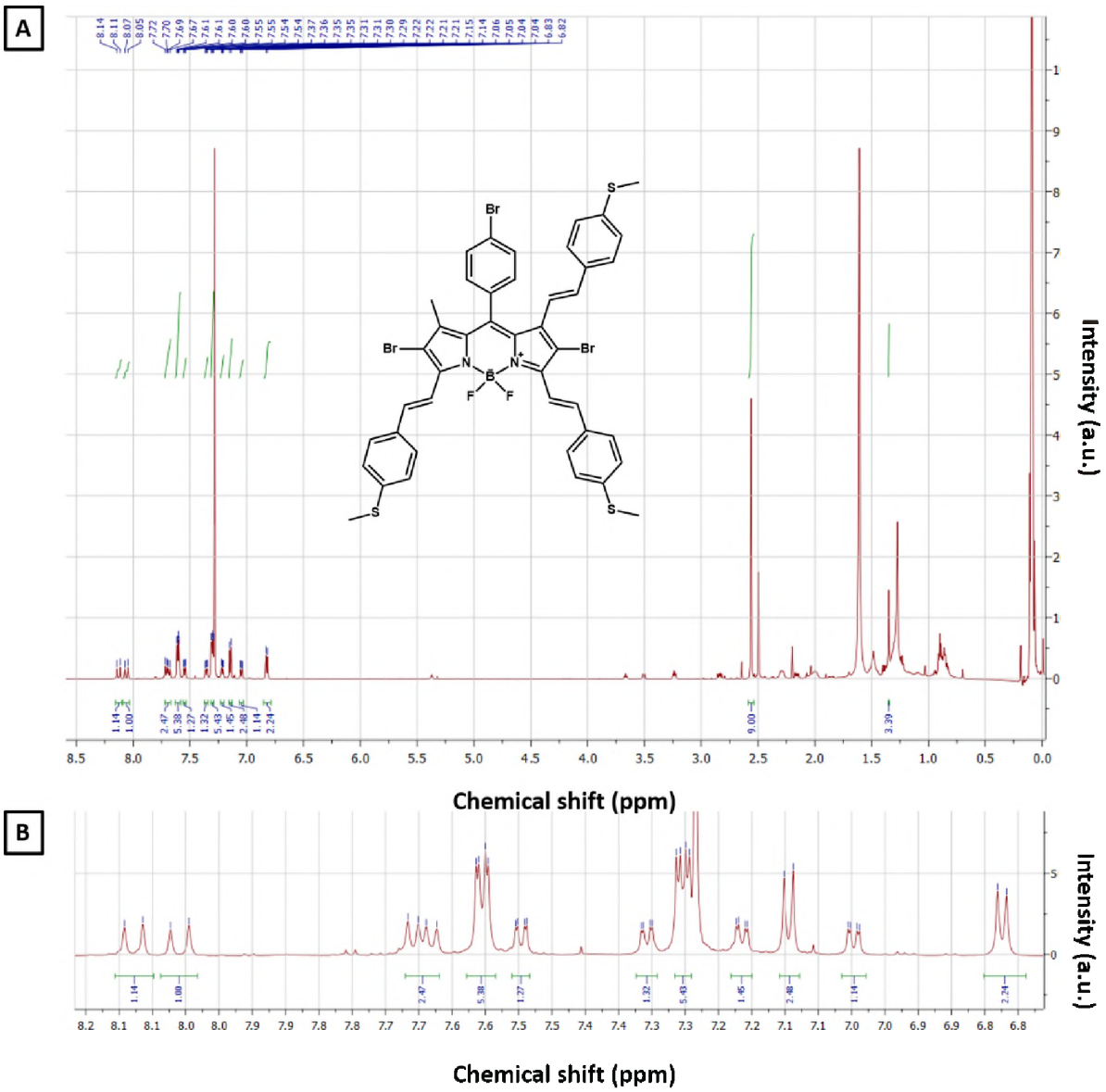

Figure 26. (A) ^{1}H NMR spectrum of BODIPY **(4)** in $CDCl_3$ with (B) expansion of the aromatic region.

3.4.3 Spectroscopic properties of BODIPY **(4)**

The electronic absorption spectrum for BODIPY **(4)** is typical of a BODIPY dye, with the absorbance maximum occurring at 681 nm in DMSO (**Fig. 27**). The absorption maximum of BODIPY **(4)** is red-shifted by ca. 175 nm when compared to its parent dye, BODIPY **(1)**, and by 151 nm with respect to BODIPY **(2)**. As the main spectral bands of BODIPY **(4)** are red-shifted to within the therapeutic window, it has potential for use in PDT.

Table 6 summarises the absorption, excitation and emission band wavelength maxima for BODIPY **(4)** in DMSO, DMF and ethanol. It also shows the log ε value for BODIPY **(4)** in DMF, which was calculated from the increase in absorbance with concentration, using the Beer-Lambert law (**Fig. 28**). The spectral maxima of BODIPY **(4)** varied by up to 14 nm, depending on the solvent used.

The singlet oxygen quantum yield of BODIPY **(4)** was determined by monitoring the photocatalytic degradation of DPBF (**Fig. 29**), using ZnPc as standard. Although the presence of bromine atoms at the 2,6-positions of BODIPY **(4)** increases the rate of ISC by relaxation of the spin-selection rule, the singlet oxygen quantum yield of BODIPY **(4)** (**Table 6**) is not as high as that of BODIPY **(2)** due to the increased molecular flexibility, which allows for more nonradiative decay. BODIPY **(4)** showed good photostability, with its absorption band remaining reasonably constant throughout the experiment (**Fig. 29**).

Table 6. Photophysical data for BODIPY **(4)**.

Solvent	log ε	λ_{abs} /nm	λ_{exc} /nm	λ_{em} /nm	Δ Stokes /nm	Φ_F ± 0.01	τ_F /ns[a]	Φ_Δ
DMSO	–	681	682	723	41	0.06	3.02 (0.89) 0.47 (0.11)	–
DMF	3.99	678	678	716	38	–	–	–
Ethanol	–	673	671	709	38	–	–	0.30

[a] Abundances in brackets

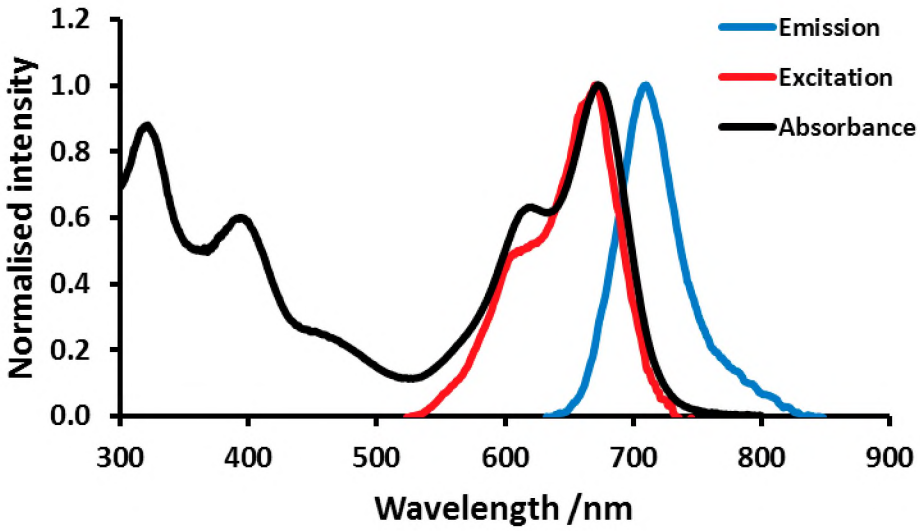

Figure 27. Normalised absorption (*black*), excitation (*red*) and emission (*blue*) spectra of BODIPY **(4)** in ethanol.

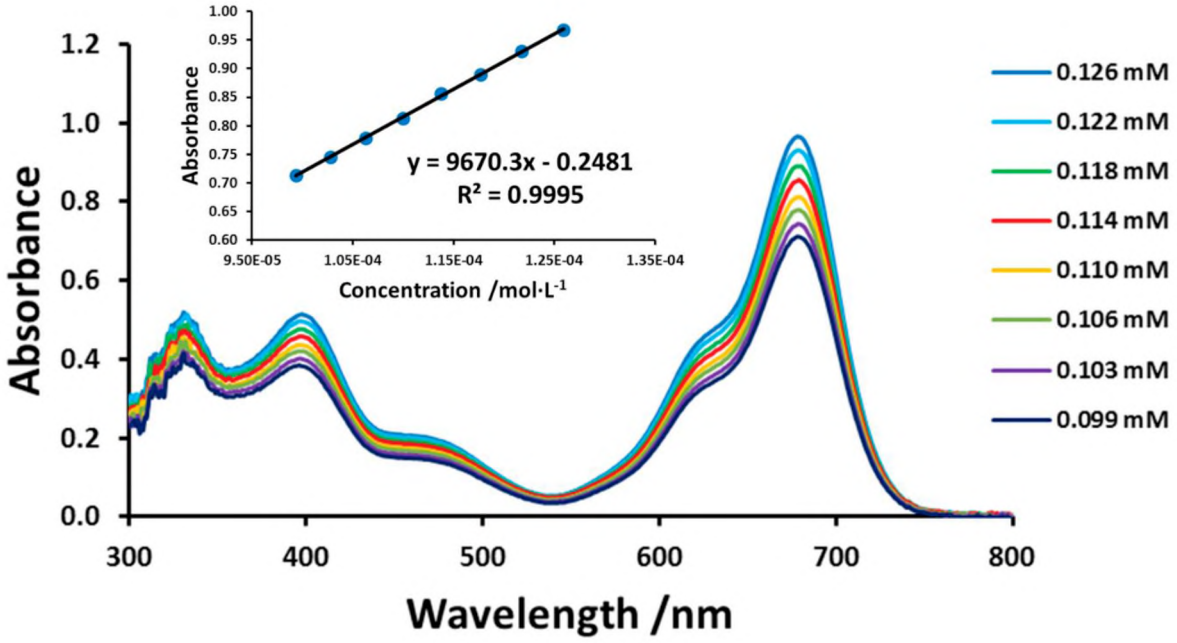

Figure 28. UV-visible absorption spectral changes with concentration for BODIPY **(4)** from 0.100–0.126 mM in DMF. The inset shows the increase of the BODIPY main spectral band intensity with concentration, and is used to calculate log ε for **(4)**.

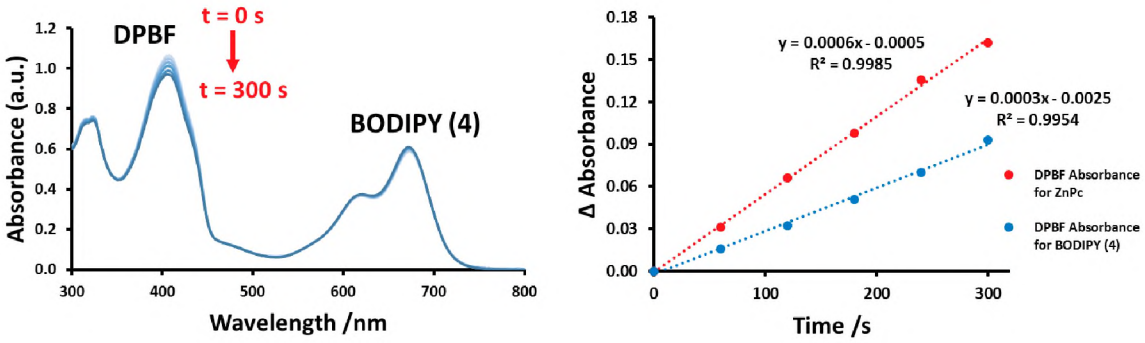

Figure 29. Photocatalytic degradation of DPBF (λ_{max} = 410 nm) in EtOH by BODIPY **(4)** (λ_{max} = 673 nm) at 60 s intervals, indicative of singlet oxygen generation (*left*). The Φ_{Δ} value for **(4)** is determined using the comparative method with ZnPc in EtOH (Φ_{Δ} = 0.53 [27, 121]) as standard (*right*).

3.5 4,4'-Difluoro-8-(4-methylthiophenyl)-1,3,5,7-tetramethyl-4-bora-3a,4a-diaza-*s*-indacene **(5)**

3.5.1 Synthesis of BODIPY **(5)**

The aryldipyrromethane precursor to BODIPY **(5)**, (4-methylthio)aryldipyrromethane **(5a)**, was synthesised in very high yield using a method described by Rohand et. al. [49]. This acid-catalysed condensation reaction of aromatic aldehyde and dimethylpyrrole utilises HCl in an aqueous medium, and the product may be obtained by simple filtration due to selective precipitation of the aryldipyrromethane. In a subsequent one-pot reaction, the aryldipyrromethane was oxidised, forming the corresponding dipyrromethene, which was then complexed with $BF_3{\cdot}Et_2O$ in a basic environment (as per BODIPY **(1)**), to yield BODIPY **(5)**.

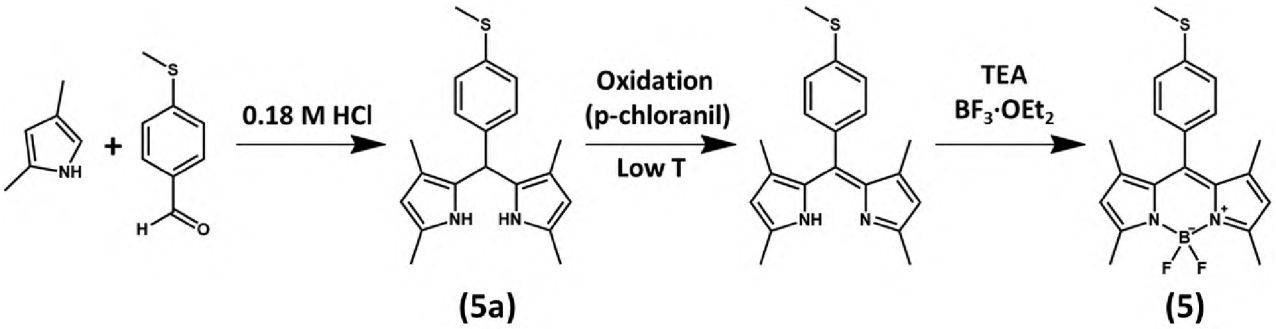

Scheme 15. Synthesis of 4,4'-Difluoro-8-(4-methylthiophenyl)-1,3,5,7-tetramethyl-4-bora-3a,4a-diaza-*s*-indacene **(5)** *via* the water method synthesis of the corresponding aryldipyrromethane **(5a)** and subsequent one-pot reaction.

3.5.2 Structural analysis of (4-methylthio)aryldipyrromethane **(5a)**

Twenty-two of the twenty-four protons can be readily identified in the ^1H NMR spectrum of **(5a)** in $CDCl_3$ (**Fig. 30**). The missing protons are those belonging to the NH groups. The position of NMR signals of the protons of NH groups is strongly dependent upon concentration, temperature and the solvent employed [131]. If two or more NH groups are present on a molecule, the NMR spectrum will show a single signal at an average chemical shift due to rapid proton exchange

[132]. Additionally, NH groups show broad resonance signals that are sometimes hidden in the noise [131, 133, 134], which appears to be the case in **Fig. 30**. The two doublets between 7.09–7.21 ppm each integrate as two protons and can hence be attributed to the four phenyl protons. The singlet at 5.73 ppm, integrating to two protons, was attributed to the protons positioned at what would become the 2,6-positions on the BODIPY core. The singlet at 5.42 pm integrates to one proton and was attributed to the proton at the *meso*-position. The singlet at 2.50 ppm, integrating to 3 protons, is attributed to the methyl group attached to sulphur at the *para*-position of the *meso*-phenyl. The singlets at 2.18 and 1.84 ppm each integrate to 6 protons. The singlet at 2.18 ppm may be attributed to the methyl groups positioned adjacent to the *meso*-phenyl, while the singlet occurring upfield at 1.84 ppm is attributed to the methyl groups at the 3,5-positions. The solvent residual peak of $CDCl_3$ occurs at 7.29 ppm while H_2O peak is visible at 1.57 ppm [129]. Rotation around the single bonds allows for lower-energy conformers. Consequently, the chemical shifts may differ slightly from those observed for their rigid BODIPY counterparts.

CHNS elemental analysis for this compound was in good agreement with expected values.

FT-IR confirms the presence of pyrrolic nitrogen, with an N-H stretch observed at 3419 cm^{-1}, while a C–S stretch is visible at 636 cm^{-1}.

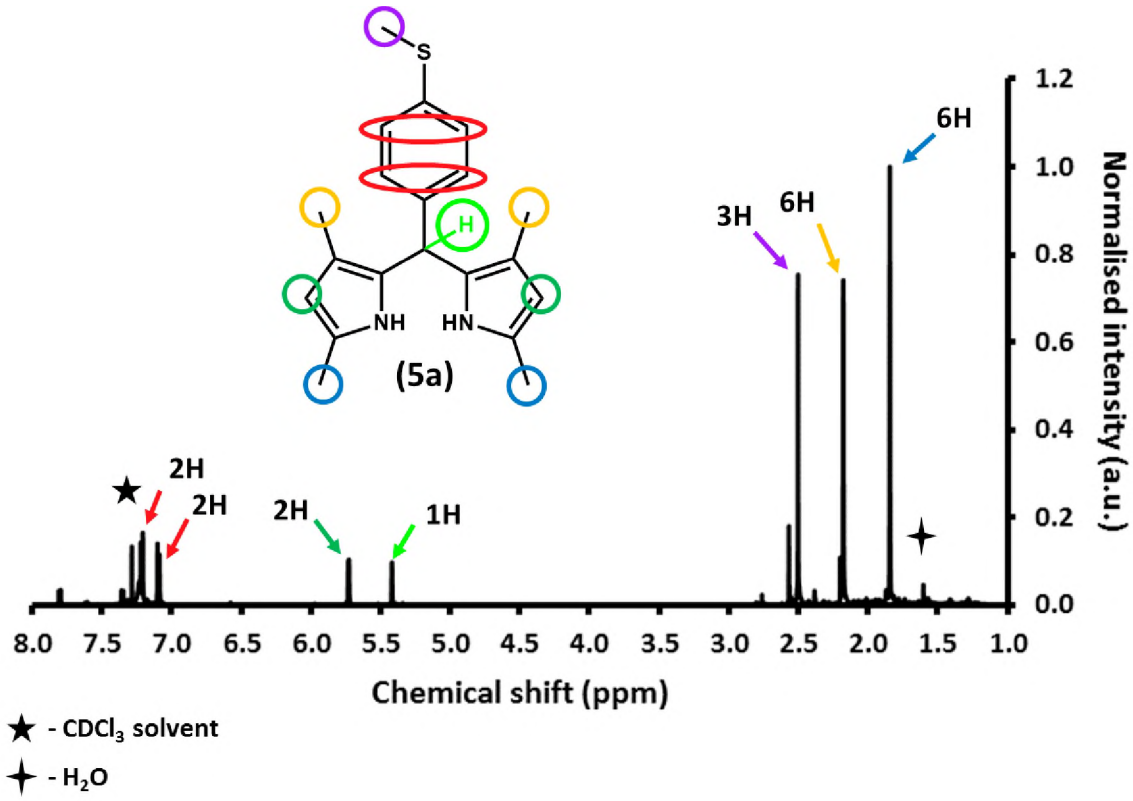

Figure 30. ^{1}H NMR spectrum of (4-methylthio)aryldipyrromethane **(5a)** in $CDCl_3$. The stars indicate the solvent and water peaks, respectively.

3.5.3 Structural analysis of BODIPY **(5)**

All twenty-one protons could be readily identified in the ^{1}H NMR spectrum of BODIPY **(5)** (**Fig. 31**). The two doublets between 7.21–7.37 ppm each integrate as two protons and can hence be attributed to the four phenyl protons. The singlet at 6.00 ppm, integrating to two protons, was attributed to the protons at the 2,6-positions of the BODIPY core. The singlets at 2.58 and 1.46 ppm each integrate to 6 protons. The singlet at 2.58 ppm may be attributed to the methyl groups positioned adjacent to the *meso*-phenyl, while the singlet occurring upfield at 1.46 ppm is attributed to the methyl groups at the 3,5-positions, which experience shielding due to their proximity to the pyrrolic nitrogens. The singlet at 2.57 ppm, integrating to 3 protons (see inset, **Fig. 31**), is attributed to the methyl group attached to sulphur at the *para*-position of the *meso*-

phenyl. The solvent residual peak of $CDCl_3$ occurs at 7.26 ppm while H_2O peak is visible at 1.56 ppm [129].

CHNS elemental analysis for this compound was in good agreement with expected values. FT-IR analysis of BODIPY **(5)** showed peaks that are in good agreement with the vibrations of the BODIPY skeleton that have been reported in the literature [61]. Two C–N stretch bands, attributed to the pyrrolic nitrogen atoms, lie in the 1059–1297 cm^{-1} region, while a C–S stretch is visible at 691 cm^{-1} (**Fig. 32**).

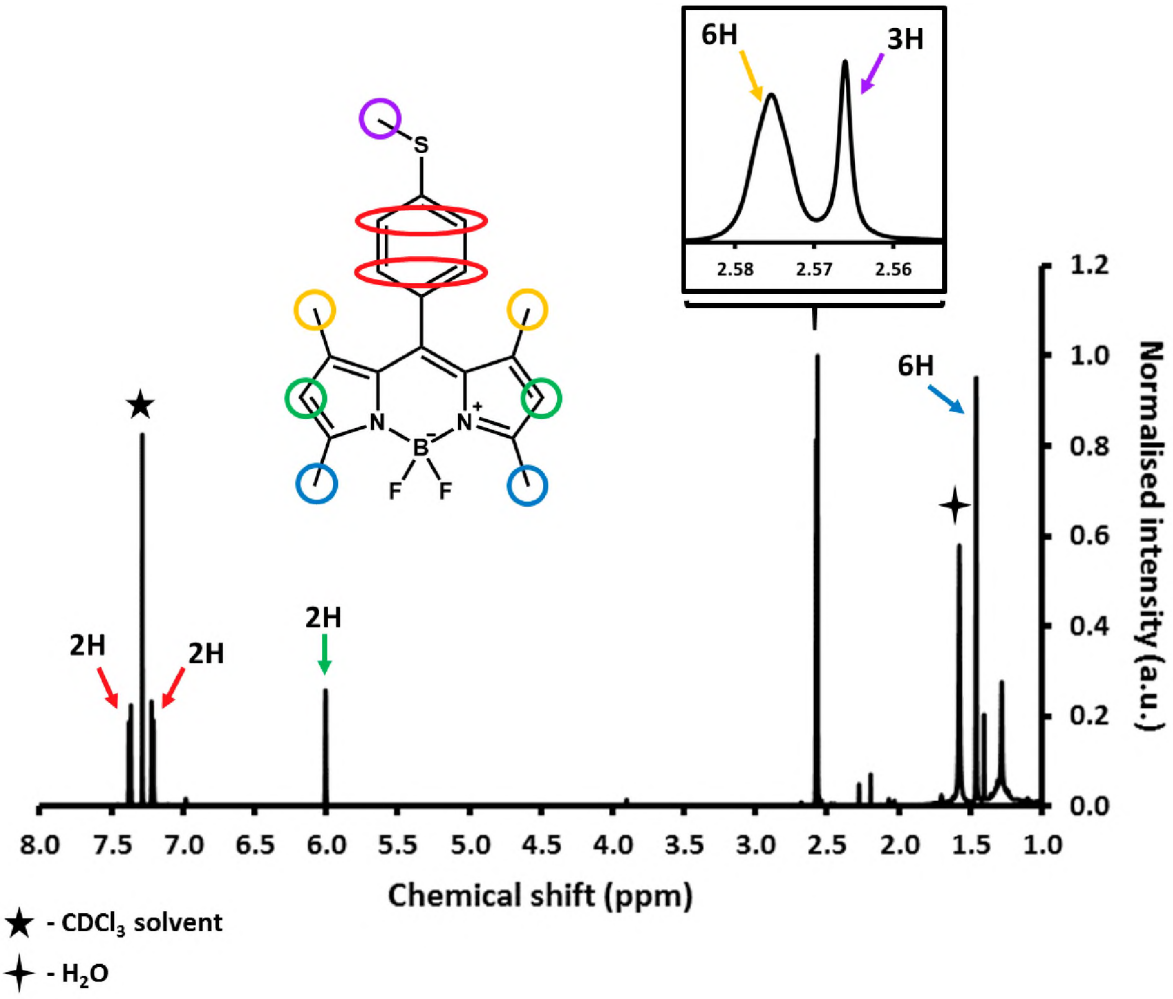

Figure 31. ^1H NMR spectrum of BODIPY **(5)** in $CDCl_3$ with an expansion (inset), showing peak assignments. The stars indicate the solvent and water peaks, respectively.

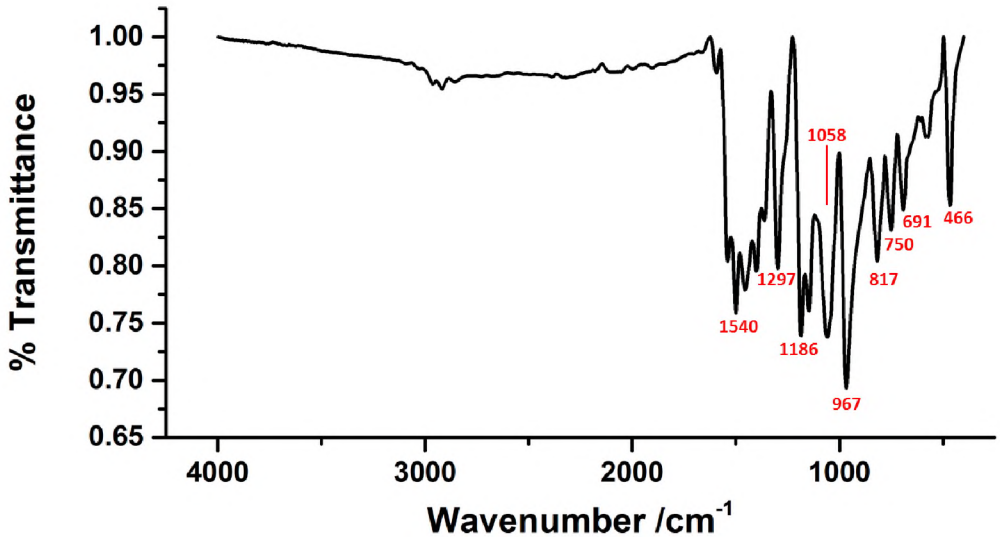

Figure 32. The FT-IR spectrum of BODIPY **(5)**, highlighting the BODIPY vibrational skeleton.

3.5.4 Spectroscopic properties of BODIPY **(5)**

The electronic absorption spectrum for BODIPY **(5)** is typical of that of a *meso*-substituted BODIPY, with an absorbance maximum at 502 nm in DMSO (**Fig. 33**). **Table 7** summarises the absorption, excitation and emission band wavelength maxima for BODIPY **(5)** in three different solvents. BODIPY **(5)** is highly soluble in a range of solvents, and did not show signs of aggregation. A small blue shift of the main spectral bands was observed when moving from DMSO (polarity index = 7.2) to the less polar ethanol (polarity index = 5.2). The emission spectrum of **(5)** is typical for a tetra-methyl BODIPY (**Fig. 33**) [2]. BODIPY **(5)** is highly fluorescent due to its rigid π-system, which limits the rate of nonradiative decay, and its lack of ISC [2]. The low rate of ISC also results in a very low singlet oxygen quantum yield (**Table 7**), which is typical of non-halogenated BODIPYs.

Table 7 also shows the log ε value for BODIPY **(5)** in DMF, which was calculated from the increase in absorbance with concentration, using the Beer-Lambert law (**Fig. 34**).

Table 7. Photophysical data for BODIPY **(5)**.

Solvent	log ε	λ_{abs} /nm	λ_{exc} /nm	λ_{em} /nm	Δ Stokes /nm	Φ_F ± 0.01	τ_F /ns[a]	Φ_Δ
DMSO	–	502	501	515	14	0.61	2.18 (0.97) 13.62 (0.03)	0.08
DMF	4.88	501	501	512	11	–	–	–
Ethanol	–	500	500	510	10	–	–	–

[a] Abundances in brackets

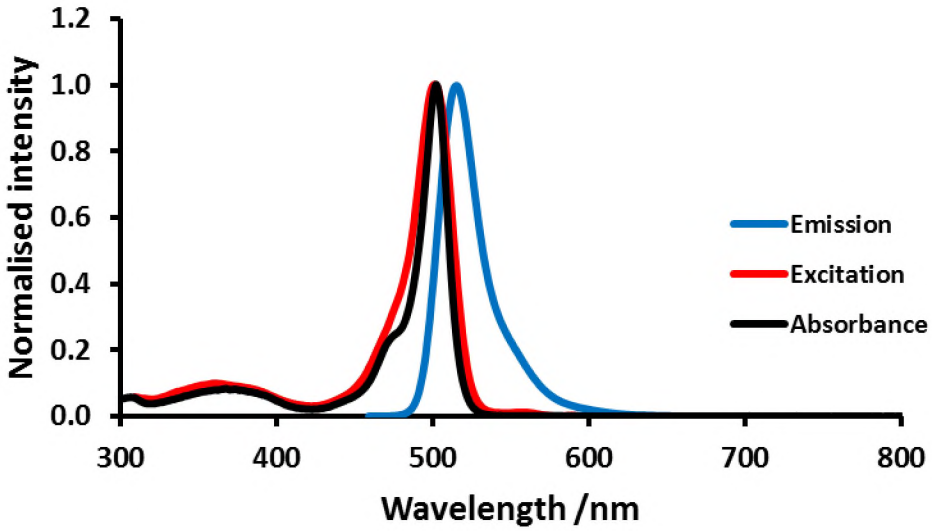

Figure 33. Normalised absorption (*black*), excitation (*red*) and emission (*blue*) spectra of BODIPY **(5)** in DMSO.

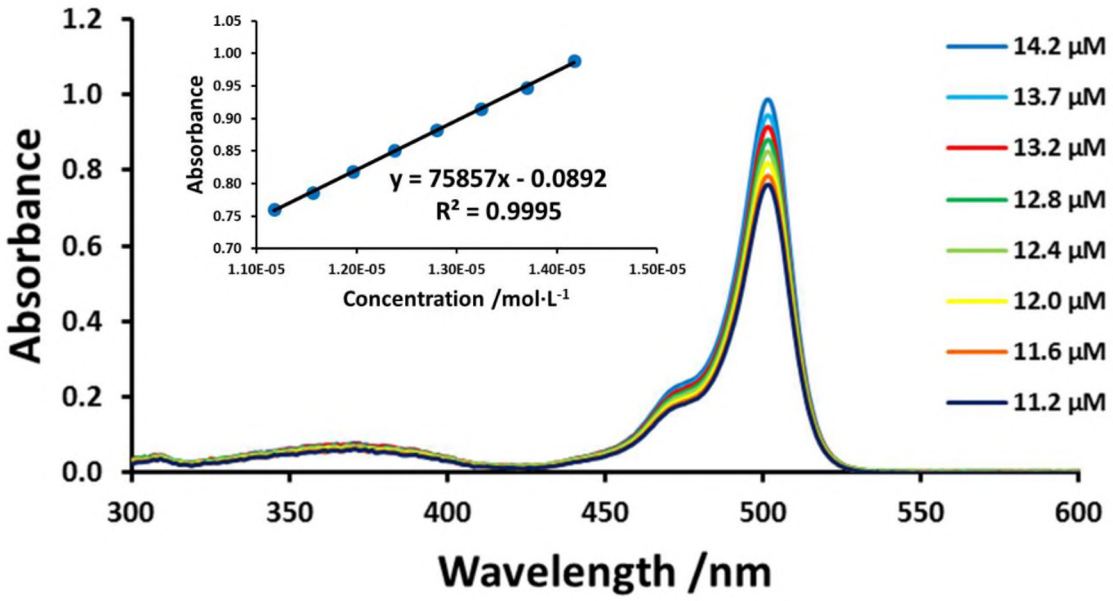

Figure 34. UV-visible absorption spectral changes with concentration for BODIPY **(5)** from 11.2–14.2 µM in DMF. The inset shows the increase of the BODIPY main spectral band intensity with concentration, and is used to calculate log ε for **(5)**.

3.6 4,4'-Difluoro-8-(4-methylthiophenyl)-1,3,57-tetramethyl-2,6-dibromo-4-bora-3a,4a-diaza-*s*-indacene **(6)**

3.6.1 Synthesis of BODIPY **(6)**

Halogenation of the BODIPY core is a simple method whereby the spectroscopic properties of the molecule may be tuned, and the ability to generate singlet oxygen may be introduced. The 2,6-positions of a tetramethyl BODIPY have been shown to be the most vulnerable to nucleophilic attack [58]. Hence, BODIPY **(6)**, a novel compound, was synthesised *via* bromination of **(5)** using N-bromosuccinimide (NBS), according to the same procedure employed in the formation of BODIPY **(2)**.

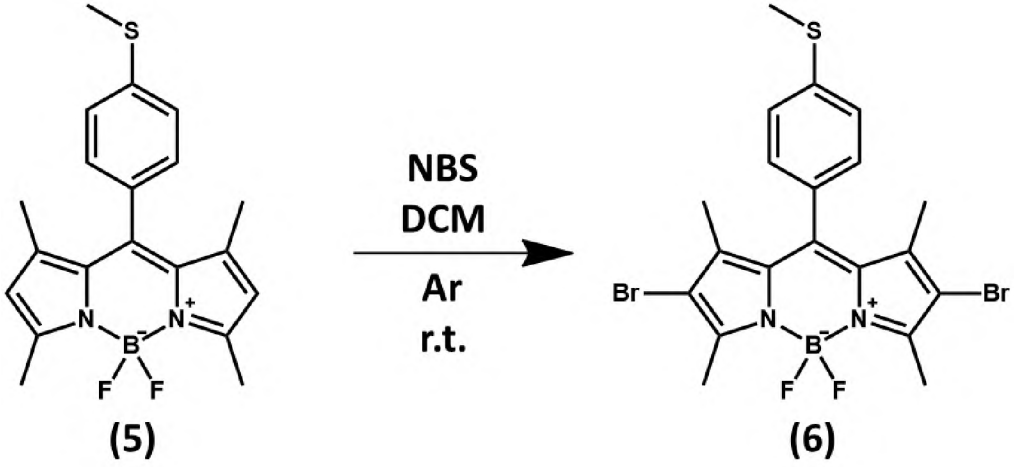

(5) **(6)**

Scheme 16. Synthesis of 4,4'-Difluoro-8-(4-methylthiophenyl)-1,3,5,7-tetramethyl-2,6-dibromo-4-bora-3a,4a-diaza-*s*-indacene **(6)** *via* nucleophilic addition of bromine to BODIPY **(5)**.

3.6.2 Structural analysis of BODIPY **(6)**

All nineteen protons can be readily identified in the ^{1}H NMR spectrum of BODIPY **(6)** (**Fig. 35**). The singlet at 2.57 ppm, integrating to 3 protons, is attributed to the methyl group attached to sulphur at the *para*-position of the *meso*-phenyl. The two doublets between 7.18–7.39 ppm each integrate as two protons and can hence be attributed to the four phenyl protons. The singlets at 2.62 and 1.45 ppm each integrate to 6 protons. The singlet at 2.62 ppm may be attributed to the methyl groups positioned adjacent to the *meso*-phenyl, while the singlet occurring upfield at 1.45 ppm is attributed to the methyl groups at the 3,5-positions, which experience shielding due to their proximity to the pyrrolic nitrogens. The absence of the singlet at 6.00 ppm confirms that the hydrogen atoms present at the 2,6-positions of BODIPY **(5)** have been replaced with bromine atoms (**Fig. 35**). The peak at 5.32 ppm integrates to a mere 0.18 and is likely due to some small impurity.

Red crystals of BODIPY **(6)** were obtained (**Fig. 36**). CHNS elemental analysis for this compound was in good agreement with expected values. The FT-IR spectrum for BODIPY **(6)** shows two C–Br stretch bands in the 523–691 cm^{-1} region, confirming incorporation of bromine atoms into the BODIPY core. However, BODIPY **(6)** displays broadly similar vibrations to that of BODIPY **(5)**, confirming that the BODIPY core remains intact upon bromination. The predicted molecular mass of 528.06 for BODIPY **(6)** was confirmed by MALDI-TOF mass spectrometry as the primary peak occurred at 528.64.

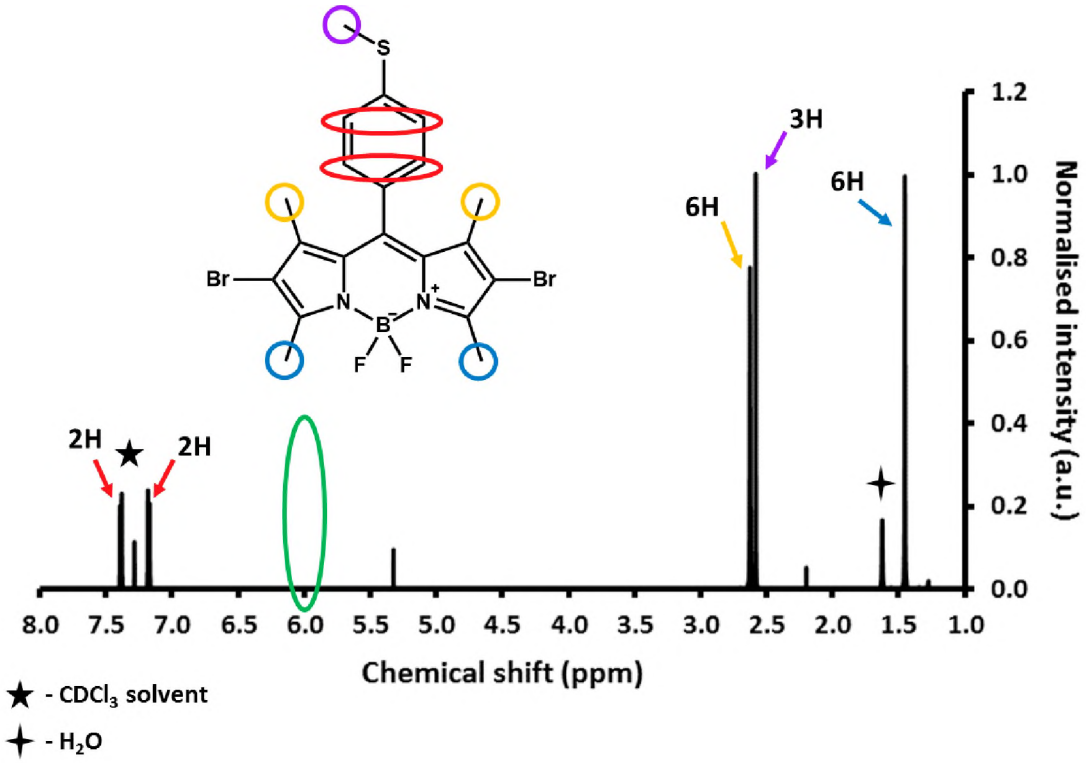

Figure 35. ^{1}H NMR spectrum of BODIPY **(6)** in $CDCl_3$, highlighting the disappearance of the peak at a chemical shift of 6.00 ppm. The stars indicate the solvent and water peaks, respectively.

Figure 36. Red crystals of BODIPY **(6)** under ambient light.

3.6.3 Spectroscopic properties of BODIPY **(6)**

The electronic absorption spectrum for BODIPY **(6)** is typical of a BODIPY dye, with the absorbance maximum occurring at 528 nm in DMSO (**Fig. 37**). However, the absorption maximum is red-shifted by ca. 30 nm when compared to its parent dye, BODIPY **(5)**. Attachment of bromine atoms at the 2,6-positions causes a destabilisation of the HOMO with respect to the LUMO, resulting in a reduced HOMO–LUMO gap, and hence a red shift of the main spectral bands. **Table 8** summarises the absorption, excitation and emission band wavelength maxima for BODIPY **(6)** in three different solvents. It also shows the log ε value for BODIPY **(6)**, which was calculated from the increase in absorbance with concentration, using the Beer-Lambert law (**Fig. 38**). BODIPY **(6)** is highly soluble in a range of solvents, and did not show signs of aggregation. A small blue shift of the main spectral bands was observed when moving to less polar solvents.

The presence of bromine atoms at the 2,6-positions of BODIPY **(6)** increases the rate of ISC by relaxation of the spin-selection rule due to the heavy atom effect. This, in turn, increases the ability of the BODIPY dye to produce singlet oxygen. Hence, BODIPY **(6)** shows a significantly higher Φ_Δ value than BODIPY **(5)** (**Table 8**). The singlet oxygen quantum yield of BODIPY **(6)** was determined by monitoring the photocatalytic degradation of DPBF in the presence of BODIPY **(6)** in ethanol (**Fig. 39**). BODIPY **(6)** showed excellent photostability (**Fig. 39**), which was even better than that of the standard, Rose Bengal. Due to the very low fluorescence quantum yield of BODIPY **(6)** in DMSO, the fluorescence lifetime was not determined.

Table 8. Photophysical data for BODIPY **(6)**.

Solvent	**log ε**	**λ_{abs} /nm**	**λ_{exc} /nm**	**λ_{em} /nm**	**Δ Stokes /nm**	**Φ_F ± 0.01**	**τ_F /ns**	**Φ_Δ**
DMSO	5.03	528	528	547	19	0.03	n.d[a]	–
DMF	5.04	527	527	543	16	–	–	–
Ethanol	–	526	526	540	14	–	–	0.79

[a] Not determined

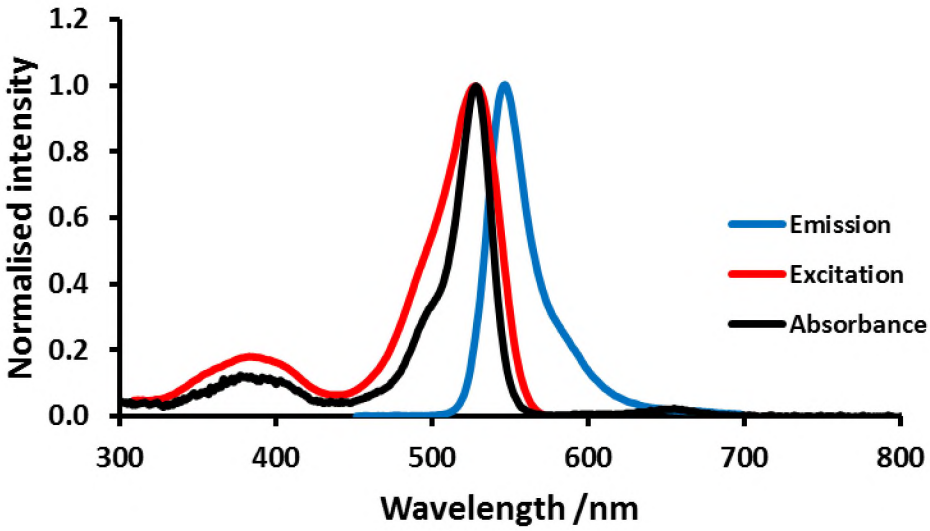

Figure 37. Normalised absorption (*black*), excitation (*red*) and emission (*blue*) spectra of BODIPY **(6)** in DMSO.

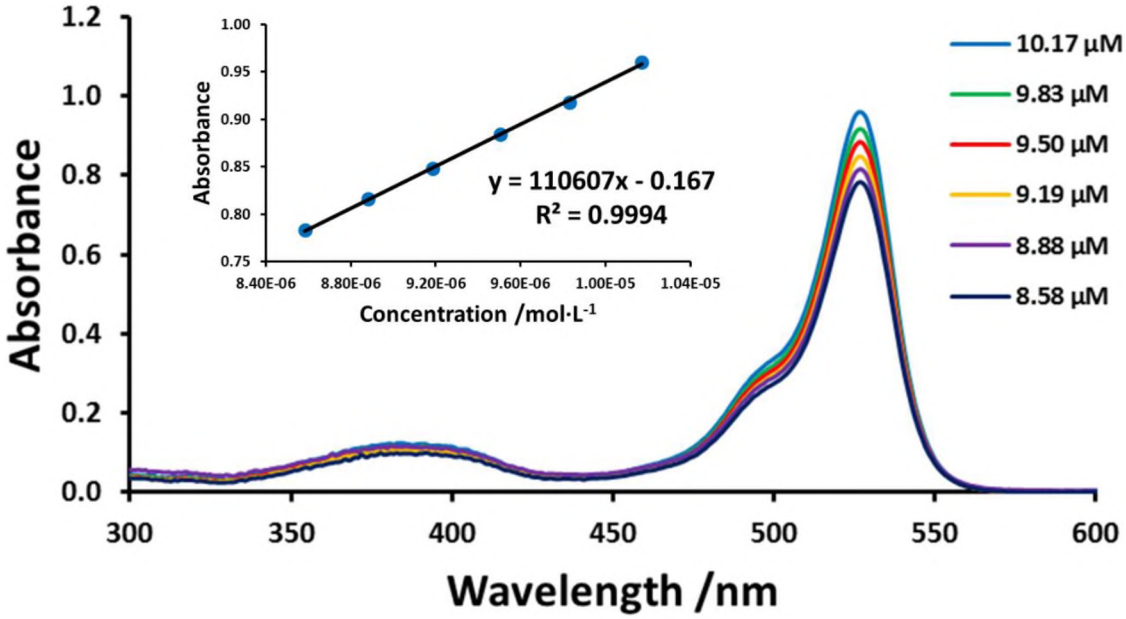

Figure 38. UV-visible absorption spectral changes with concentration for BODIPY **(6)** from 8.58–10.17 µM in DMF. The inset shows the increase of the BODIPY main spectral band intensity with concentration.

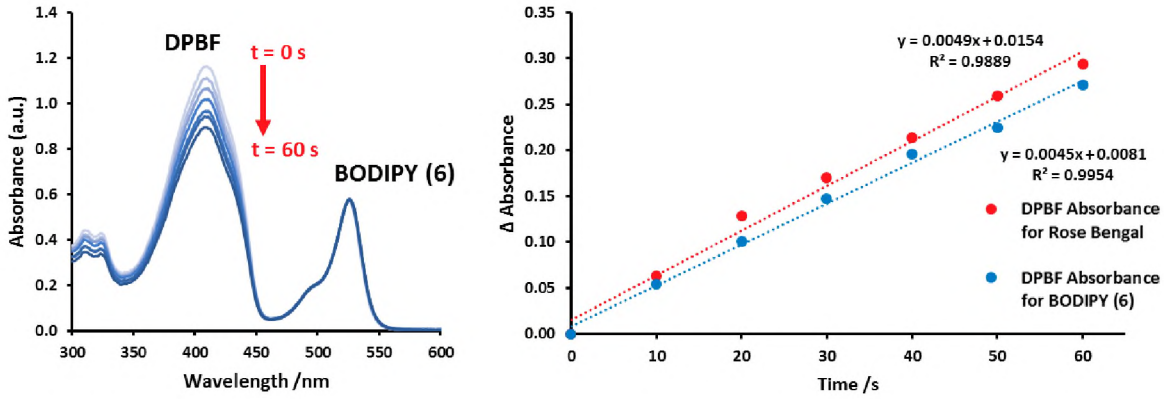

Figure 39. Photocatalytic degradation of DPBF (λ_{max} = 410 nm) in EtOH by BODIPY **(6)** (λ_{max} = 526 nm) at 10 s intervals, indicative of singlet oxygen generation (*left*). The Φ_{Δ} value for **(6)** is determined using the comparative method with Rose Bengal (Φ_{Δ} = 0.86 [27, 125]) as standard (*right*).

3.7 4,4'-Difluoro-8-(4-methylthiophenyl)-1-methyl-2,6-dibromo-3,5,7-tri-styryl-4-bora-3a,4a-diaza-*s*-indacene **(7b)**

3.7.1 Synthesis of BODIPYs **(7a)** and **(7b)**

BODIPY **(7)** was synthesised using a modified Knoevenagel condensation reaction [7, 61, 64] (**Scheme 17**), as a potential candidate for use in PDT. The reaction is conducted in dry conditions. However, as water is formed as a by-product of the reaction, a Dean-Stark trap was used for the azeotropic removal of water. The reaction yielded a number of distinct, brightly coloured fractions (**Fig. 40** and **Fig. 41**). BODIPYs **(7a)** and **(7b)** were obtained by column chromatography using ethyl acetate/ petroleum ether (1:9) as eluent. BODIPY **(7a)** was afforded as a blue powder, while BODIPY **(7b)** was obtained as a green-blue powder.

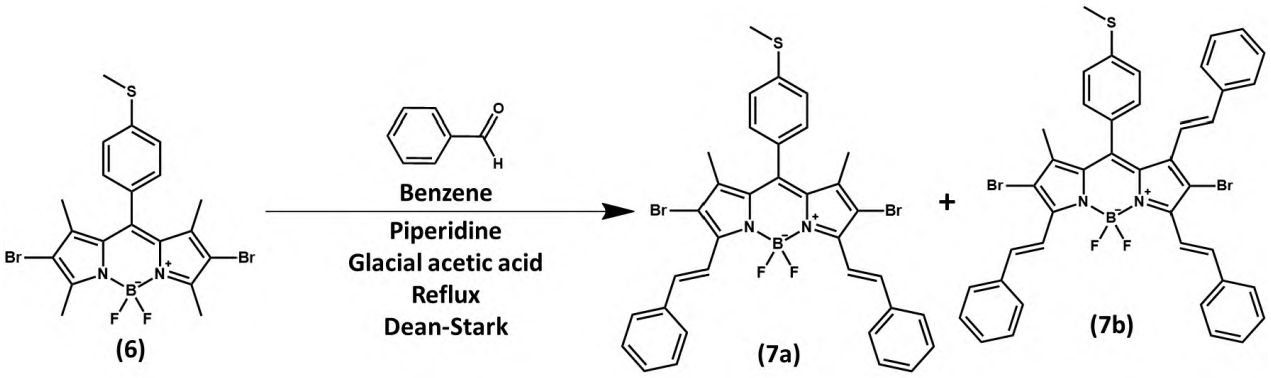

Scheme 17. Knoevenagel condensation of benzaldehyde and **(6)** resulting in the synthesis of di-**(7a)** and tri-**(7b)** styryl BODIPY dyes.

Figure 40. Fractions of the reaction mixture (*top*) and corresponding TLC plates (*bottom*) of BODIPY **(7)**. The fractions containing the leading blue spots were further purified to yield BODIPY **(7a)**, while the lagging green-blue spots were further purified to yield BODIPY **(7b)**.

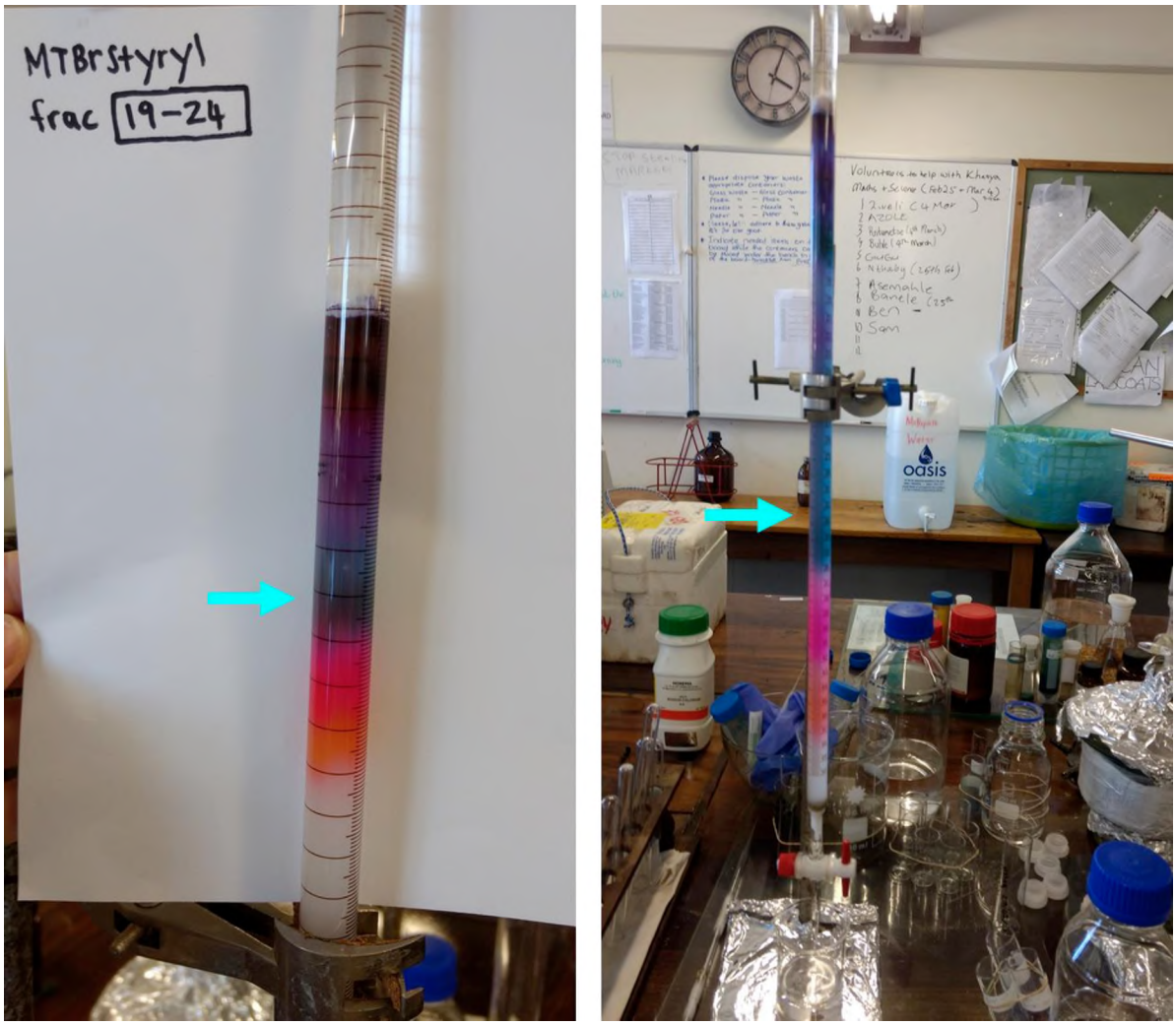

Figure 41. The fractions containing the leading blue spots highlighted in **Fig. 40** were further purified by column chromatography using silica gel, with ethyl acetate/ petroleum ether (1:9) as eluent to yield BODIPY **(7a)**.

3.7.2 Structural analysis of BODIPY **(7a)**

All twenty-seven protons can be readily identified in the ^{1}H NMR spectrum of BODIPY **(7a)**. In the aromatic region, in the range of 8.2–7.2 ppm, there are five doublets and one multiplet, which all integrate to give 18 protons – the expected number of protons for this region.

The remaining protons are accounted for by singlets at 2.60 and 1.52 ppm. The singlet at 2.60 ppm integrates to 3 protons and is attributed to the S-methyl group present at the *para*-position of the *meso*-phenyl, while the singlet at 1.52 ppm, integrating to 6 protons, is assigned to the 1, 7-methyl groups. The solvent residual peak of $CDCl_3$ occurs at 7.28 ppm, and the H_2O peak is visible at 1.60 ppm.

The predicted molecular mass of 704.27 for BODIPY **(7a)** was confirmed by MALDI-TOF mass spectrometry, as the primary peak occurred at 704.51. As there are multiple points at which fragmentation can occur, it is not unexpected that the mass spectrum shows a fairly large number of peaks.

3.7.3 Spectroscopic properties of BODIPY **(7a)**

The electronic absorption spectrum for BODIPY **(7a)** is typical of a BODIPY dye, with the absorbance maximum occurring at 641 nm in DMSO (**Fig. 42**). The absorption maximum of BODIPY **(7a)** is red-shifted by ca. 139 nm when compared to its parent dye, BODIPY **(5)**, and by 113 nm with respect to BODIPY **(6)**. As the main spectral bands of BODIPY **(6)** are red-shifted to the edge of the therapeutic window, it was thought to have potential for use in PDT. However, BODIPY **(7a)** displayed a very low singlet oxygen quantum yield (**Table 9**), which was unexpected based on the promising Φ_{Δ} value obtained for its precursor, BODIPY **(6)**.

Table 9 summarises the absorption, excitation and emission band wavelength maxima for BODIPY **(7a)** in DMSO, DMF and ethanol. The spectral maxima of BODIPY **(7a)** varied by up to 9 nm, depending on the solvent used.

Table 9. Photophysical data for BODIPY **(7a)**.

Solvent	log ε	λ_{abs} /nm	λ_{exc} /nm	λ_{em} /nm	Δ Stokes /nm	Φ_F ± 0.01	τ_F /ns	Φ_Δ
DMSO	–	641	641	659	18	0.47	3.40	–
DMF	3.99	640	640	656	16	–	–	–
Ethanol	–	637	636	650	14	–	–	0.03

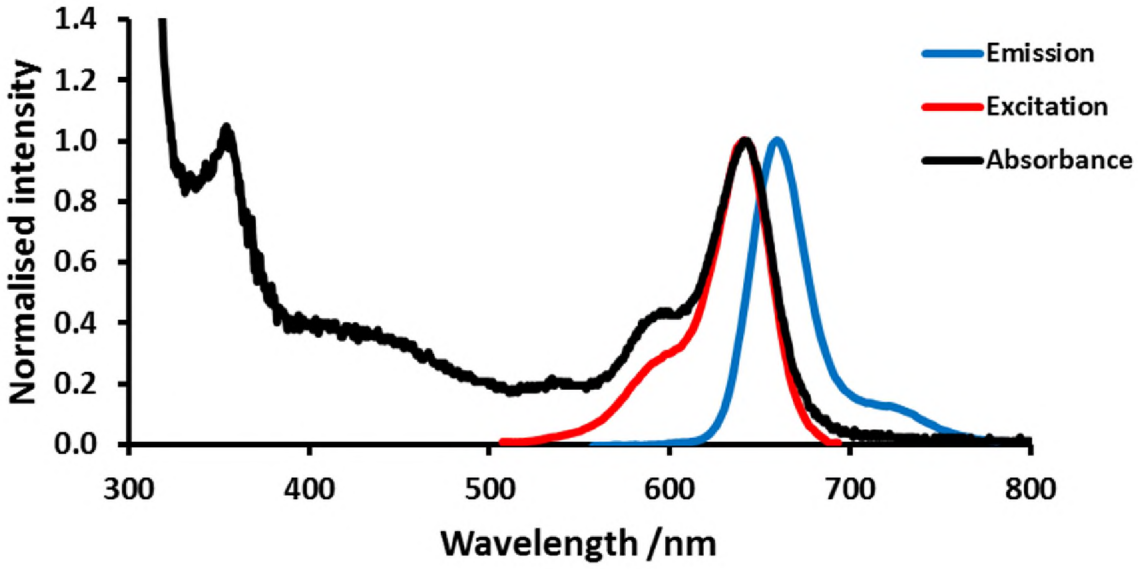

Figure 42. Normalised absorption (*black*), excitation (*red*) and emission (*blue*) spectra of BODIPY **(7a)** in DMSO.

3.7.4 Structural analysis of BODIPY **(7b)**

All thirty-one protons can be readily identified in the ^{1}H NMR spectrum of BODIPY **(7b)** (**Fig. 43**). The peaks present in the aromatic region, in the range of 8.2–6.8 ppm, integrate to give 18 protons – the expected number of protons for this region. The remaining protons are accounted for by singlets at 2.43 and 1.39 ppm. The singlet at 2.43 ppm integrates to 3 protons and is attributed to the S-methyl group present at the *para*-position of the *meso*-phenyl, while the singlet at 1.39 ppm, also integrating to 3 protons, is assigned to the 1-methyl group. The solvent residual peak of $CDCl_3$ occurs at 7.28 ppm, and the H_2O peak is visible at 1.60 ppm.

The predicted molecular mass of 792.38 for BODIPY **(7b)** was confirmed by MALDI-TOF mass spectrometry. Although the primary peak occurred at 794.76 [**(7b)**+2H], there was a peak at 792.74, corresponding to **(7b)** alone. As the structure of BODIPY **(7b)** has multiple points at which fragmentation can occur, the mass spectrum shows several different peaks. Additional peaks correspond to [**(7b)**+Br], for example.

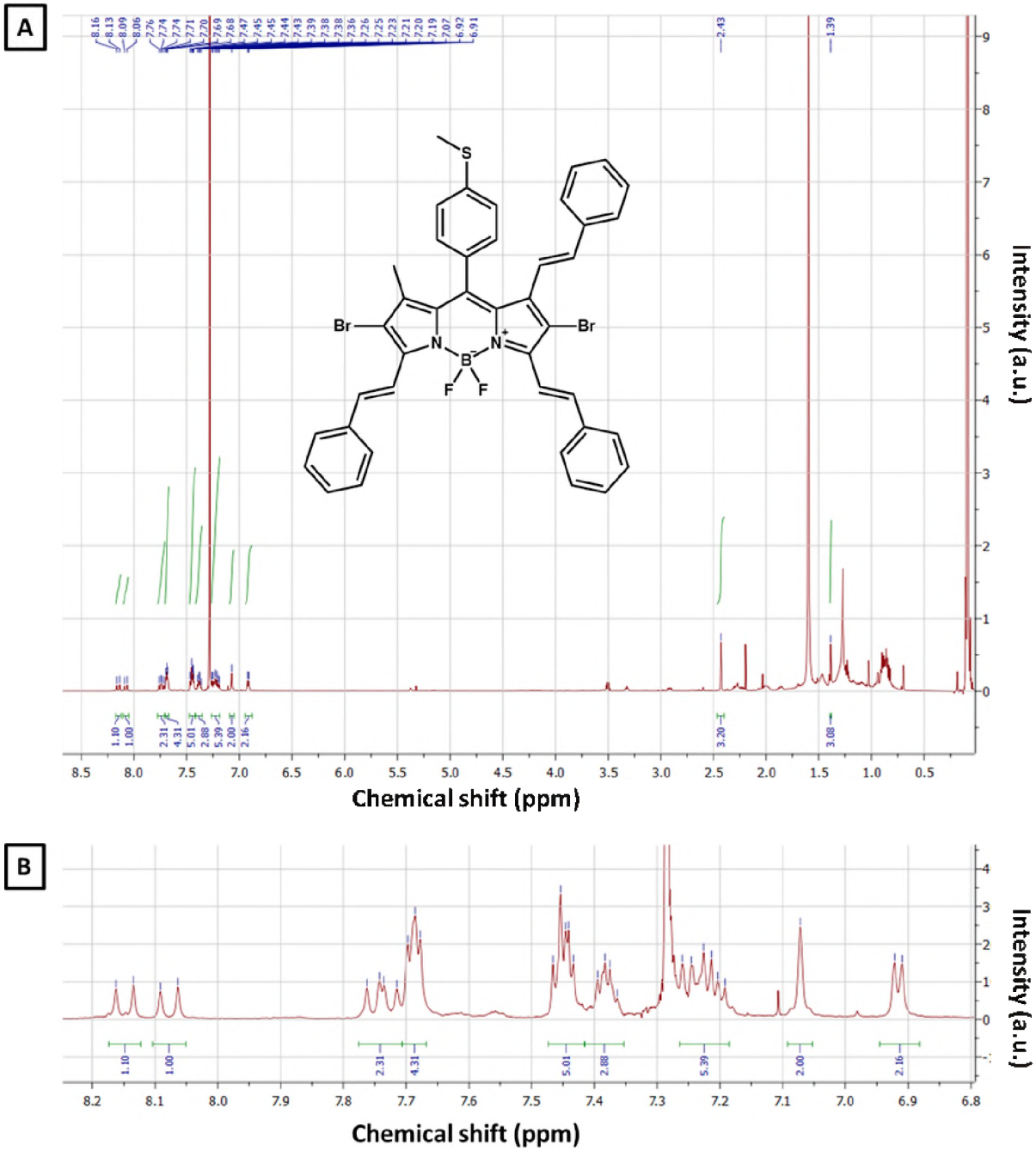

Figure 43. (A) ^{1}H NMR spectrum of BODIPY **(7b)** in $CDCl_3$ with (B) expansion of the aromatic region.

3.7.5 Spectroscopic properties of BODIPY **(7b)**

The electronic absorption spectrum for BODIPY **(7b)** is typical of a BODIPY dye, with the absorbance maximum occurring at 647 nm in DMSO (**Fig. 44**). The absorption maximum of BODIPY **(7a)** is red-shifted by ca. 145 nm when compared to its parent dye, BODIPY **(5)**, and by 119 nm with respect to BODIPY **(6)**. As the main spectral bands of BODIPY **(7b)** are red-shifted to the edge of the biological window, it has potential for use in PDT.

Table 10 summarises the absorption, excitation and emission band wavelength maxima for BODIPY **(7b)** in DMSO, DMF and ethanol. It also shows the log ε value for BODIPY **(7b)** in DMF, which was calculated from the increase in absorbance with concentration, using the Beer-Lambert law (**Fig. 45**). The spectral maxima of BODIPY **(7b)** varied by up to 6 nm, depending on the solvent used.

The singlet oxygen quantum yield of BODIPY **(7b)** was determined by monitoring the photocatalytic degradation of DPBF (**Fig. 46**), using Rose Bengal in EtOH as standard. Although the presence of bromine atoms at the 2,6-positions of BODIPY **(7b)** increases the rate of ISC by relaxation of the spin-selection rule, the singlet oxygen quantum yield of BODIPY **(7b)** (**Table 10**) is not as high as that of BODIPY **(6)** due to the increased molecular flexibility, which allows for more nonradiative decay. However, the Φ_Δ value obtained for **(7b)** was better than that obtained for BODIPY **(7a)**.

Table 10. Photophysical data for BODIPY **(7b)**.

Solvent	**log ε**	**λ_{abs} /nm**	**λ_{exc} /nm**	**λ_{em} /nm**	**Δ Stokes /nm**	**Φ_F ± 0.01**	**τ_F /ns [a]**	**Φ_Δ**
DMSO	–	647	646	665	19	0.14	3.28 (0.99) 0.20 (0.01)	–
DMF	4.25	644	643	665	22	–	–	–
Ethanol	–	641	640	659	19	–	–	0.17

[a] Abundances in brackets

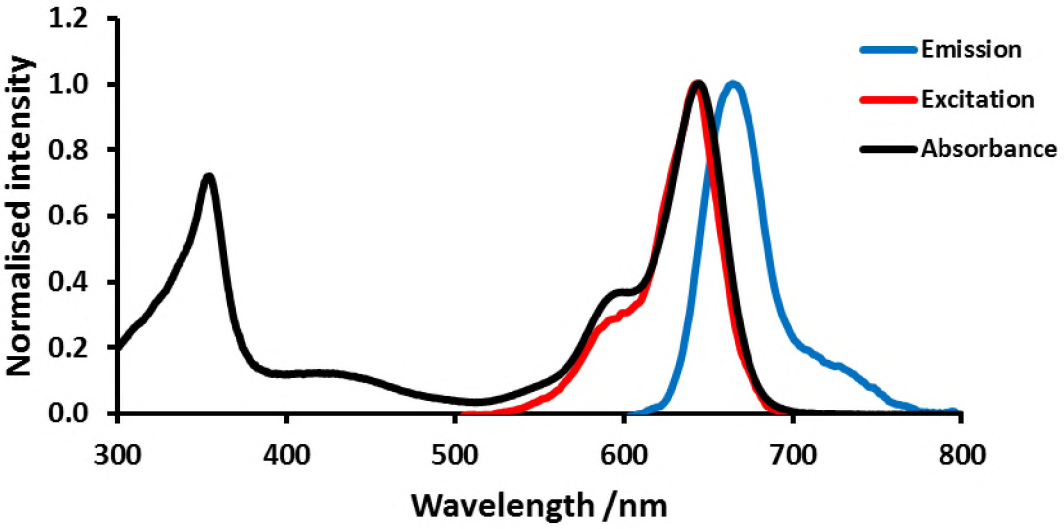

Figure 44. Normalised absorption (*black*), excitation (*red*) and emission (*blue*) spectra of BODIPY **(7b)** in DMF.

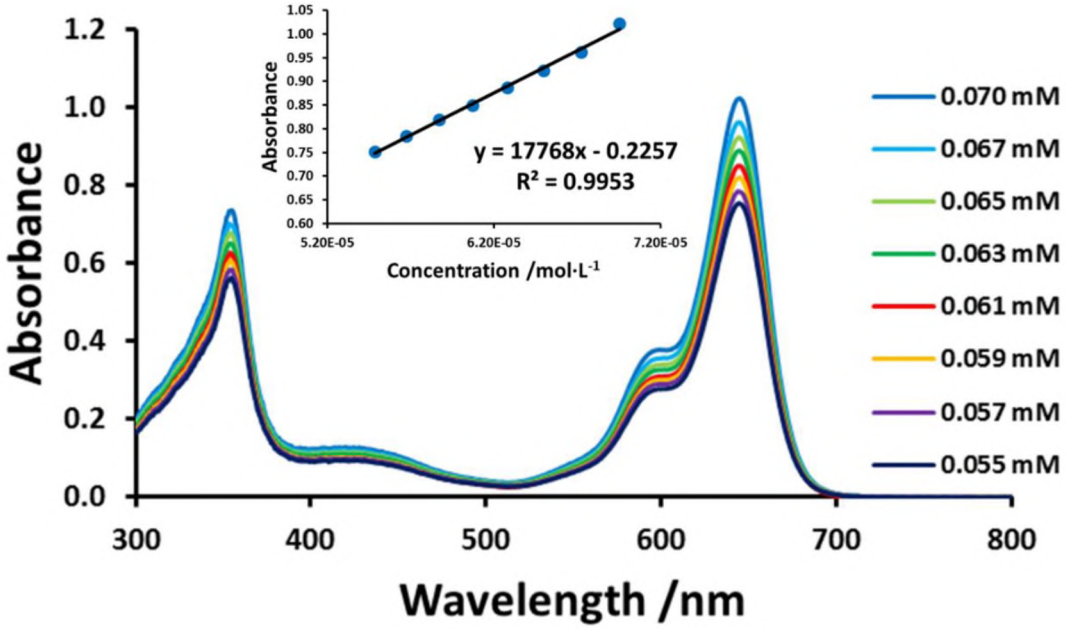

Figure 45. UV-visible absorption spectral changes with concentration for BODIPY **(7b)** from 0.055–0.070 mM in DMF. The inset shows the increase of the BODIPY main spectral band intensity with concentration, and is used to calculate log ε for **(7b)**.

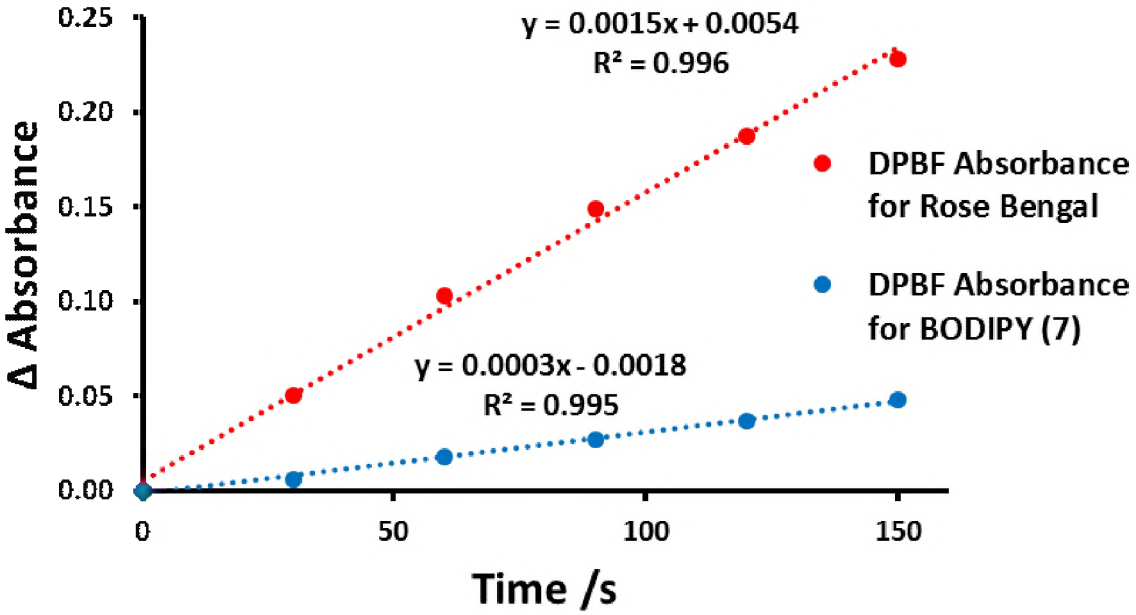

Figure 46. The Φ_Δ value for **(7b)** was determined using the comparative method with Rose Bengal in EtOH (Φ_Δ = 0.86 [27, 125]) as the standard.

3.8 3,5-Dithienylenevinylene BODIPYs: **(8)**, **(9)**, and **(10)**

3.8.1 Synthesis of BODIPYs **(8)**, **(9)**, and **(10)**

BODIPYs **(8–10)** were synthesised by Dr. Lizhi Gai as reported [126].

3.8.2 Structural analysis of BODIPYs **(8)**, **(9)**, and **(10)**

BODIPYs **(8–10)** were characterised using ^{1}H NMR and MALDI-TOF MS. All twenty-three protons are accounted for in the ^{1}H NMR spectrum of BODIPY **(8)** (**Fig. 47**). In the aromatic region, in the range of 8.5–7.0 ppm, there are two multiplets, two doublets, and one doublet of doublets, which together integrate to give 15 protons – the expected number of protons for this region. The singlet at 6.89 ppm integrates to 2 protons and is attributed to the protons at the 2,6-positions, while the singlet at 1.48 ppm, integrating to 6 protons, is attributed to the methyl groups at the 1,7-positions of the BODIPY core. The solvent residual peak of acetone occurs at 2.05 ppm, and the H_2O peak is visible at 2.84 ppm [129, 130].

Similarly, all twenty-five protons of BODIPY **(9)** can be readily identified in its ^{1}H NMR spectrum (**Fig. 48**). In the aromatic region, in the range of 8.5–7.0 ppm, there are a number of peaks, which together integrate to give 14 protons – the expected number of protons for this region. The singlet at 6.91 ppm integrates to 2 protons and is attributed to the protons at the 2,6-positions of the BODIPY core. The appearance of a singlet at 3.98 ppm, integrating to 3 protons, is attributed to the methyl in the -COOMe group present at the *para*-position of the *meso*-phenyl. The remaining singlet, at 1.48 ppm, which integrates to 6 protons, is attributed to the methyl groups at the 1,7-positions of the BODIPY core. The solvent residual peak of acetone occurs at 2.07 ppm, and the H_2O peak is visible at 2.88 ppm [129, 130].

The ^{1}H NMR spectrum of BODIPY **(10)** was obtained in THF due to insufficient solubility in acetone. In the aromatic region, in the range of 8.5–7.0 ppm, there are a number of peaks, which together integrate to give 15 protons – the expected number of protons for this region. The absence of a singlet below 7.0 ppm that integrates to 2 protons confirms that the hydrogen atoms at the 2,6-positions have been replaced. The solvent residual peaks of THF occur at 1.72 and 3.58, while the H_2O peak is visible at 2.54 ppm [130].

The predicted molecular masses of BODIPYs **(8–10)** were confirmed by MALDI-TOF mass spectrometry (**Fig. 49**). The primary peak, in each case, corresponded closely with the expected mass.

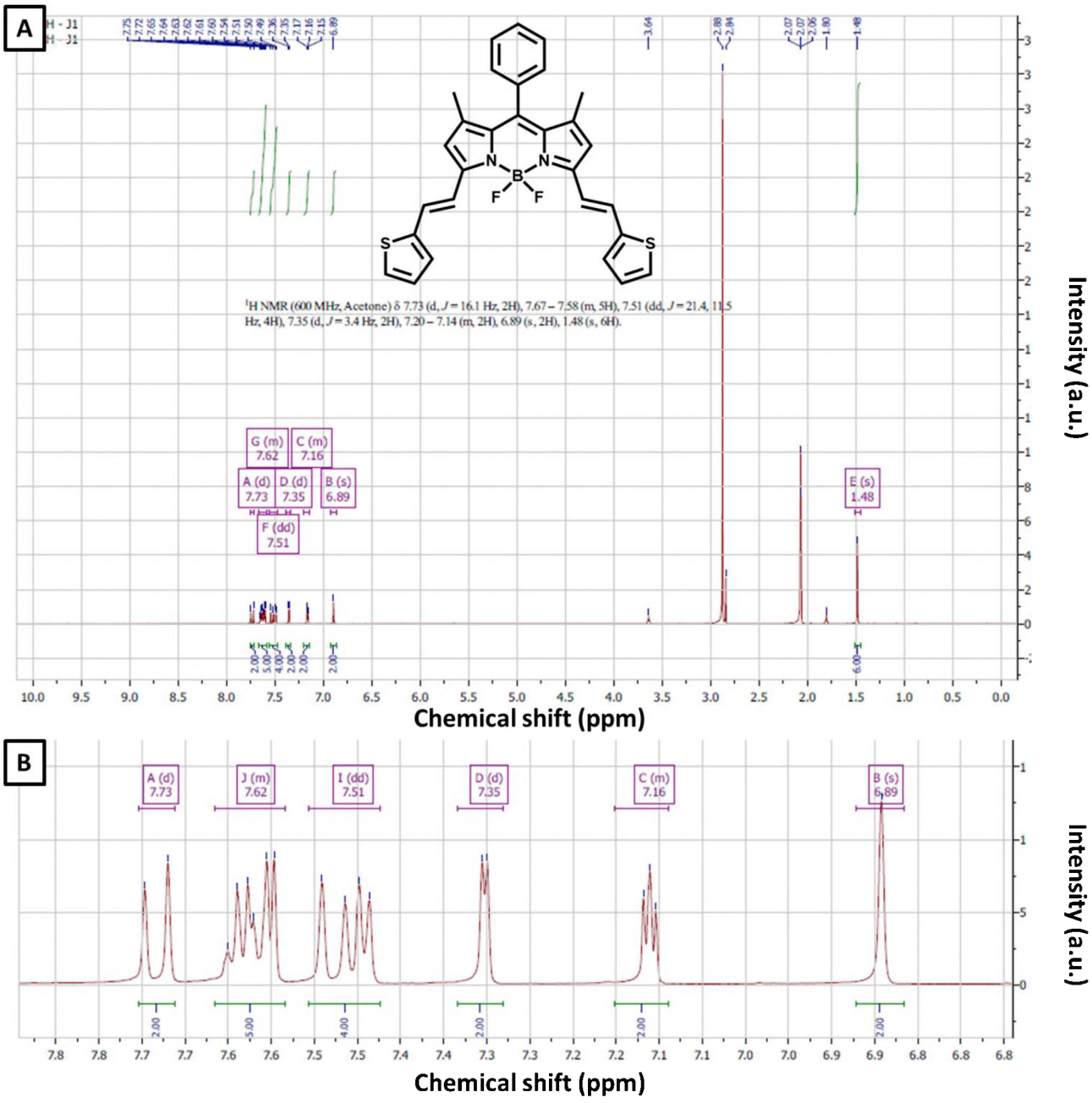

Figure 47. (A) ^{1}H NMR spectrum of BODIPY **(8)** in acetone with (B) expansion of the aromatic region.

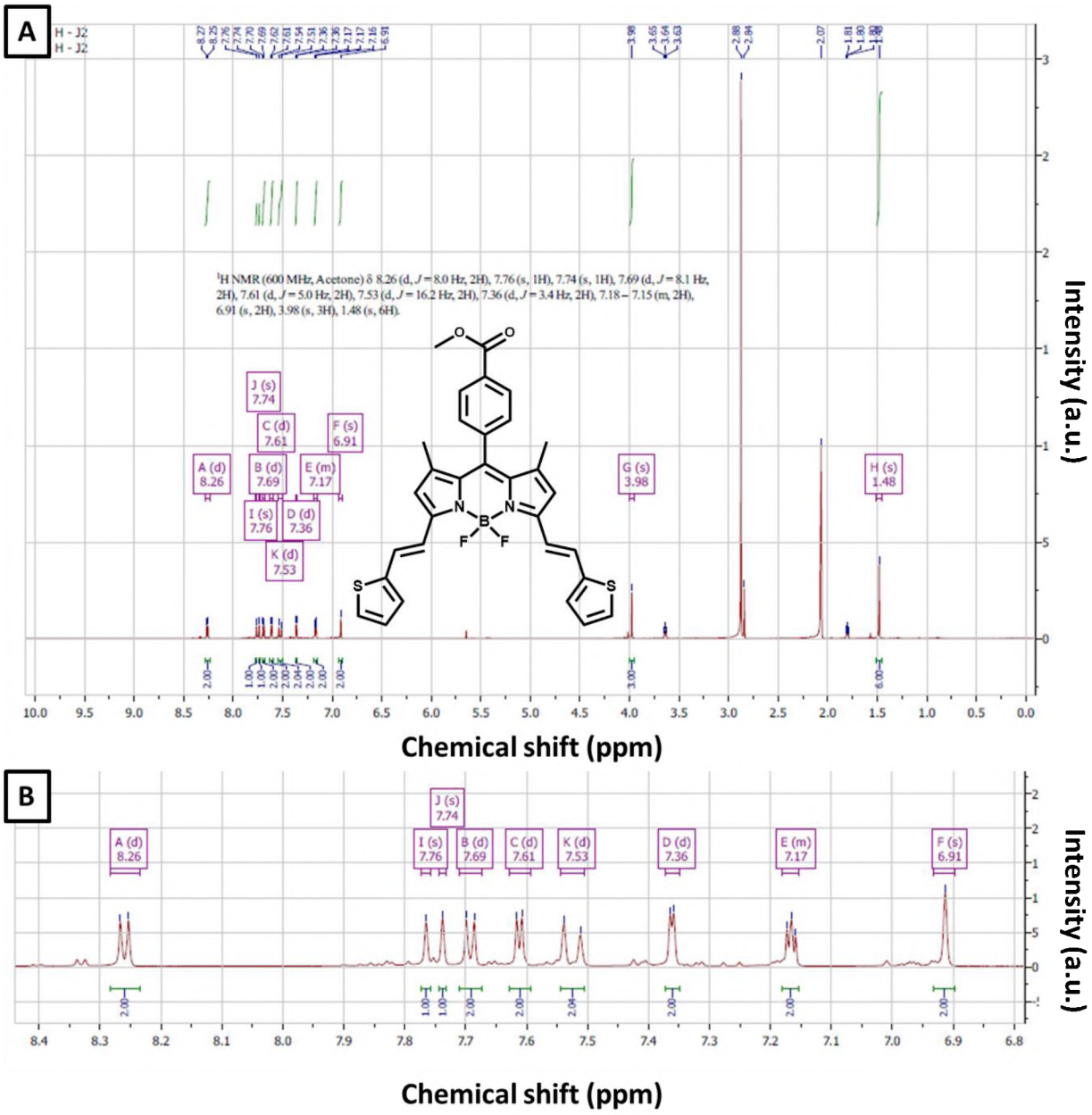

Figure 48. (A) ^{1}H NMR spectrum of BODIPY **(9)** in acetone with (B) expansion of the aromatic region.

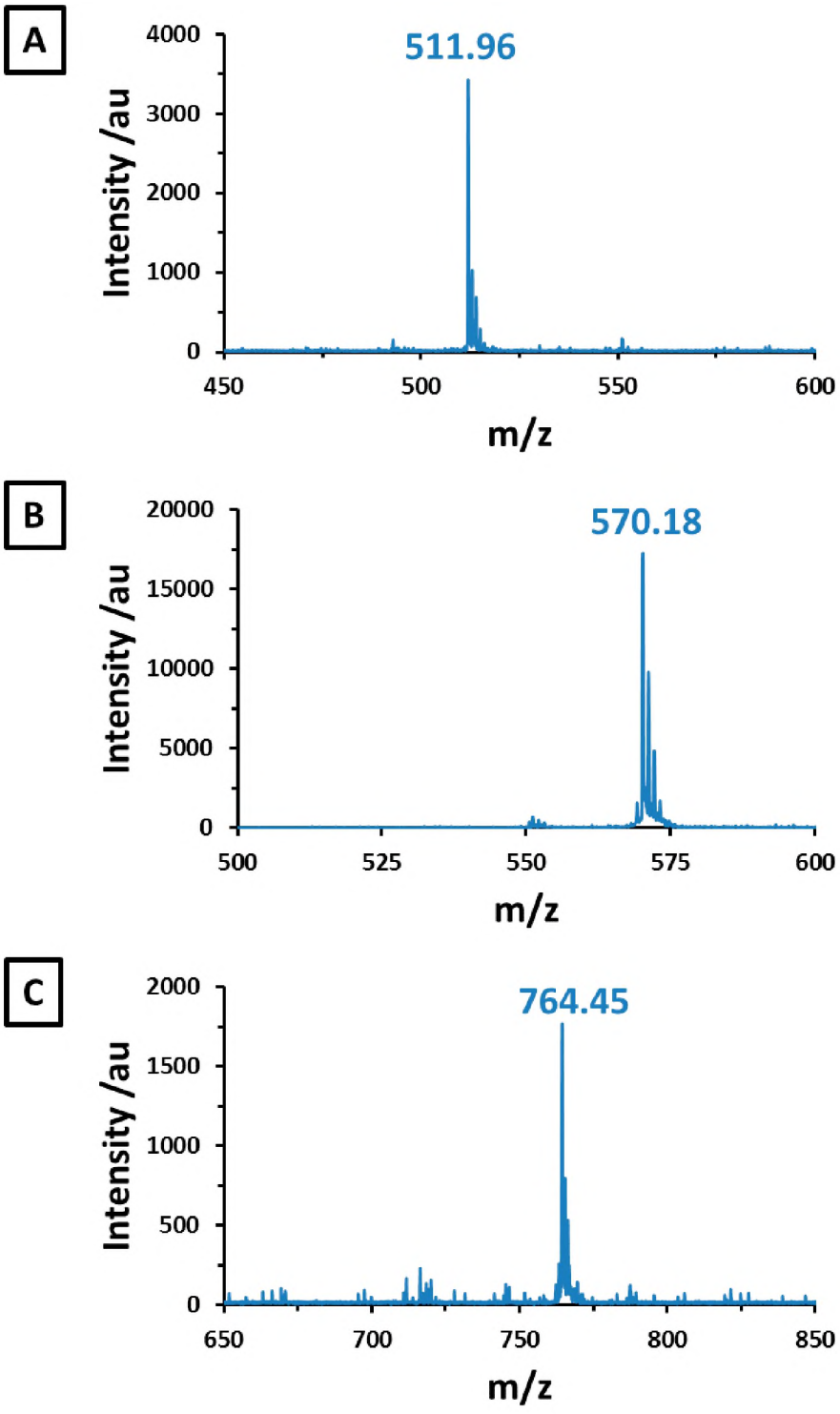

Figure 49. Mass spectra of BODIPYs (A) **(8)**, (B) **(9)**, and (C) **(10)**. The main peaks correspond very closely with the expected masses for each compound.

3.8.3 Spectroscopic properties of BODIPYs **(8)**, **(9)**, and **(10)**

The electronic absorption spectra for BODIPYs **(8–10)** are typical of a BODIPY dye (**Fig. 50**). **Table 11** summarises the absorption, excitation and emission band wavelength maxima for BODIPYs **(8–10)** in DMF. It also shows their log ε values, which were calculated from the increase in absorbance with concentration, using the Beer-Lambert law.

The fluorescence quantum yield of BODIPY **(10)** was significantly lower than those of BODIPYs **(8)** and **(9)**. This is due to the presence of iodine atoms at the 2,6-positions of BODIPY **(10)**, which increases the rate of ISC by relaxation of the spin-selection rule.

Table 11. Photophysical data for 3,5-dithienylenevinylene BODIPYs **(8)**, **(9)**, and **(10)** in DMF.

BODIPY	**log ε**	**λ_{abs} /nm**	**λ_{exc} /nm**	**λ_{em} /nm**	**Δ Stokes /nm**	**Φ_F ± 0.01**	**τ_F /ns [a]**
(8)	5.00	651	651	663	12	0.33	2.89
(9)	5.05	656	656	671	15	0.40	2.87
(10)	4.73	670	670	695	25	0.11	1.62 (0.95) 3.92 (0.05)

[a] Abundances in brackets

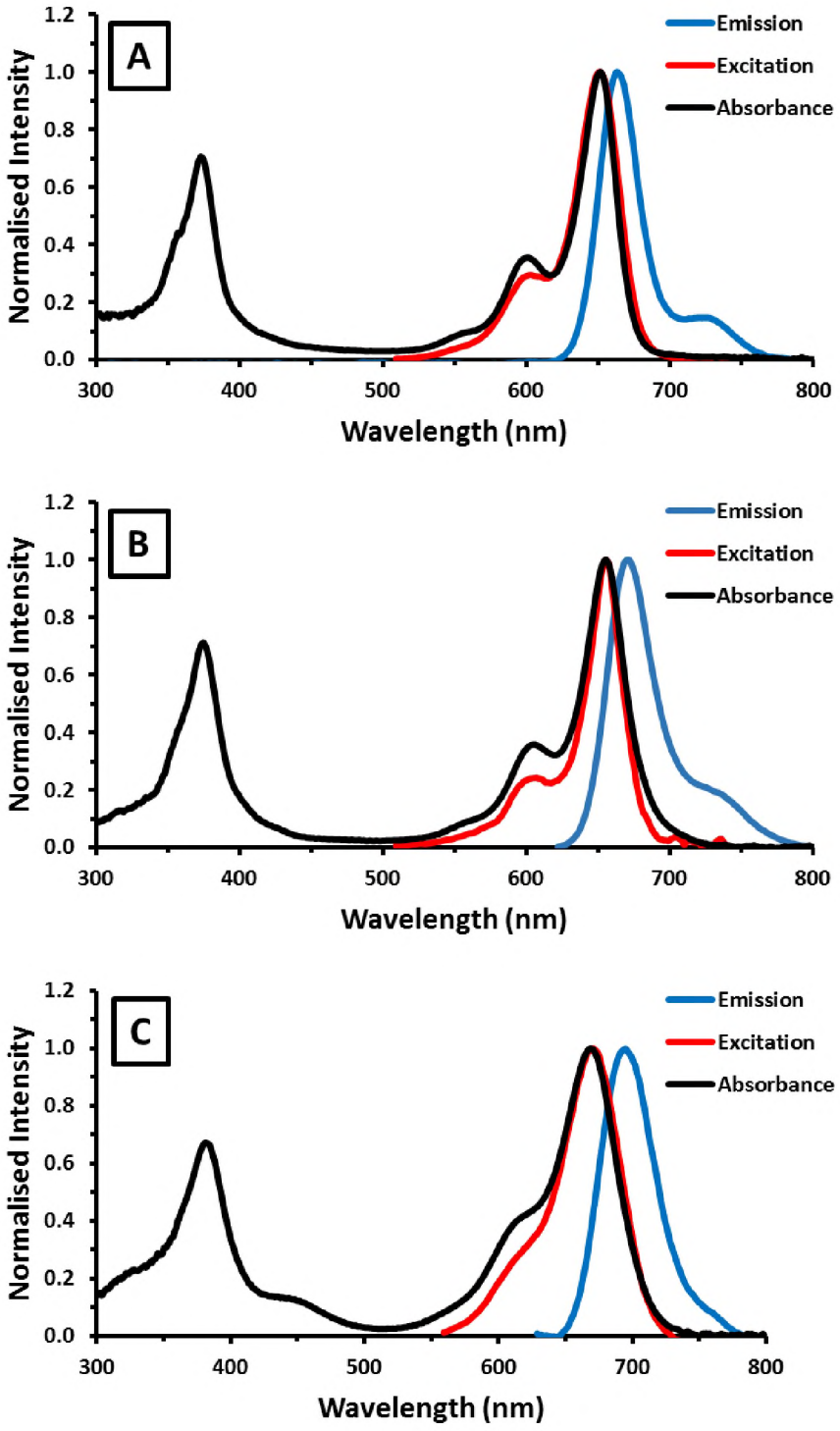

Figure 50. Emission, excitation and absorption spectra of BODIPYs (A) **(8)**, (B) **(9)**, and (C) **(10)**.

3.9 Concluding remarks

Two BODIPY cores, **(1)** and **(5)** were synthesised and characterised using ^{1}H-NMR, CHNS elemental analysis and FT-IR. BODIPY **(1)** was synthesised using the classic "one-pot-three-step" acid catalysed condensation reaction, while BODIPY **(5)** was synthesised *via* the water-method preparation of the corresponding aryldipyrromethane **(5a)**. The only structural difference between these two BODIPYs is that **(1)** has a bromine atom at the 4-position of the *meso*-phenyl, whereas **(5)** has a 4-(methylthio) group at this position. Both **(1)** and **(5)** had high a fluorescence quantum yield, good photostability and negligible singlet oxygen generation capacity. Changing the solvent had very little effect on the main spectral bands of these BODIPY dyes.

Both **(1)** and **(5)** were brominated at the 2,6-positions, yielding BODIPYs **(2)** and **(6)** respectively. BODIPYs **(2)** and **(6)** are red shifted by ca. 30 nm with respect to their parent dyes. BODIPYs **(2)** and **(6)** displayed large singlet oxygen quantum yields that equalled that of the standard, Rose Bengal. Additionally, these BODIPYs showed better photostability than the standard in ethanol, suggesting that they might be useful standards for Φ_{Δ} measurements.

BODIPYs **(2)** and **(6)** were further modified by substitution at the 3,5-positions, *via* a modified version of the Knoevenagel condensation reaction. BODIPY **(2)** was reacted with 3-thiophenecarboxaldehyde to form **(3)** and with 4-(methylthio)benzaldehyde to yield **(4)**, while BODIPY **(6)** was reacted with benzaldehyde to form BODIPYs **(7a)** and **(7b)**. BODIPY **(3)** was characterised using ^{1}H-NMR, MALDI-TOF mass spectrometry and CHNS elemental analysis while BODIPYs **(4)**, **(7a)** and **(7b)** were characterised using ^{1}H-NMR and MALDI-TOF mass spectrometry.

The addition of vinyl/ styryl groups to the BODIPY core causes an increase in fluorescence quantum yield as well as a decrease in singlet oxygen quantum yield with respect to the dibrominated analogues, which was expected – to some degree – as the inclusion of styryl groups introduces pathways for nonradiative decay.

BODIPY **(3)** was red-shifted to the edge of the therapeutic window, at 650 nm, and showed a moderate singlet oxygen quantum yield of 0.28. BODIPY **(4)** was red-shifted to well within the therapeutic window, at 681 nm, and had a Φ_{Δ} value of 0.30. Both BODIPY **(3)** and **(4)** could be of

interest as photosensitisers in PDT, especially if conjugated to gold nanoparticles, which would cause an external heavy atom effect, potentially increasing the Φ_Δ of these compounds. BODIPY **(4)** would be better suited for use in PDT, as its main spectral band is more red-shifted than that of BODIPY **(3)**.

BODIPYs **(7a)** and **(7b)** were red-shifted to the edge of the therapeutic window, at 640 and 641 nm, respectively. Based on the high Φ_Δ values obtained for BODIPY **(6)**, it was thought that its styryl-substituted derivatives might also display high singlet oxygen quantum yields. However, BODIPY **(7a)** showed negligible singlet oxygen production, while BODIPY **(7b)** was marginally better, at 0.17.

3,5-Dithienylenevinylene BODIPYs **(8–10)** were characterised using ^{1}H-NMR and MALDI-TOF mass spectrometry, and their spectroscopic properties were investigated. BODIPY **(10)** has a lower fluorescence quantum yield than BODIPYs **(8)** and **(9)** due to the presence of iodine atoms at the 2,6-positions of the BODIPY core, which promote ISC to the triplet state. The nonlinear absorption properties of BODIPYs **(3)** and **(8–10)** are studied in Chapter 4.

Chapter 4:

Nonlinear optical (NLO) parameters of BODIPY dyes in solution and embedded in polymer thin films

4.1 BODIPYs for NLO studies

It has been demonstrated that π-conjugated systems possess large electronic polarizabilities [77, 135]. Therefore, it is reasonable to expect conjugated molecules to possess substantial second-order hyperpolarizabilities [75, 136, 137]. Additionally, molecules with donor and acceptor moieties that are separated by a π-conjugation system (D–π–A**)** are known to exhibit large third order susceptibility values [138, 139]. In this work, 3,5-dithienylenevinylene BODIPY dyes **(3)** and **(8–10)** were studied to evaluate their potential for optical limiting applications. The electron donating thiophene groups present in BODIPYs **(3)** and **(8–10)** are separated from the BODIPY core (acceptor) *via* a conjugated system. Hence, it was expected that these dyes should show enhanced third order susceptibility values. Extension of the π-conjugation system also shifts the main spectral bands of these BODIPYs to longer wavelengths. As this results in weak absorption at 532 nm, BODIPYs **(3)** and **(8–10)** could potentially be suitable for OL applications where the second harmonic of Nd/YAG lasers is concerned.

4.2 BODIPY–PBC thin films

The ground state absorption spectra of the thin films were obtained in order to visualise the effect of a solid support. **Fig. 51** shows the absorption spectra of BODIPYs **(3)**, **(8)**, **(9)** and **(10)** in DMF and embedded in poly(bisphenol A carbonate) (PBC) as thin films. The DMF spectra show the main absorption bands of the BODIPYs are well defined and do not show signs of aggregation. For BODIPY **(8)**, the DMF spectrum is well-defined but the **(8)–PBC** spectrum shows significant aggregation. The BODIPY-PBC spectra of BODIPYs **(3)**, **(9)** and **(10)** are slightly red-shifted but show that the BODIPYs maintain their electronic character. The red shift is likely as a result of aggregation in the solid support. The average film thickness of the BODIPY-embedded PBC films was determined using SEM (**Fig. 52**).

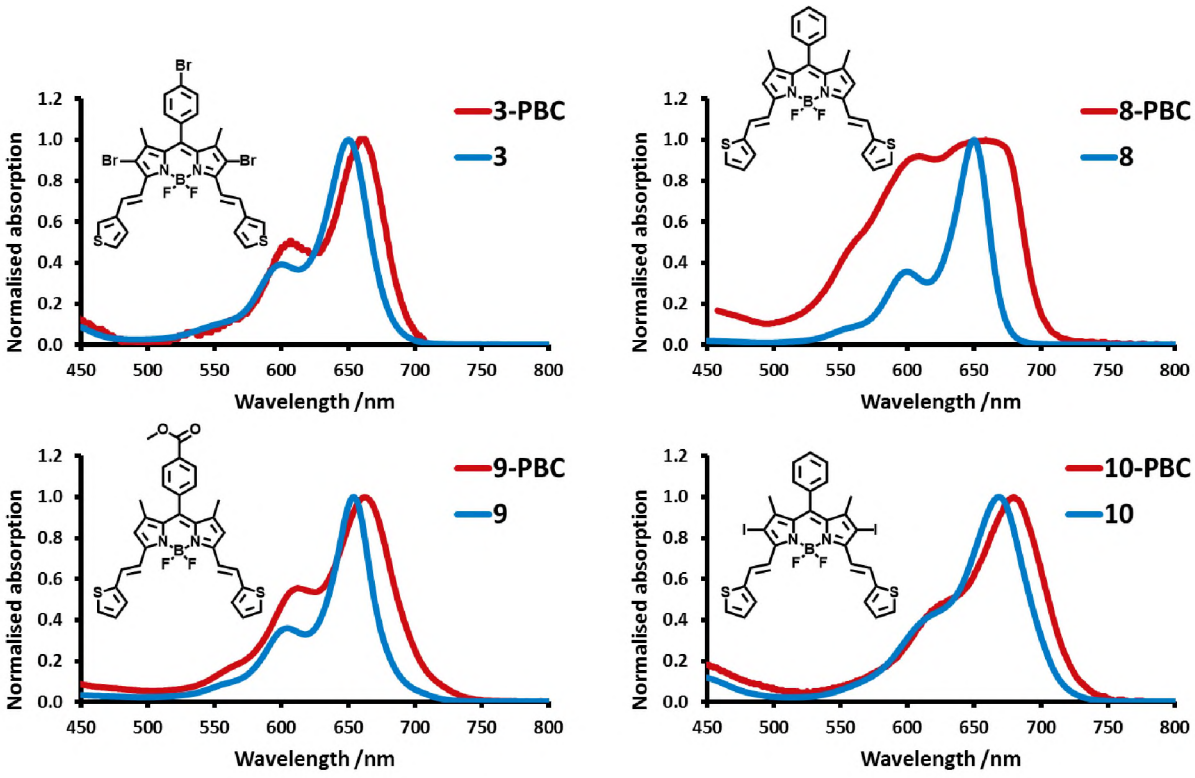

Figure 51. Ground state absorption spectra for BODIPYs **(3)**, **(8–10)** in DMF (*blue*) and when embedded in PBC thin film (*red*).

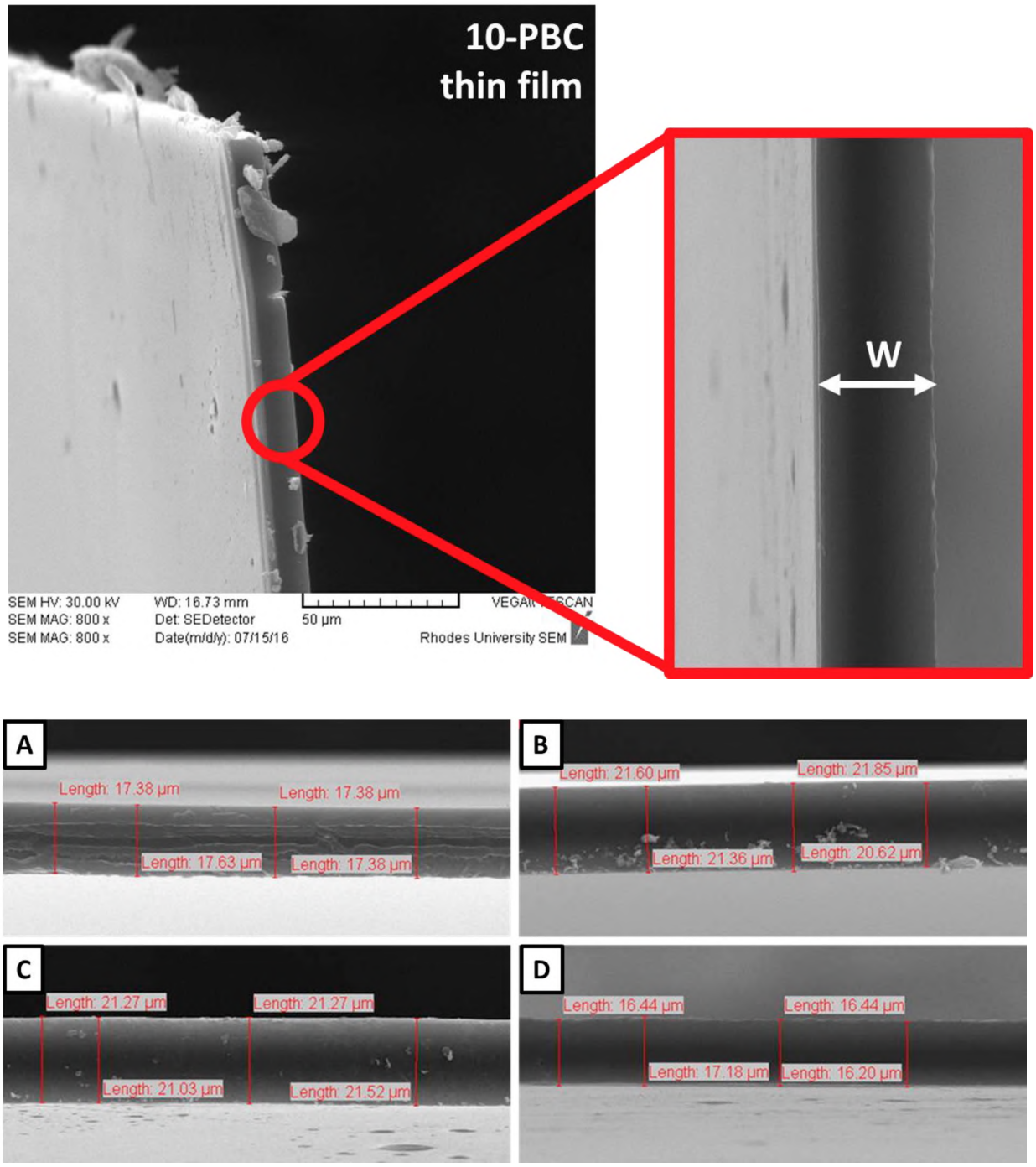

Figure 52. Scanning electron microscopy images of the PBC thin films embedded with BODIPYs. A corner of the **10–PBC** thin film is shown, indicating where the film thickness/ width is measured (*top*). PBC thin films (side view) embedded with BODIPYs (A) **(3)** (average thickness of ca. 17 µm); (B) **(8)** (average thickness of ca. 21 µm); (C) **(9)** (average thickness of ca. 21 µm); and (D) **(10)** (average thickness of ca. 17 µm) (*bottom*).

4.3 Nonlinear optical parameters

Nonlinear optical parameters were determined using the open aperture z-scan setup described in Chapter 2. All studies were carried out in solution as well as in solid state for BODIPYs **(3)** and **(8–10)**. Solution studies were conducted in DMF, which has a high boiling point that allows it to resist differential temperature effects due to the incident laser. For practical optical limiting applications, it is necessary for the BODIPYs to be cast in the solid state. Hence, solid state studies were conducted with BODIPYs embedded in PBC thin films. The optical limiting parameters of BODIPYs **(3)** and **(8–10)** are summarised in **Table 12**. The parameters reported in this work are the nonlinear absorption coefficient (β), the second-order hyperpolarizability (γ) and imaginary third-order susceptibility ($Im[\chi^{(3)}]$); and the optical limiting threshold (I_{lim}). While the efficacy of an optical limiter cannot be determined from a single parameter, γ is particularly useful as it is independent of concentration and can hence be used for meaningful comparison of samples.

4.3.1 Nonlinear absorption coefficient (β)

The nonlinear absorption coefficient (β) measures the degree of nonlinear absorptivity. In molecules where the linear absorption at the laser wavelength of 532 nm is zero, all absorption at that wavelength must be due to 2PA. However, this may be due to sequential ground and excited state absorption (as opposed to concerted 2 photon absorption) [83]. Additionally, as 3,5-dithienylenevinylene BODIPYs **(3)** and **(8–10)** have a small amount of linear absorbance occurring at 532 nm, the S_1 state will be populated. Excited state absorption initiated by linear absorption and 2PA will give nearly identical results for loss as a function of input energy [91]. Thus, there are evidently a number of processes that could be contributing to the nonlinear absorptive properties of these compounds. For example, a styryl-substituted BODIPY in literature [83], has reportedly shown strong RSA behaviour consistent with sequential absorption from its longer lived S_1 excited state [83].

The z-scan plots for BODIPYs **(3)** and **(8–10)** in solution are shown in **Fig. 53**. The z-scan plots show a typical nonlinear absorption behaviour, with reverse saturable absorption (RSA) profiles. **Eqs. 1–4** were used to determine the nonlinear absorption coefficient (β) for each sample, and the results are summarised in **Table 12**. The experimental β values for BODIPYs **(3)**, **(8)**, **(9)** and **(10)**

in DMF solution were found to be 3.63×10^{-9}, 1.40×10^{-9}, 1.35×10^{-9}, and 1.62×10^{-9} $m \cdot W^{-1}$ respectively. This suggests that BODIPY **(3)** (substituted with 3-thiophene) showed a better β value compared to BODIPYs **(8), (9)** and **(10)**, which are substituted with 2-thiophene. The magnitude of the β values for BODIPYs **(3)** and **(8–10)** lie within the range of values previously reported for other organic compounds [74].

BODIPYs **(3)** and **(8–10)** were embedded in PBC as thin films and their β values measured. Z-scan plots for BODIPYs **(3)** and **(8–10)** embedded in PBC are shown in **Fig. 54**. Once again, BODIPY **(3)** had a better β value compared to BODIPYs **(8)**, **(9)** and **(10)**. The β values of BODIPY thin films **(3)–PBC**, **(8)–PBC**, **(9)–PBC** and **(10)–PBC** were found to be 21.35×10^{-9}, 21.10×10^{-9}, 13.00×10^{-9}, and 11.50×10^{-9} $m \cdot W^{-1}$, respectively. The β values of BODIPYs **(3)** and **(8–10)** were significantly improved when embedded in PBC as a thin film – a phenomenon that may primarily be attributed to aggregation of the molecules [140]. This was especially noticeable for BODIPY **(8)** embedded in PBC (**8–PBC**), which had a higher BODIPY concentration than the other films. **Fig. 55** and **Fig. 56** show open aperture z-scan profiles of BODIPYs **(3)** and **(8–10)** in solution and thin film at laser energies of E = 15 μJ and E = 25 μJ, respectively.

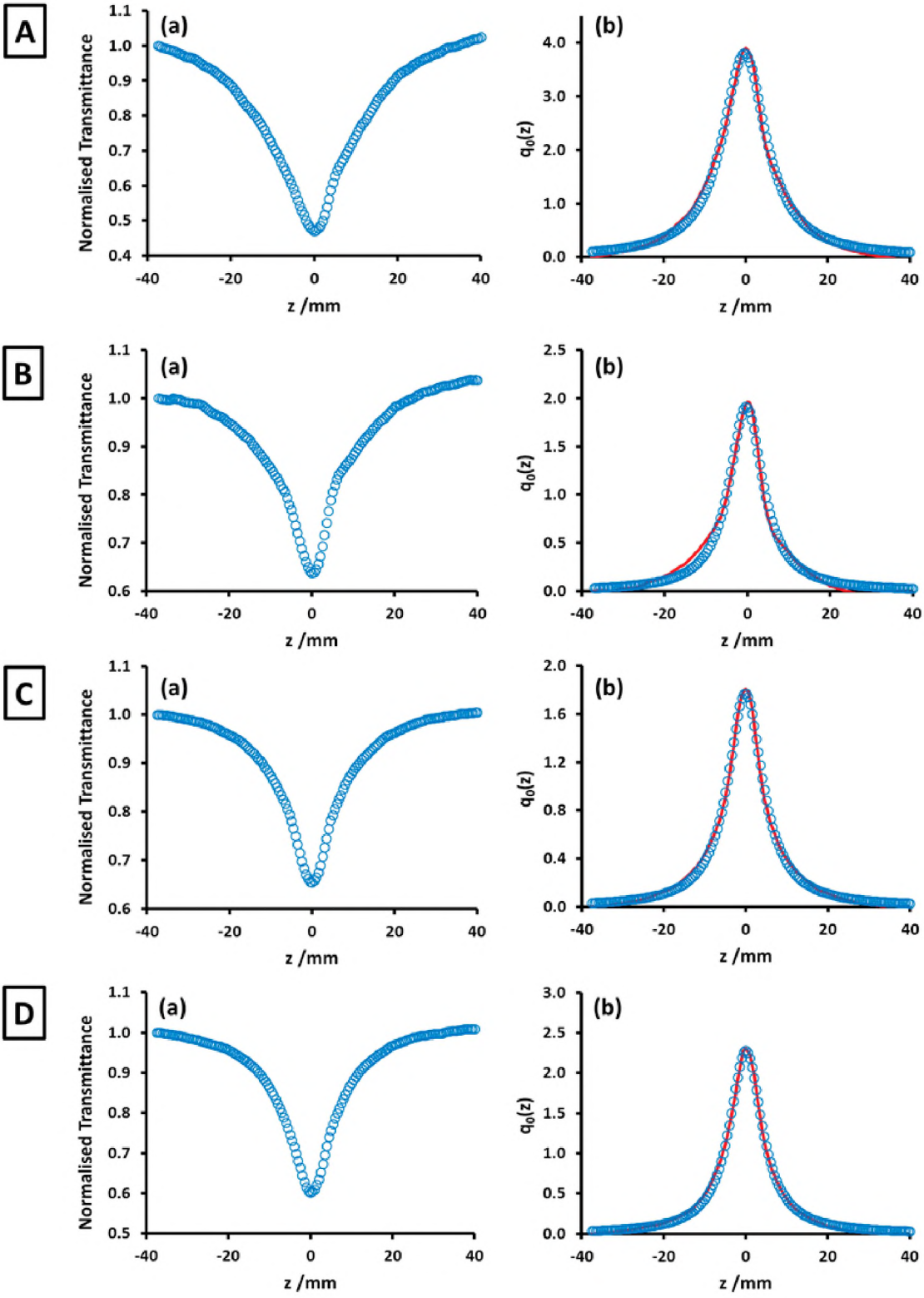

Figure 53. Z-scan (a) and nonlinear fit ($q_0(z)$) curves (b) for BODIPYs (A) **(3)**, (B) **(8)**, (C) **(9)** and (D) **(10)** in DMF solution.

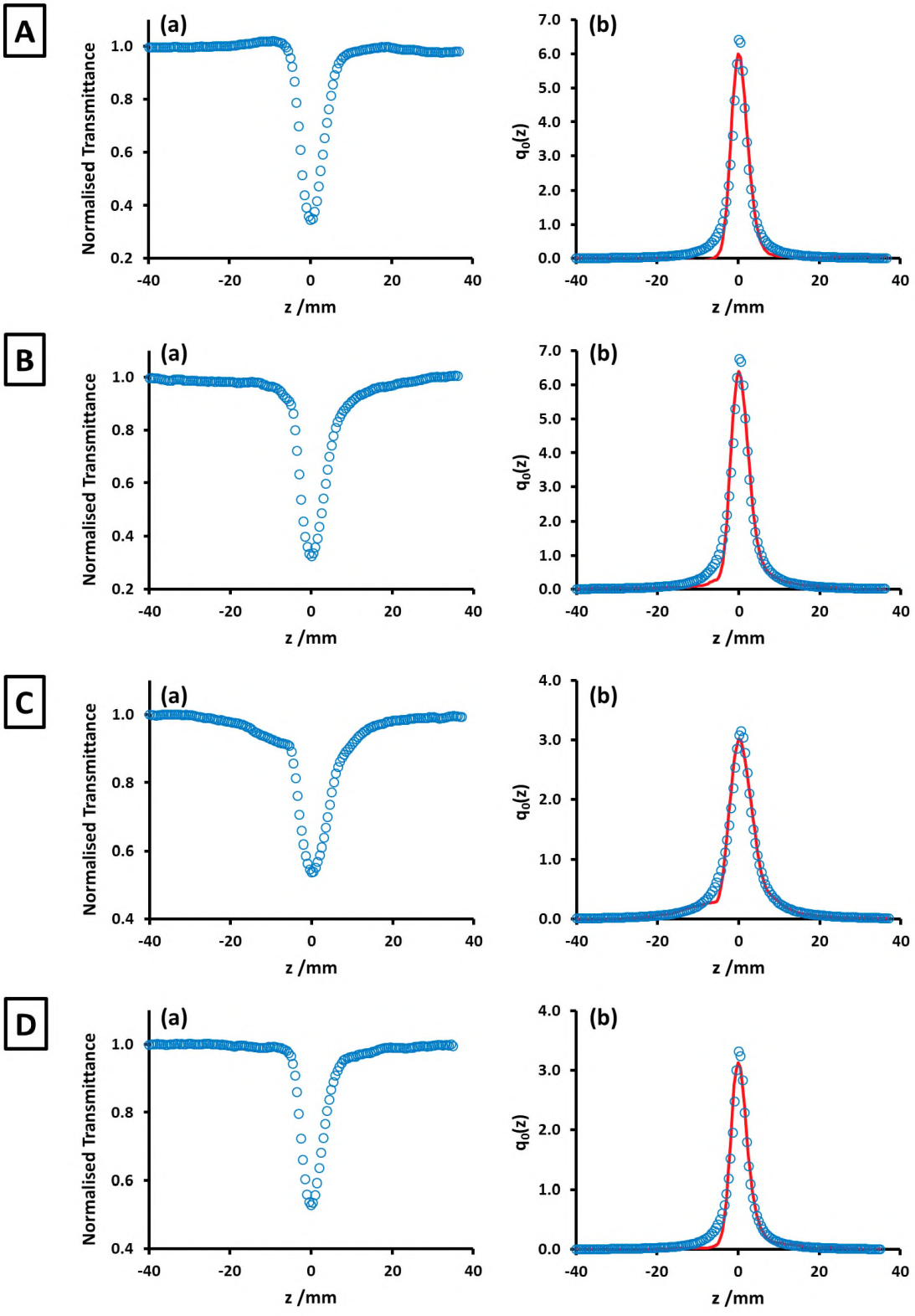

Figure 54. Z-scan (a) and nonlinear fit ($q_0(z)$) curves (b) for BODIPYs (A) **(3)**, (B) **(8)**, (C) **(9)** and (D) **(10)** when embedded in PBC thin films.

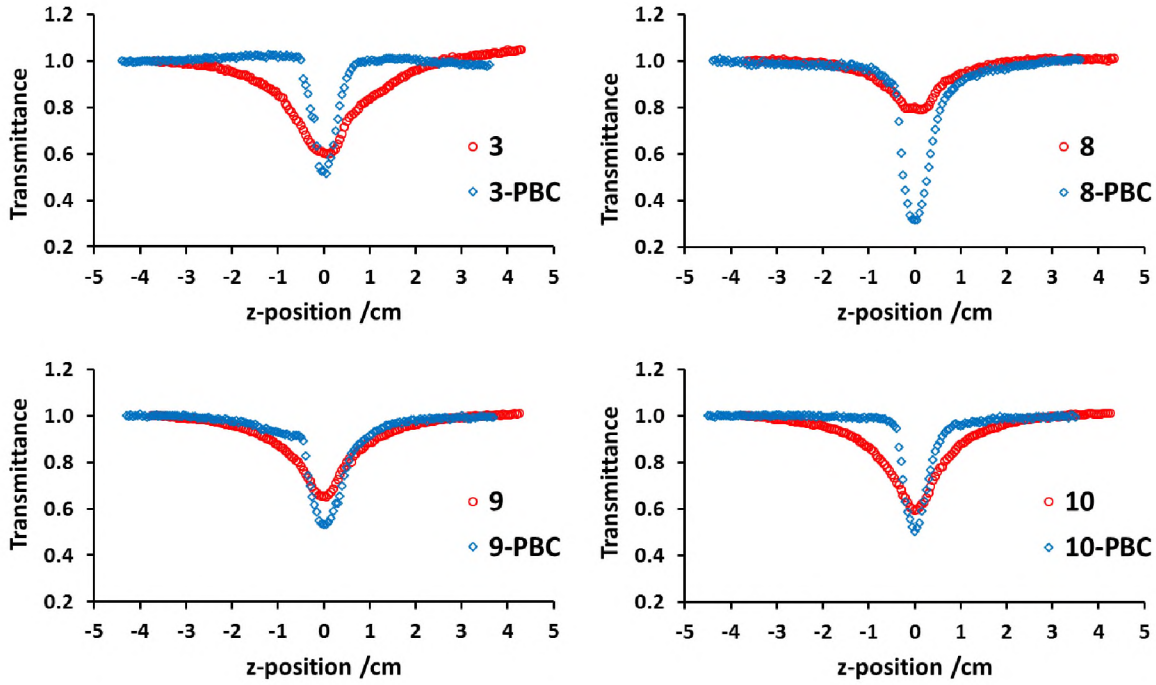

Figure 55. Open aperture z-scan profiles of BODIPYs **(3)**, **(8)**, **(9)**, and **(10)** in DMF (*red*) and when embedded in PBC thin films (*blue*) at E = 15 µJ.

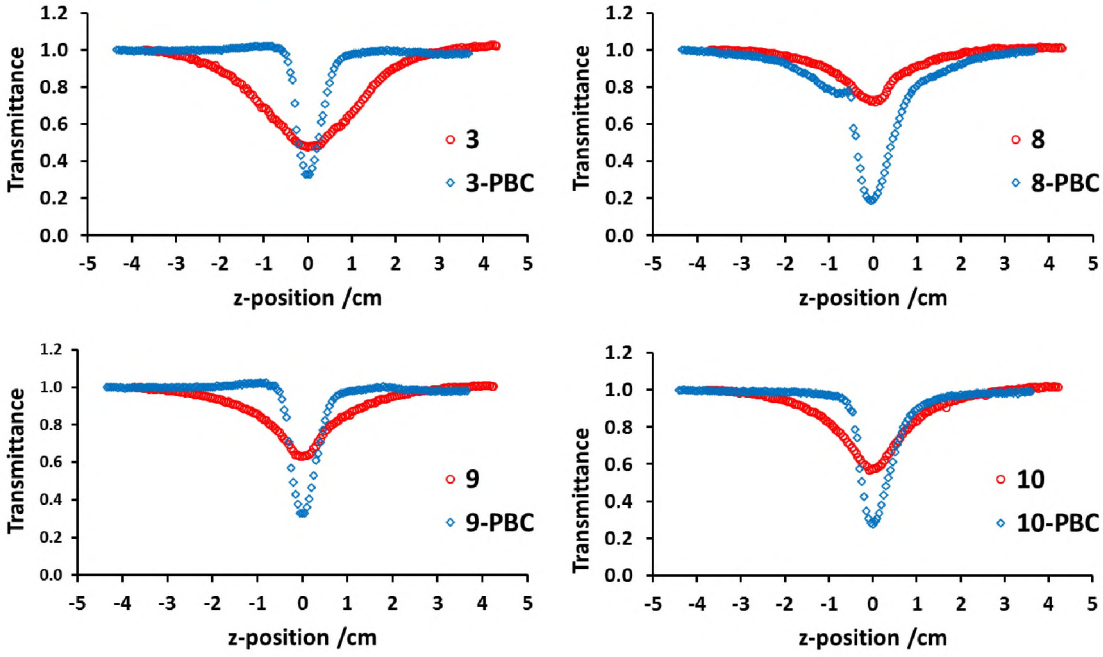

Figure 56. Open aperture z-scan profiles of BODIPYs **(3)**, **(8)**, **(9)**, and **(10)** in DMF (*red*) and when embedded in PBC thin films (*blue*) at E = 25 µJ.

4.3.2 Second-order hyperpolarizability (γ) and third-order nonlinear susceptibility ($Im[\chi^{(3)}]$)

The second-order hyperpolarizability, γ, measures the interaction of an incident photon with the permanent dipole moment of the BODIPY dyes at a molecular level, while the third-order nonlinear susceptibility, $Im[\chi^{(3)}]$, is a measure of the ultra-fast response of a nonlinear optical material. Both values are required to be sufficiently large; reported values for $Im[\chi^{(3)}]$ and γ are typically in the range of 10^{-9}–10^{-15} and 10^{-29}–10^{-34} respectively [96]. **Table 12** summarises the $Im[\chi^{(3)}]$ and γ values of BODIPYs **(3)**, **(8)**, **(9)**, and **(10)** in solution and as thin films. The concentrations of BODIPYs **(3)**, **(8)**, **(9)**, and **(10)** were determined to be in the order of 10^{-4} M. The thickness of the films was determined to be 21 µm for **(8)–PBC** and **(9)–PBC**, and 17 µm for **(3)–PBC** and **(10)–PBC** using SEM.

The $Im[\chi^{(3)}]$ values obtained for both solutions and thin films fall into the aforementioned range. The γ values of BODIPYs **(8)** and **(9)** in thin films (**8–PBC** and **9–PBC**) also fell within the literature range, while γ values of the 2,6-halogenated BODIPYs **(3)** and **(10)** in thin films (**3–PBC** and **10–PBC**) were even better. In general, the $Im[\chi^{(3)}]$ and γ values are much larger in thin films compared to the corresponding solution (**Table 12**). BODIPY **(3)** showed a higher $Im[\chi^{(3)}]$ value compared to BODIPYs **(8)**, **(9)** and **(10)**, both in solution and thin film. BODIPY **(8)**, which showed a particularly high β value in thin film (**8–PBC**), also had a high value for $Im[\chi^{(3)}]$, as the two quantities are directly proportional. As γ describes the nonlinear absorption *per mole* of the OL compound, it is useful when comparing efficiencies of different optical limiters. It is here that it can be seen that although BODIPY **(8)** shows comparatively high β and $Im[\chi^{(3)}]$ values when embedded in PBC, this is primarily due to the higher concentration of BODIPY dye in **(8)–PBC** compared to the other films.

Table 12. NLO parameters for 3,5-dithienylenevinylene BODIPYs **(3)**, **(8)**, **(9)**, and **(10)** in DMF and embedded in PBC thin films.

Complex	[a] [C]×10^{-5} M [b] Film-thickness (μm)	β (m/W) × 10^{-9}	$Im[\chi^{(3)}]$ (× 10^{-10} esu)	γ (esu)	I_{lim} (J·cm^2)	I_{out} % at 50% I_{in}
(3)	11.67	3.63	1.18	2.60 × 10^{-30}	0.50	65
(8)	9.73	1.40	0.46	1.20 × 10^{-30}	–	80
(9)	8.56	1.35	0.44	1.31 × 10^{-30}	–	78
(10)	18.10	1.62	0.53	7.58 × 10^{-31}	1.63	71
(3)–PBC	17	21.35	6.97	1.12 × 10^{-28}	1.18	40
(8)–PBC	21	21.10	6.89	7.79 × 10^{-29}	0.61	39
(9)–PBC	21	13.00	4.24	4.19 × 10^{-29}	0.40	25
(10)–PBC	17	11.50	3.76	2.46 × 10^{-28}	0.96	38

[a] Concentration in DMF solution [b] Average thickness of BODIPY-embedded PBC films

4.3.3 Optical limiting threshold (I_{lim})

The limiting threshold intensity or fluence, I_{lim}, is defined as the input fluence at which nonlinear transmittance is 50 % of the linear transmittance [75, 97]. The value of I_{lim} was determined using plots of input fluence vs. output fluence (**Fig. 57**), and transmittance vs. input fluence (**Fig. 58**).

The I_{lim} values of BODIPYs **(8)** and **(9)** in solution could not be estimated, as the transmittance did not drop below 50 % (**Fig. 58**). **Table 12** shows the I_{lim} values of BODIPYs **(3)** and **(10)** to be 0.50 and 1.63 J·cm^{-2} respectively, in solution. The I_{lim} values of BODIPYs **(3)**, **(8)**, **(9)**, and **(10)** in thin films were 1.18, 0.61, 0.40, and 0.96 J·cm^{-2} respectively. Hence, BODIPY **(3)** (in solution) and BODIPYs **(8)** and **(9)** (in thin films) fall below the damage threshold of 0.95 J·cm^{-2}.

A logarithmic plot of I_{out} versus I_{in} may also be used for a rough comparison of different optical limiting materials. **Fig. 59** shows the logarithmic plot of I_{out} versus I_{in} for BODIPYs **(3)**, **(8)**, **(9)**, and **(10)** in DMF and as films. **Table 12** records the I_{out} percentage at 50 % of I_{in}. In solution, the I_{out} percentage values suggest that the responses of BODIPYs **(8)** and **(9)** are very similar (80 and 78 % respectively), while BODIPY **(10)** is better (at 71 %) and BODIPY **(3)** performs the best (with 65 %). However, as a film, BODIPY **(9)** shows a significantly better response of 25 %, while BODIPYs **(3), (8)** and **(10)** have I_{out} percentage values of 39, 40, and 38 %, respectively.

Since the concentration was not held constant, one cannot fully conclude which of the four 3,5-dithienylenevinylene BODIPY dyes showed the best NLO properties. However, they all showed some degree of nonlinear optical behaviour and, due to the RSA profiles obtained, warrant further investigation for optical limiting.

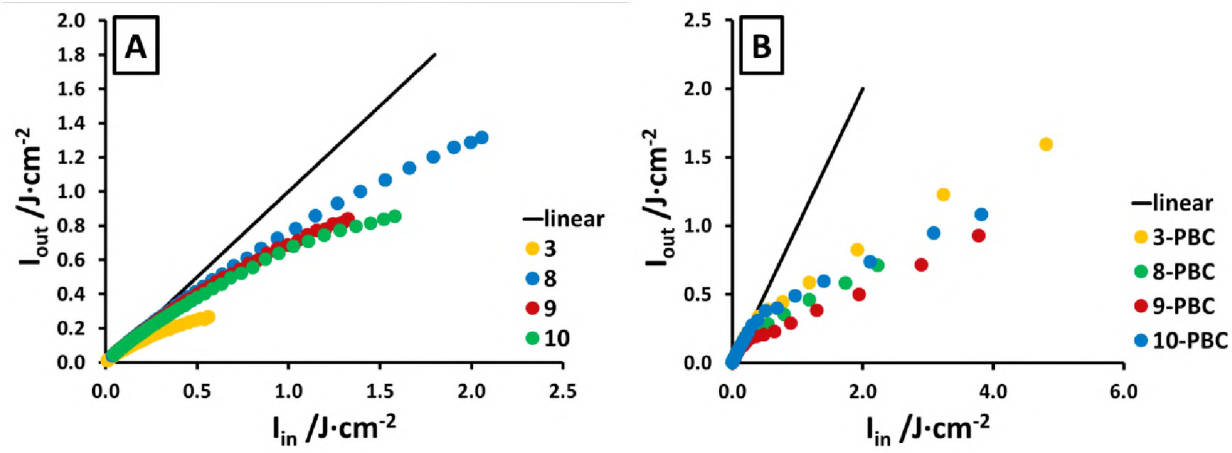

Figure 57. Plots of I_{out} vs I_{in} for BODIPYs **(3)**, **(8)**, **(9)**, and **(10)** (A) in DMF and (B) when embedded in PBC thin films. The solid black line represents linear transmittance.

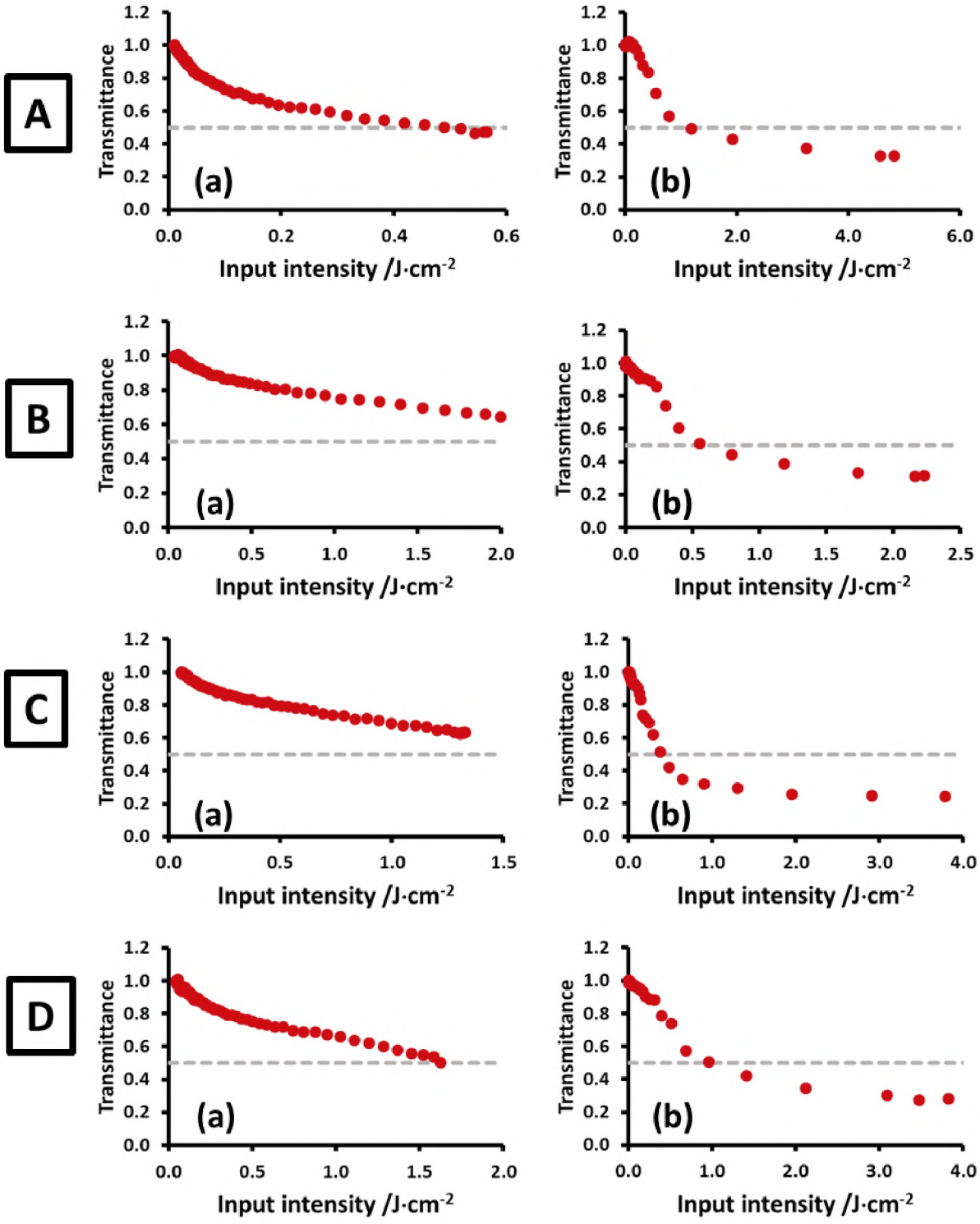

Figure 58. Normalised transmittance vs input fluence curves for BODIPYs (A) **(3)**, (B) **(8)**, (C) **(9)** and (D) **(10)** in DMF (a) and when embedded in PBC thin films (b). Grey dotted line indicates 50 % transmittance and is used to determine the I_{lim} value.

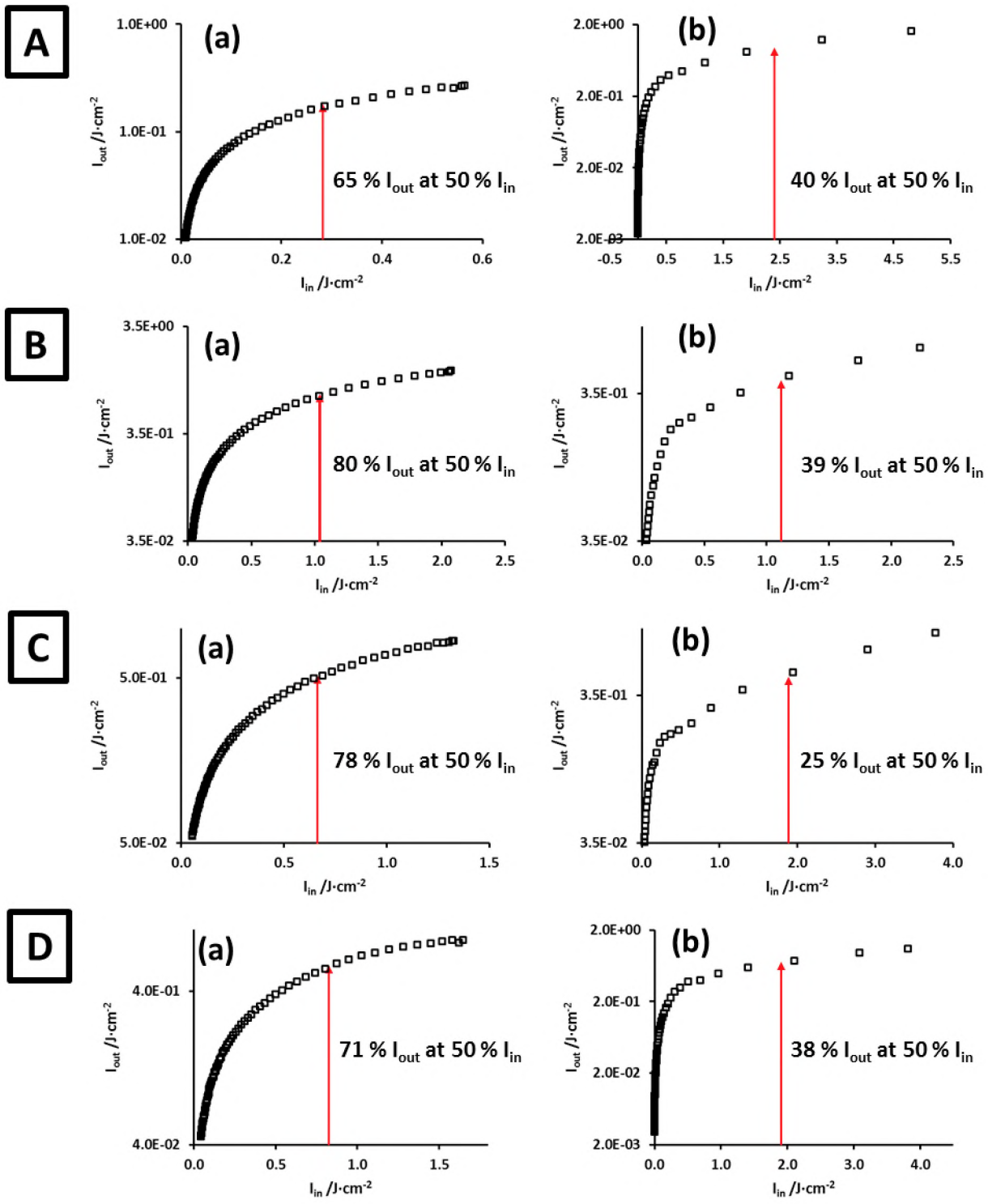

Figure 59. Logarithmic plot of I_{out} versus I_{in} for BODIPYs (A) **(3)**, (B) **(8)**, (C) **(9)** and (D) **(10)** in DMF (a) and when embedded in PBC thin films (b).

4.4 Concluding remarks

Substitution with thiophene groups at the 3,5-positions of the BODIPY core red-shifted the main spectral bands of BODIPYs **(3)**, **(8)**, **(9)**, and **(10)** to 650–670 nm. Hence, there is only limited absorption at 532 nm. All the compounds studied exhibited RSA behaviour, both in solution and when embedded in PBC thin films. As BODIPYs **(3)** and **(10)** possess halogen atoms at the 2,6-positions, which enhance ISC *via* the heavy atom effect, their OL activity may arise from either 2PA or sequential photon absorption in the singlet manifold. BODIPYs **(8)** and **(9)** also showed RSA behaviour, despite the fact they do not contain any heavy atoms, and are therefore unable to undergo ISC to the triplet state. Hence, any OL behaviour displayed by **(8)** and **(9)** is likely due to sequential photon absorption in the singlet manifold.

BODIPY **(3)** showed the best OL activity in solution, with an I_{lim} value of 0.50 J·cm^{-2}, which is lower than the threshold value of 0.95 J·cm^{-2}. The I_{lim} values of **(8)–PBC** and **(9)–PBC** were also below the threshold, at 0.61 and 0.40 J·cm^{-2}, respectively.

Chapter 5:

Molecular Modelling

5.1 Geometry optimisations and TD-DFT calculations

Molecular modelling may be used to investigate the spectral trends and structure-property relationships of a series of related BODIPY dyes. Gaussian09 software was used to perform geometry optimisations for a number of BODIPY dyes using the B3LYP functional with SDD basis sets. The SDD basis set, while not particularly suited to handling a specific range of atoms, offers reasonable approximations for all atoms, including the heavy bromine and iodine atoms used in this study. The B3LYP functional does not take charge transfer into account sufficiently and as there is likely to be significant charge transfer in the electronic excited states of the TBC complexes, the Coulomb-attenuating method — Becke 3-Parameter, Lee, Yang and Parr (CAM-B3LYP) was used for the TD-DFT calculations that are used to predict the electronic absorption properties of the compounds. The CAM-B3LYP functional was used as it includes a long-range correction of the exchange potential, which incorporates an increasing fraction of Hartree-Fock (HF) exchange as the interelectronic separation increases [141].

5.2 BODIPYs for PDT

This section addresses the structural modifications made to the BODIPY cores, **(1)** and **(5)**, and serves to explain why these changes influence their absorption properties, ultimately resulting in BODIPYs that are better suited for use in PDT-related applications.

Changing the *para*-substituent on the *meso*-phenyl of the BODIPY does not affect the HOMO–LUMO band gap, as evidenced by the similarities between **BDP**, **(1)** and **(5)** (**Table 13**). As the *meso*-phenyl group is oriented perpendicular to the plane of the BODIPY core, due to the steric hindrance of the methyl groups at the 1- and 7-postions, there is poor conjugation with the BODIPY π-system and, as such, changes at the *para*-position on the *meso*-phenyl have little impact on the predicted MO energies. This observation is consistent with experimental data (**Table 13**).

While BODIPYs are not formally aromatic, as they do not obey Huckel's rule for aromaticity, they display properties similar to aromatic systems due to the rigidity of the indacene plane upon complexation with boron difluoride. Hence, the indacene plane can be compared to those of an aromatic $C_{12}H_{12}^{2-}$ cyclic perimeter corresponding to the inner ligand perimeter, which can be used for describing and rationalising the optical properties, according to the principles of Michl's perimeter model [142, 143]. The TD-DFT calculations predict that the lowest lying $S_0 \rightarrow S_1$ transition is almost entirely associated with the HOMO → LUMO one-electron transition (**Table 13**), as the C_{2V} symmetry acquired by BODIPY dyes upon complexation with a boron difluoride ligand results in the HOMO and LUMO being energetically well-separated from other MOs (**Fig. 60**). Thus, when considering the impact of structural changes, it is the HOMO and LUMO which should be considered, with the other MOs remaining largely uninvolved. A red-shift of the BODIPY main spectral band arises when structural alterations change the energies of the HOMO and LUMO in such a way that the HOMO–LUMO band gap is narrowed.

Two major modifications are made to the BODIPY core in this work. To increase singlet oxygen generating capacity, bromine atoms are added at the 2,6-positions, promoting ISC to the triplet state. Thereafter, vinyl/ styryl moieties are added at the 3,5-positions to red-shift the main spectral band of the BODIPY towards the biological window. Molecular modelling allows for better understanding of these phenomena. The calculated oscillator strengths and corresponding wavenumbers of BODIPY **(1)**, its 2,6-dibrominated analogue **(2)**, and its 3,5,7-di(4-methylthio)styryl substituted counterpart (**Fig. 61**) indicate the predicted changes of the spectral bands upon modification. The addition of bromine groups at the 2,6-positions results in a red-shift of ca. 30 nm. Although the addition of bromine atoms at these positions results in the stabilisation of the whole stack of MOs (**Fig. 60**), halogens are able to donate a pair of electrons in resonance forms, which leads to some degree of destabilisation. At the 2,6-positions, there are significant MO coefficients in the HOMO, but only small MO coefficients in the LUMO (**Fig. 61 A**). Hence, when bromine atoms are added at the 2,6-positions, they cause a net destabilisation of the HOMO relative to the LUMO, resulting in the narrowing of the HOMO–LUMO band gap, which leads to the red-shifting of the observed spectral bands of the BODIPY. The same is observed for BODIPY **(5)** and its 2,6-dibrominated analogue **(6)** (**Fig. 62**).

In can be seen in **Fig. 61** and **Fig. 62** that the MO coefficients at the 3,5-positions are unevenly distributed in the HOMO and LUMO of the brominated compounds. A larger MO coefficient in the HOMO suggests that any structural alterations at this position should affect the HOMO to a greater extent than the LUMO, and can thus result in a change in magnitude of the HOMO–LUMO band gap. The inclusion of vinyl/ styryl moieties at the 3,5-positions results in a further red-shift between 115–150 nm, depending on the functional groups present on the styryl moiety, which is consistent with experimental data (**Table 13**). The HOMO–LUMO one-electron transitions remain the dominant transition for the main absorption band of the styryl-substituted BODIPY dyes but other one-electron transitions are calculated for HOMO−1 → LUMO, and HOMO → LUMO+1 (**Table 13**). These transitions are primarily associated with the styryl substituents and result in absorption bands observed over the 300–450 nm region.

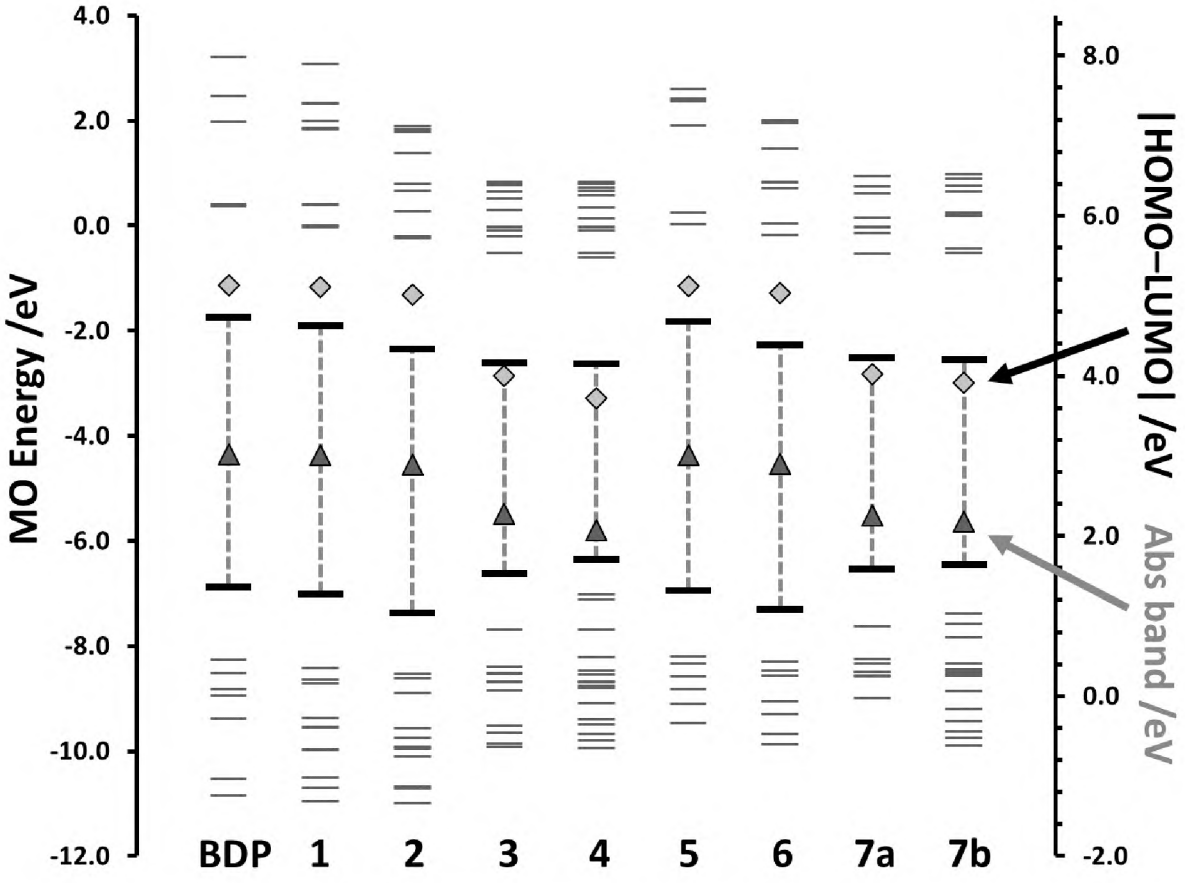

Figure 60. MO energies in TD-DFT calculations in vacuo at the CAM-B3LYP/SDD level of theory for the B3LYP/SDD optimised geometries of 1,3,5,7-tetramethyl-*meso*-phenyl-BODIPY (**BDP**), and BODIPYs **(1–7)**. The HOMO and LUMO for each compound are highlighted with thick black lines. The calculated HOMO–LUMO gaps and energies for the main BODIPY absorption bands are plotted against a secondary axis.

Table 13. Calculated and observed electronic excitation wavelengths of 1,3,5,7-tetramethyl-*meso*-phenyl-BODIPY **(BDP)** and BODIPYs **(1–7)**, and their calculated oscillator strengths and wavefunctions.

BODIPY	# [a]	E (eV) [b]	λ_{exp} [c]	λ_{calc} [d]	ν_{calc} [e]	f [f]	Wavefunction [g]
BDP	1	3.02	498[h] [32]	411	24.3	0.55	H → L (96 %); ...
(1)	1	3.01	503	412	24.3	0.55	H → L (97 %); ...
(2)	1	2.89	530	429	23.3	0.62	H → L (96 %); ...
(3)	1	2.27	650	546	18.3	1.00	H → L (97 %); ...
	2	3.46	–	358	27.9	0.69	H-1 → L (94 %); ...
	4	4.27	–	290	34.5	1.11	H → L+1 (90 %); ...
(4)	1	2.07	681	600	16.7	1.12	H → L (95 %); ...
	2	2.77	–	448	22.3	0.49	H-1 → L (70 %); H-4 → L (13 %); ...
	3	3.10	–	400	25.0	0.80	H-2 → L (75 %); H-1 → L (16 %); ...
	6	3.93	–	316	31.7	0.63	H → L+1 (44 %); H-4 → L (17 %); ...
	7	3.98	–	311	32.1	0.81	H → L+1 (30 %); H-4 → L (20 %); ...
(5)	1	3.01	502	411	24.3	0.54	H → L (96 %); ...
(6)	1	2.90	528	428	23.4	0.62	H → L (97 %); ...
(7a)	1	2.25	641	550	18.2	0.94	H → L (97 %); ...
	2	3.46	–	358	27.9	0.79	H-1 → L (94 %); ...
	5	4.14	–	300	33.4	1.04	H → L+1 (81 %); ...
(7b)	1	2.18	647	568	17.6	1.05	H → L (97 %); ...
	3	3.37	–	368	27.2	0.73	H-2 → L (85 %); ...
	7	4.12	–	301	33.3	1.08	H → L+1 (60 %); H-7 → L (11 %); ...

[a] – Excited state number assigned in increasing energy in the TD-DFT calculations. Only states located below 35000 cm^{-1} resulting from allowed electronic transitions with an oscillator strength greater than 0.5 are consistently included. [b] – Calculated band energies in eV. [c] – Experimental wavelengths in nm, recorded in DMSO. [d] – Calculated wavelengths in nm. [e] – Calculated band energy (10^3 cm^{-1}). [f] – Calculated oscillator strengths. [g] – Wavefunctions of MOs involved in the transition, and their respective contributions, based on eigenvectors predicted by TD-DFT. H and L refer to the HOMO and LUMO respectively. [h] – Literature value, recorded in MeOH.

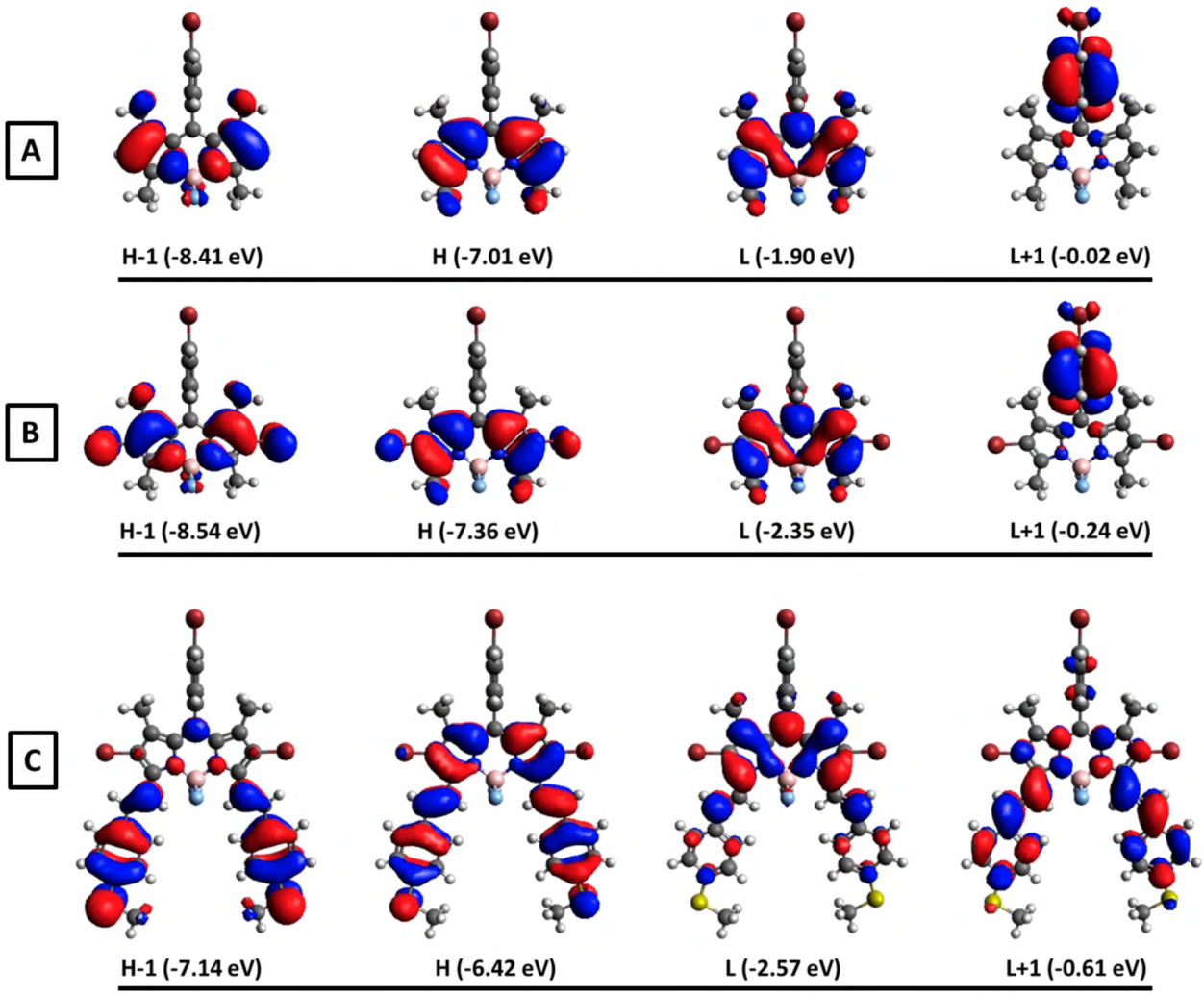

Figure 61. Nodal patterns (at an isosurface value of 0.02 a.u.) and MO energies of BODIPYs (A) **(1)**, (B) **(2)**, and (C) their di(4-methylthio)styryl analogue in the TD-DFT calculations carried out using the CAM-B3LYP functionals with SDD basis sets.

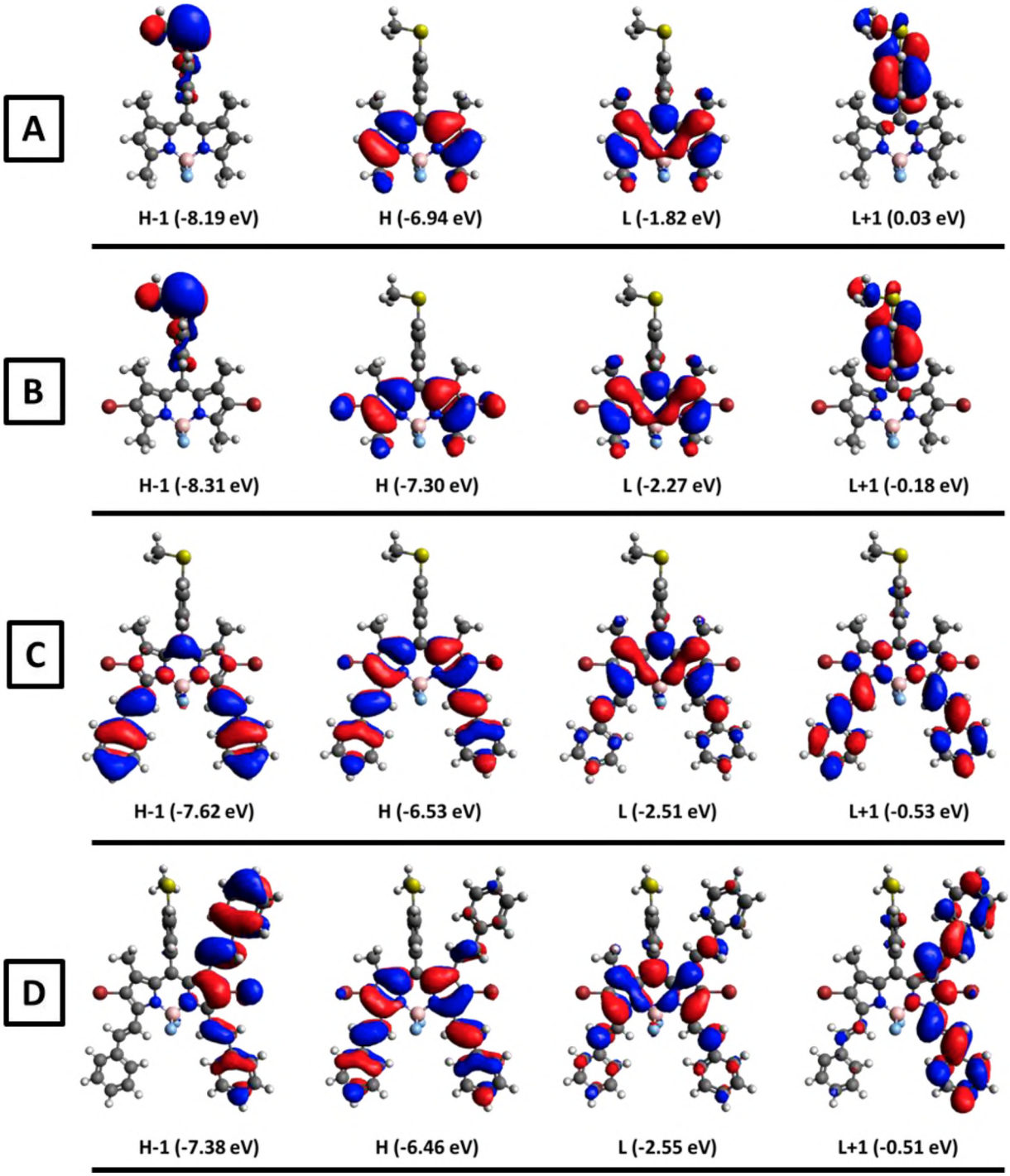

Figure 62. Nodal patterns (at an isosurface value of 0.02 a.u.) and MO energies of BODIPYs (A) **(5)**, (B) **(6)**, (C) **(7a)**, and (D) **(7b)** in the TD-DFT calculations carried out using the CAM-B3LYP functionals with SDD basis sets.

5.2.1 BODIPY (4)

As the mono-, di- and tetra-styryl analogues of BODIPY **(4)** were not isolated in this work, molecular modelling was employed to investigate the structure-property relationships of this series, to better understand the spectroscopic properties of BODIPY **(4)** and to determine if any of the other derivatives might be a better candidate for use in PDT applications.

Geometry optimisations were performed at a B3LYP level of theory, with SDD basis sets. The precursor, the 2,6-dibrominated BODIPY **(2)**, showed a highly planar structure (**Fig. 63 A**). The sequential addition of (4-methylthio)styryl groups at the 3,5-positions, gave the mono- and di-styryl derivatives of BODIPY **(4)**. In both cases, the BODIPYs retained their planar structure to a large extent (**Fig. 63 B** and **Fig. 63 C**). However, the introduction of (4-methylthio)styryl groups at the 1- (**Fig. 63 D**) and 1,7-positions (**Fig. 63 E**), requires that the styryl moieties twist out of plane. This twisting results in poorer conjugation of the 1,7-styryl groups with the BODIPY core [144]. Hence, although these styryl groups extend the π-system, which typically results in a red-shift of the main absorption bands, the magnitude of the red-shift is significantly smaller than that observed for the mono- and di-styryl derivatives (**Fig. 64**).

Although the (4-methylthio)styryl groups at the 1, 7-positions cannot be accommodated in a planar fashion, the bromine at the *para*-position of the *meso*-phenyl is a single-atom group, and the *meso*-phenyl retains its original orientation, perpendicular to the indacene plane (**Fig. 63 E**).

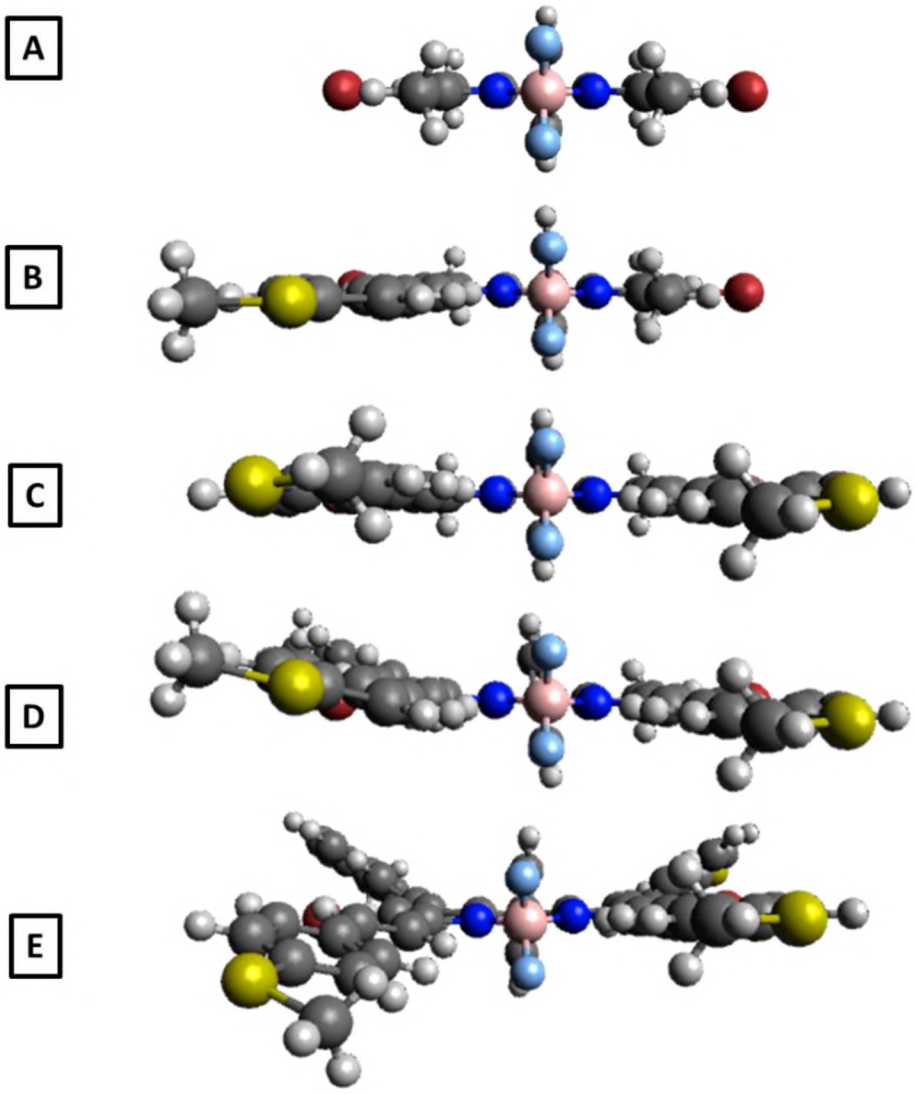

Figure 63. View along the boron–*meso*-carbon axis of (A) the 2,6-dibrominated BODIPY **(2)**, and its (B) mono-, (C) di-, (D) tri-**(4)**, and (E) tetra-styryl derivatives. The indacene plane is perpendicular to the page.

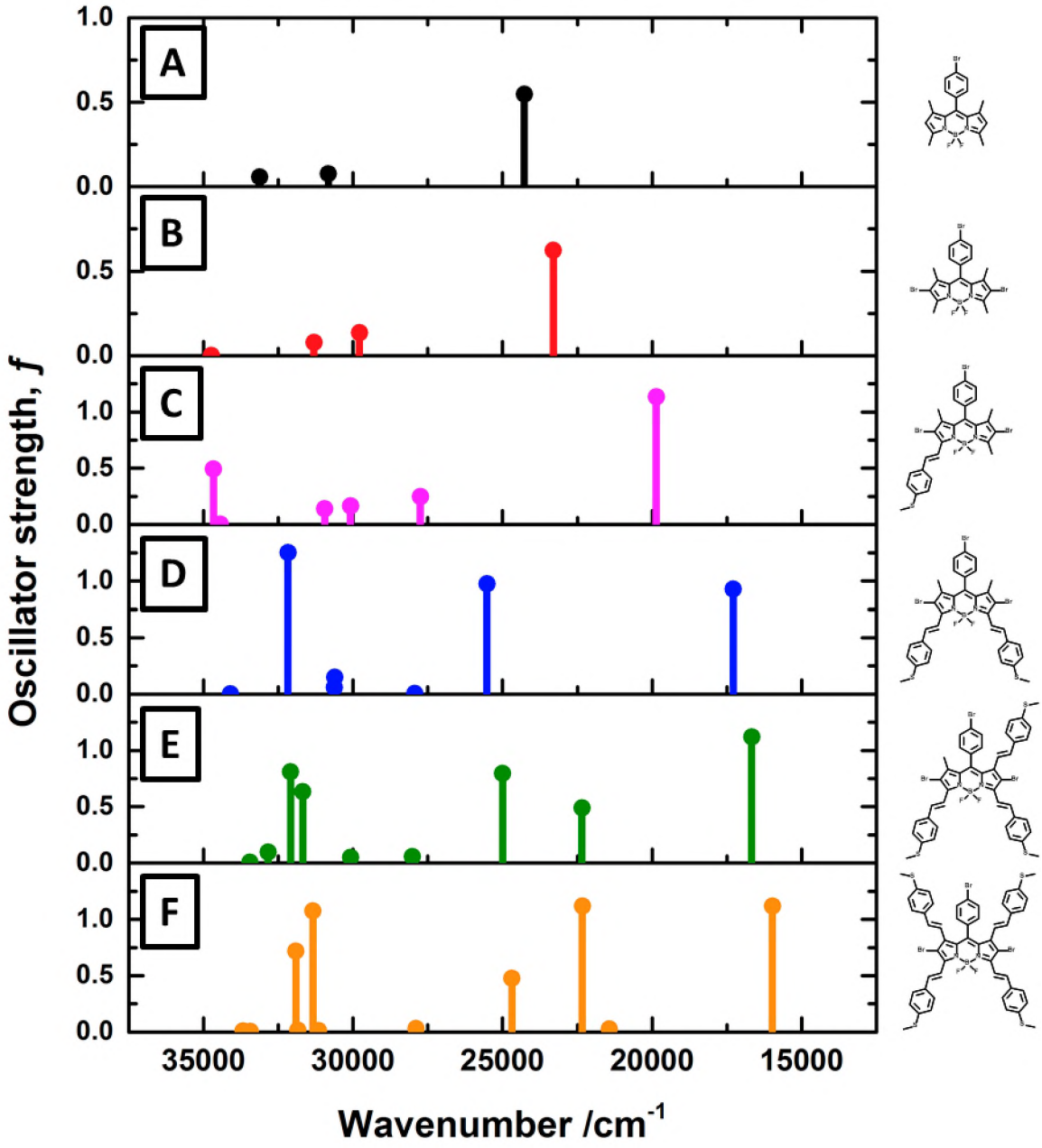

Figure 64. TD-DFT calculated oscillator strengths for (A) BODIPY core **(1)**, (B) its 2,6-dibrominated analogue **(2)** and its (C) mono-, (D) di-, (C) tri-**(4)**, and (D) tetra-(4-methylthio)styryl derivatives. Only oscillator strengths corresponding to wavenumbers in the range of 15000–35000 cm^{-1} were considered.

5.2.2 BODIPYs (7a) and (7b)

Both the di-**(7a)** and tri-styryl **(7b)** BODIPY derivatives were isolated and characterised in this work. However, their absorption maxima occurred at very similar wavelengths, which was not expected due to the large red-shift observed for the di-styryl derivative. Hence, molecular modelling was employed to investigate the structure-property relationships of this series, to better understand the spectroscopic properties of **(7a)** and **(7b)**.

The TD-DFT calculated oscillator strengths of this series are shown in **Fig. 65**. Bromination of BODIPY **(5)** to yield the 2,6-dibrominated derivative, BODIPY **(6)**, results in a red-shift of ca. 925 cm^{-1} (**Table 13**, **Fig 63 B**). Introduction of a single styryl group at the 3-position of the BODIPY core results in a large red-shift of ca. 2800 cm^{-1}, while the sequential addition of another styryl group at the 5-position (giving the 3,5-distyryl derivative, BODIPY **(7a)** (**Fig. 65 D**)) results in a further red-shift, with a magnitude of ca. 2300 cm^{-1}.

However, when a third styryl group is introduced at the 1-position, giving **(7b)**, the magnitude of the red-shift is much smaller, at only 578 cm^{-1} (**Fig. 65 E**). Interestingly, when a fourth styryl group is introduced at the 7-position (giving the 1,3,5,7-tetrastyryl derivative), the main absorption band is blue-shifted by ca. 5000 cm^{-1} with respect to the tri-styryl derivative (**Fig. 65 E**). These observations may be explained by observing the geometry-optimised structures for this series of BODIPYs.

The precursor, the 2,6-dibrominated BODIPY **(5)**, showed a highly planar structure (**Fig. 66 A**). The sequential addition of styryl groups at the 3,5-positions, gave the mono- and di-styryl derivatives of BODIPY **(7)**. In both cases, the BODIPYs retained their planar structure to a large extent (**Fig. 66 B** and **Fig. 66 C**), as there is very little steric hindrance at these positions. However, the introduction of additional styryl groups at the 1-position (**Fig. 66 D**) requires the twisting of the styryl moiety. This twisting results in poorer conjugation of the 1-styryl group with the BODIPY core. Hence, although this styryl group extends the π-system of the BODIPY, the magnitude of the red-shift is significantly smaller than that observed for the mono- and di-styryl derivatives.

The addition of a fourth styryl group (giving the 1,3,5,7-styryl derivative (**Fig. 65 F**)) requires twisting of the styryl groups in order to achieve incorporation, in a similar manner as to that

observed for BODIPY **(4)**. While the *para*-position of the *meso*-phenyl does not typically affect the spectroscopic properties of the BODIPY, as the ring is perpendicular to the indacene plane, when the substituent at the *para*-position is relatively bulky, it compromises the ability to substitute with styryl groups at the 1,7-positions. In this case, there is increased steric hindrance due to the bulky (4-methylthio) group present on the *meso*-phenyl. In **Fig. 66 E**, it is evident that the *meso*-phenyl of the tetra-styryl derivative is no longer perpendicular to the BODIPY core. The *meso*-phenyl and the styryl groups are twisted in order to sterically accommodate each other, which compromises the conjugation of the styryl moieties. Hence, the tetra-styryl derivative is blue-shifted compared to the tri-styryl **(7b)** derivative. Additionally, a blue-shift may arise from destabilisation of the LUMO relative to the HOMO, due to asymmetric MO coefficients present at the 1,7-positions of the BODIPY core (**Fig. 62**). As there are larger MO coefficients present on these positions in the LUMO, substitution at these positions will affect the LUMO to a greater extent than the HOMO.

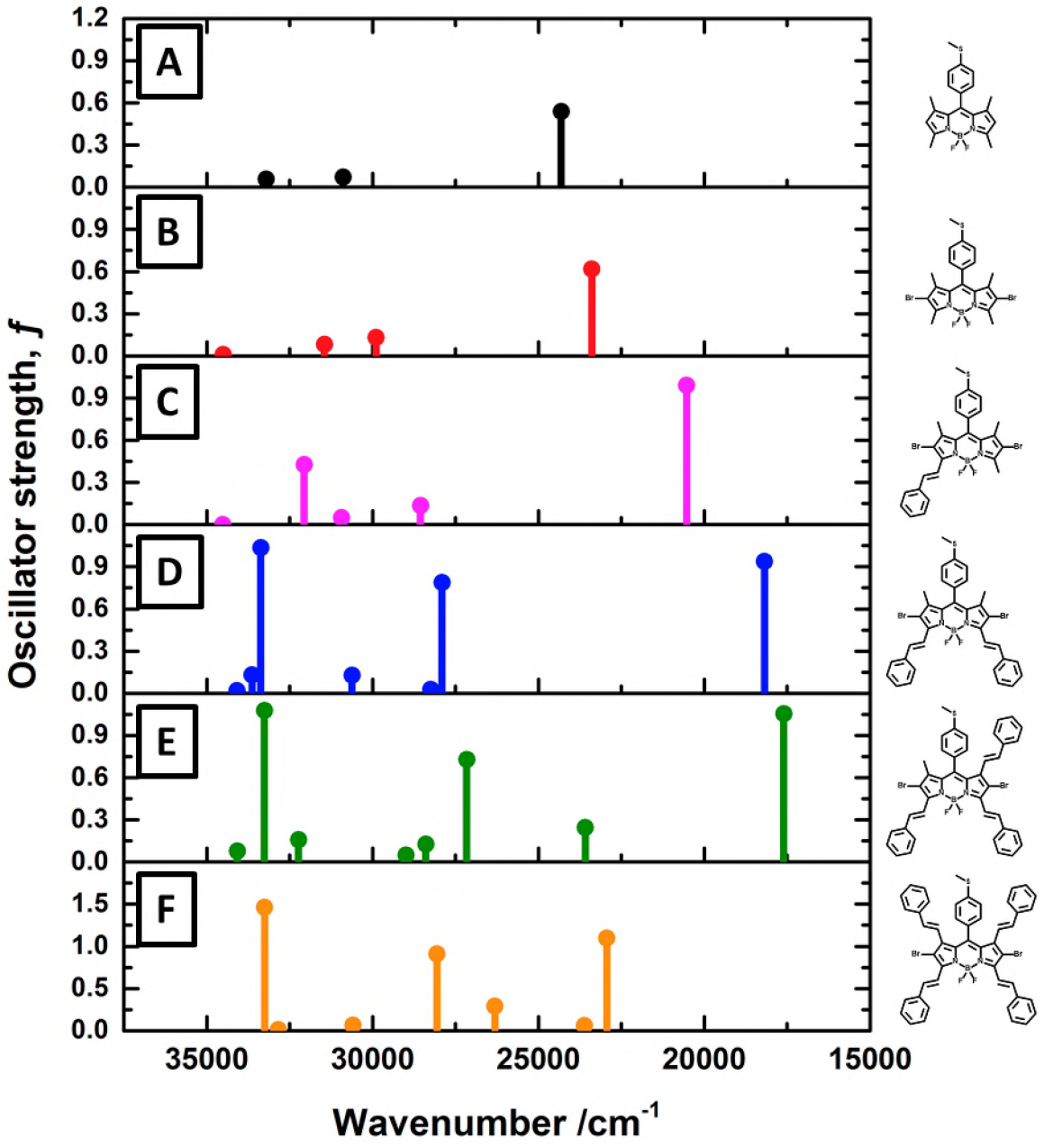

Figure 65. TD-DFT calculated oscillator strengths for (A) BODIPY core **(5)**, (B) its 2,6-dibrominated analogue **(6)** and its (C) mono-, (D) di-**(7a)**, (C) tri-**(7b)**, and (D) tetra-styryl derivatives. Only oscillator strengths corresponding to wavenumbers in the range of 15000–35000 cm^{-1} were considered.

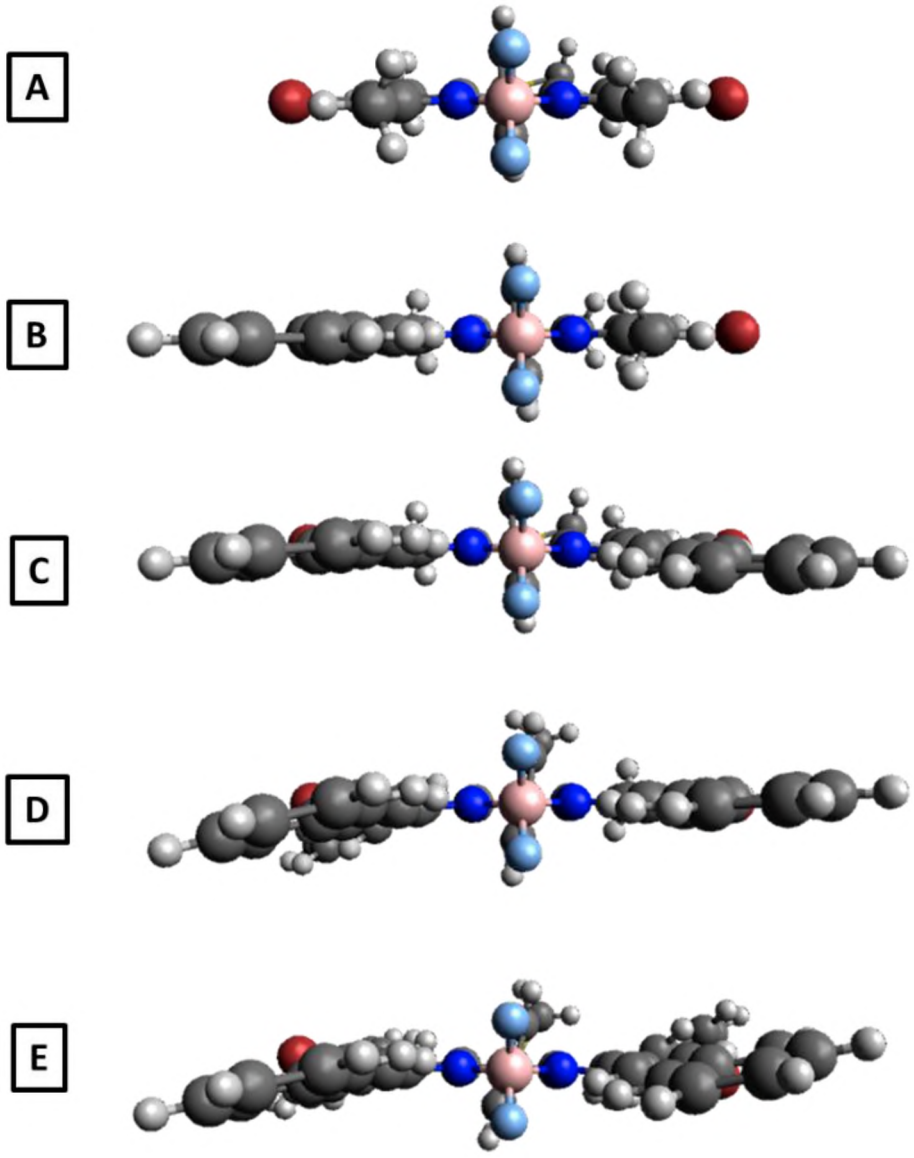

Figure 66. View along the boron–*meso*-carbon axis of (A) the 2,6-dibrominated BODIPY **(6)**, and its (B) mono-, (C) di-**(7a)**, (D) tri-**(7b)**, and (E) tetra-styryl derivatives, showing the loss of planarity upon inclusion of styryl moieties at the 1, 7-positions of the BODIPY core. The indacene plane is perpendicular to the page.

5.3 3,5-Dithienylenevinylene BODIPYs **(3)** and **(8–10)** for optical limiting

This section investigates the properties of a series of 3,5-dithienylenevinylene BODIPYs: **(3)**, **(8)**, **(9)** and **(10)**, whose nonlinear optical properties were investigated in Chapter 4. TD-DFT calculations were performed on B3LYP geometry optimised structures using CAM-B3LYP and SDD basis sets. A MO energy diagram (**Fig. 67**) was then plotted to compare the characteristics of these compounds. 1,3,5,7-tetramethyl-*meso*-phenyl-BODIPY (**BDP**) was also modelled to allow for more meaningful comparison.

The TD-DFT calculations predict that the lowest lying $S_0 \rightarrow S_1$ transition is almost entirely associated with the HOMO → LUMO one-electron transition (**Table 14**). The C_{2V} symmetry possessed by BODIPYs as a result of complexation with a boron difluoride ligand results in the HOMO and LUMO being well-separated from other MOs.

BODIPYs **(8)** and **(9)** are very similar, differing only in that BODIPY **(8)** has no *para*-substituent present on the *meso*-phenyl, whereas BODIPY **(9)** has a –COOMe group attached at this point. The *meso*-phenyl group is oriented perpendicular to the plane of the BODIPY core, due to the steric hindrance of the methyl groups at the 1- and 7-postions. This results in poor conjugation with the BODIPY π-system and as such, changes at the *para*-position on the *meso*-phenyl have little impact on the predicted MO energies. This observation is consistent with experimental data (**Table 14**).

BODIPY **(3)** is brominated at the 2,6-positions, while BODIPY **(10)** has iodine atoms substituted at these positions. Halogens are electronegative and thus act as electron withdrawing groups (EWG). However, they have the ability to donate a pair of electrons in resonance forms. At the 2,6-positions, there are significant MO coefficients in the HOMO, but only small MO coefficients in the LUMO (**Fig. 68**). Thus, any structural modifications at these positions will affect the energy of the HOMO more than that of the LUMO. When halogens are added at the 2,6-positions, they cause a net destabilisation of the HOMO relative to the LUMO, resulting in the narrowing of the HOMO–LUMO band gap, which leads to the red-shifting of the observed spectral bands of the BODIPY.

Although there are no nodal planes at the 3,5-positions in either the HOMO or LUMO of the BODIPY dyes, the MO coefficients at these positions are larger in the HOMO than in the LUMO. This means that any substitutions at these positions will have a greater effect on the HOMO than the LUMO, resulting in a net change in the HOMO–LUMO band gap. Substitution with conjugated moieties at the 3,5-positions extends the π-system of the BODIPY core and has a destabilising effect. As the HOMO is more affected, it will experience greater destabilisation than the LUMO, resulting in the narrowing of the HOMO–LUMO band gap and hence red-shifting of the main spectral band.

It may be observed in **Fig. 67** that both the HOMO and LUMO of BODIPY **(3)** are stabilised with respect to those of BODIPYs **(8)**, **(9)**, and **(10)**. This is likely due to the fact that BODIPY **(3)** contains 3-thiophene substituents whereas BODIPYs **(8)**, **(9)** and **(10)** contain 2-thiophene substituents at the 3,5-positions. The stabilising effect must have had a greater effect on the HOMO than the LUMO, resulting in a net blue shift in comparison to BODIPYs **(8)**, **(9)** and **(10)**. Stabilisation of the HOMO means that the complex is more stable to oxidative attack.

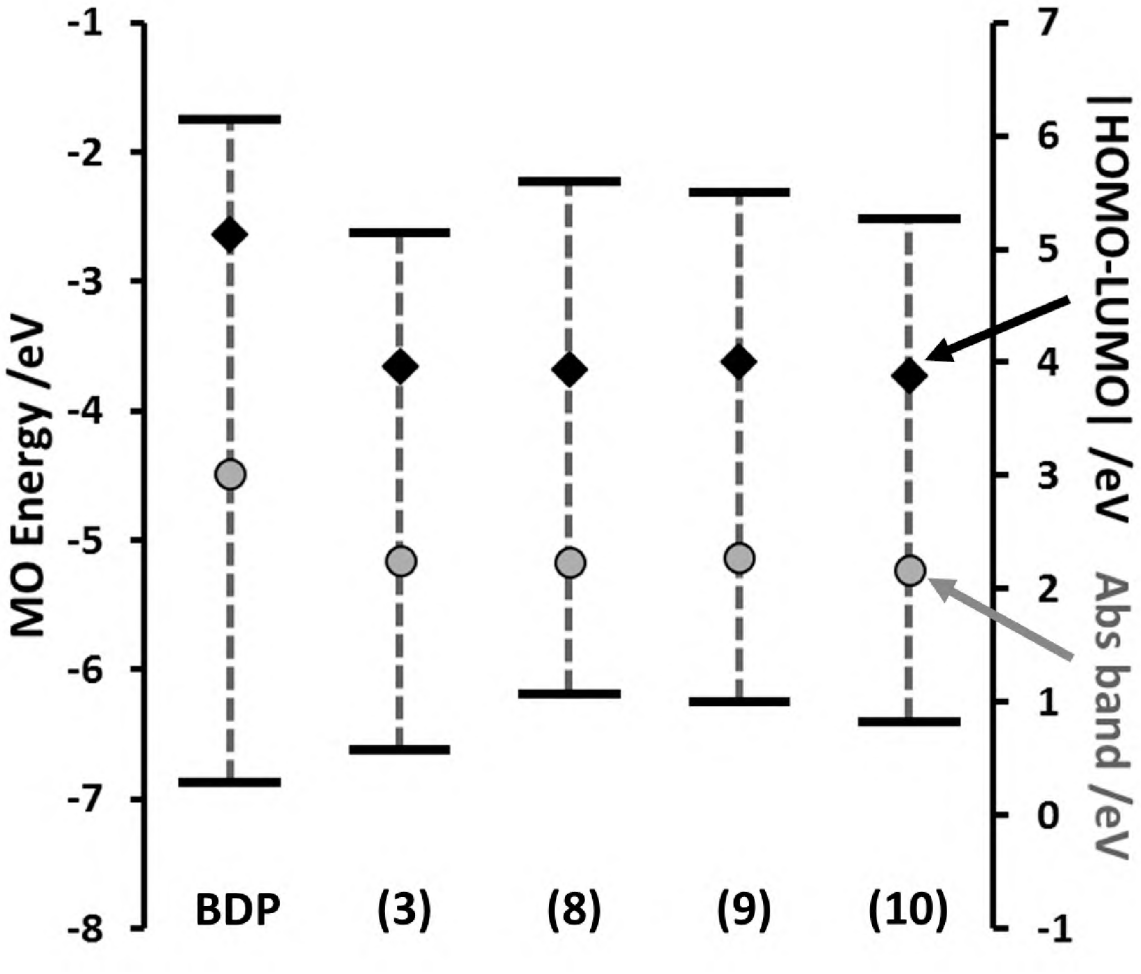

Figure 67. MO energies in TD-DFT calculations in vacuo at the CAM-B3LYP/SDD level of theory for the B3LYP/SDD optimised geometries of 1,3,5,7-tetramethyl-*meso*-phenyl-BODIPY (**BDP**), and BODIPYs **(3)**, **(8)**, **(9)**, and **(10)**. The HOMO and LUMO for each compound are highlighted with thick black lines. The calculated HOMO–LUMO gaps and energies for the main BODIPY absorption bands are plotted against a secondary axis.

Table 14. Calculated and observed electronic excitation wavelengths of 1,3,5,7-tetramethyl-*meso*-phenyl-BODIPY **(BDP)** and BODIPYs **(3)**, **(8)**, **(9)**, and **(10)**, and their calculated oscillator strengths and wavefunctions.

BODIPY	# [a]	E (eV) [b]	λ_{calc} [c]	λ_{exp} [d]	f [e]	Wavefunction [f]
BDP	1	3.02	411	498[g] [32]	0.55	H → L (96 %); ...
(3)	1	2.27	546	650	1.00	H → L (97 %); ...
	2	3.46	358	–	0.69	H-1 → L (94 %); ...
	7	4.27	290	–	1.11	H → L+1 (90 %); ...
(8)	1	2.24	554	652	1.02	H → L (97 %); ...
	2	3.45	360	–	0.64	H-1 → L (94 %); ...
	4	3.79	327	–	1.06	H → L+1 (91 %); ...
(9)	1	2.23	557	656	1.02	H → L (97 %); ...
	2	3.42	362	–	0.71	H-1 → L (94 %); ...
	4	3.79	327	–	1.11	H → L+2 (91 %); ...
(10)	1	2.16	574	669	0.93	H → L (97 %); ...
	2	3.26	380	–	0.74	H-1 → L (95 %); ...
	5	3.84	323	–	1.01	H → L+1 (91 %); ...

[a] – Excited state number assigned in increasing energy in the TD-DFT calculations. Only states resulting from allowed electronic transitions with oscillator strength greater than 0.5 are consistently included. [b] – Calculated band energies in eV. [c] – Calculated wavelengths in nm. [d] – Experimental wavelengths in nm, recorded in DMF. [e] – Calculated oscillator strengths. [f] – Wavefunctions of MOs involved in the transition, and their respective contributions, based on eigenvectors predicted by TD-DFT. H and L refer to the HOMO and LUMO respectively. [g] – Literature value, recorded in MeOH.

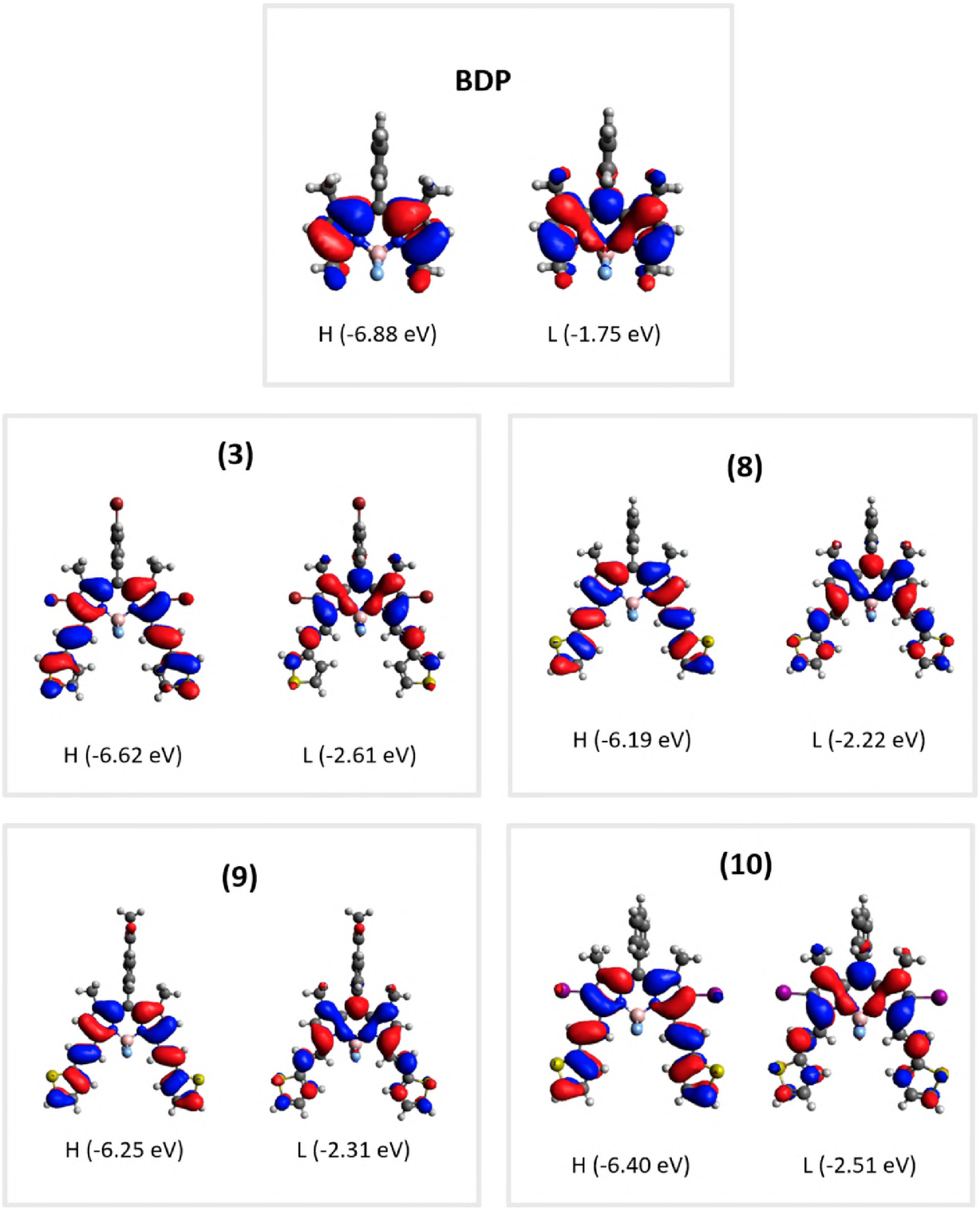

Figure 68. Nodal patterns (at an isosurface value of 0.02 a.u.) and MO energies of the HOMO and LUMO of 1,3,5,7-tetramethyl-*meso*-phenyl-BODIPY (**BDP**) and BODIPYs **(3)**, **(8)**, **(9)**, and **(10)**, obtained by TD-DFT calculations using the CAM-B3LYP functional with SDD basis sets.

5.4 Concluding remarks

The TD-DFT calculations are a useful tool for establishing the structure-property relationships of a series of related BODIPY dyes, in order to better understand their spectroscopic properties. The properties of the modelled dyes closely followed the trends observed for the synthesised dyes. As the same trends may be observed for the calculated values, and the corresponding experimental electronic absorption (**Table 13** and **Table 14**), it is evident that the spectral shifts may be rationalised based on calculated HOMO and LUMO values. Visualisation of the optimised geometries, and of the nodal patterns, of these BODIPYs offered possible explanations for the spectral phenomena observed.

Molecular modelling helps to provide an enhanced understanding of the trends that are observed experimentally, allowing for rational design of BODIPY dyes for use in applications such as PDT and NLO.

Chapter 6:

Conclusions, Limitations and Future Work

6.1 Conclusions

Two BODIPY dyes, **(1)** and **(5)**, were synthesised and fully characterised. BODIPY **(1)**, which has a bromine atom at the 4-position of the *meso*-phenyl, was synthesised using the classic "one-pot-three-step" acid catalysed condensation reaction, while the novel (4-methylthio) *meso*-phenyl BODIPY **(5)** was synthesised *via* the water-method preparation of the corresponding novel aryldipyrromethane **(5a)**. The spectroscopic properties of **(1)** and **(5)** were very similar, confirming that substitution at the *para*-position of the *meso*-phenyl does not have a large effect on the spectral properties of a BODIPY dye. This is due to the perpendicular orientation of the *meso*-phenyl, resulting in poor conjugation of the *meso*-phenyl with the BODIPY π-system. BODIPYs **(1)** and **(5)** were synthesised to serve as the core for a series of increasingly complex BODIPY dyes. BODIPYs **(1)** and **(5)** both had negligible singlet oxygen quantum yields.

In order to produce BODIPY dyes capable of generating singlet oxygen, BODIPYs **(1)** and **(5)** were brominated at the 2,6-positions, yielding BODIPYs **(2)** and **(6)** respectively. The attachment of bromine atoms to the BODIPY cores resulted in a red shift of ca. 30 nm with respect to the parent dyes. BODIPYs **(2)** and **(6)** displayed large singlet oxygen quantum yields that equalled that of the standard, Rose Bengal, and showed remarkable photostability, suggesting that they might be useful standards for Φ_Δ measurements. They may also be of use in singlet oxygen applications where a red-shifted photosensitiser is not required.

In order to red-shift the main spectral bands of the BODIPY dyes, BODIPYs **(2)** and **(6)** were modified by substitution at the 3,5-positions, *via* a modified version of the Knoevenagel condensation reaction. BODIPY **(2)** was reacted with 3-thiophenecarboxaldehyde to form **(3)** and with 4-(methylthio)benzaldehyde to yield **(4)**. BODIPYs **(3)** and **(4)** were red-shifted to the therapeutic window and showed moderate fluorescence and singlet oxygen quantum yields. BODIPY **(6)** was reacted with benzaldehyde to form BODIPYs **(7a)** and **(7b)**. BODIPYs **(7a)** and **(7b)** were red-shifted to the edge of the therapeutic window but showed poor singlet oxygen generation capability.

The nonlinear optical properties of BODIPY **(3)**, together with a number of other 3,5-dithienylenevinylene BODIPYs, **(8)**, **(9)** and **(10)**, was also investigated. All the 3,5-

dithienylenevinylene BODIPY dyes showed some optical limiting response at 532 nm in solution but better results were obtained when the dyes were embedded in PBC as thin films.

Molecular modelling was used to investigate the spectral trends and structure-property relationships of the BODIPY dyes intended for use in PDT and NLO, and helped to explain why the main absorbance band of the synthesised tri-styryl BODIPY dye **(7b)** was not significantly red-shifted with respect to its di-styryl analogue **(7a)**.

6.2 Limitations

- Water solubility is an important requirement for the application of photosensitisers in PDT. While it is possible to conjugate the BODIPY photosensitisers to drug carriers in order to achieve water solubility, another approach could be to introduce water-solubilising groups to the BODIPY dyes.
- Using tri- and tetra-styryl substitution as a method for red-shifting the main spectral bands of BODIPY dyes is limited due to the increased steric effects. Hence, it would be preferable to focus on di-styryl derivatives for PDT applications, with a focus on inclusion of moieties, such as fused-ring groups, that will maximise the red-shift of the main spectral band.

6.3 Future Work

- Conjugation of BODIPYs **(3)** and **(4)** to gold nanoparticles could be used to render the BODIPYs water soluble, and could increase the singlet oxygen quantum yields of these compounds *via* the external heavy atom effect.
- The inclusion of iodine atoms at the 2,6-positions, instead of bromine, could improve the singlet oxygen production of the BODIPY dyes.
- BODIPY **(6)** could be conjugated to water-soluble gold nanoparticles, *via* the (4-methylthio) group present on the *meso*-phenyl, for use in antimicrobial PDT (APDT). BODIPY **(6)** is a good candidate for application in APDT due to its high singlet oxygen quantum yield. Additionally, APDT does not require photosensitisers that are red-shifted to within the therapeutic window.

References

1. Treibs, A.; Kreuzer, F. H. Difluorboryl–komplexe von di– und tripyrrylmethenen. *Justus Liebigs Ann. Chem.* **1968**, *718*, 208–223.
2. Lu, H.; Mack, J.; Yang, Y.; Shen, Z. Structural modification strategies for the rational design of red/NIR region BODIPYs. *Chem. Soc. Rev.* **2014**, *43*, 4778–4823.
3. Schmitt, A.; Hinkeldey, B.; Wild, M.; Jung, G. Synthesis of the core compound of the BODIPY dye class: 4,4'-difluoro-4-bora-(3a,4a)-diaza-*s*-indacene. *J Fluoresc.* **2009**, *19*, 755–758.
4. Ulrich, G.; Ziessel, R.; Harriman, A. The chemistry of fluorescent Bodipy dyes: versatility unsurpassed. *Angew. Chem. Int. Ed*. **2008**, *47*, 1184 – 1201.
5. Monsma, F. J.; Barton, C.; Kang, H. C.; Brassard, D. L.; Haugland, R. P.; Sibley, D. R. Characterization of novel fluorescent ligands with high affinity for D1 and D2 dopaminergic receptors. *J. Neurochem.* **1989**, *52*, 1641–1644.
6. Shah, M.; Thangaraj, K.; Soong, M. -L.; Wolford, L. T.; Boyer, J. H.; Politzer, I. R.; Pavlopoulos, T. G. Pyrromethene–BF_2 complexes as laser dyes: 1. *Heteroatom Chem*. **1990**, *1*, 389–399.
7. Dost, Z.; Atilgan, S.; Akkaya, E. U. Distyryl–boradiazaindacenes: facile synthesis of novel near IR emitting fluorophores. *Tetrahedron* **2006**, *62*, 8484–8488.
8. Kamkaew, A.; Lim, S. H.; Lee, H. B.; Kiew, L. V.; Chung, L. Y.; Burgess, K. BODIPY dyes in photodynamic therapy. *Chem. Soc. Rev.* **2013**, *42*, 77–88.
9. Patrice, T.; Moan, J.; Peng, Q. An outline of the history of PDT. In *Photodynamic therapy*, 1st ed.; Royal Society of Chemistry, 2003, pp 1–18.
10. Dolmans, D.; Fukumura, D.; Jain, R. Photodynamic therapy for cancer. *Nat. Rev. Cancer* **2003**, *3*, 380–387.
11. Huang, Z. A review of progress in clinical photodynamic therapy. *Technol. Cancer Res. Treat.* **2005**, *4*, 283–293.
12. Hopper, C. Photodynamic therapy: a clinical reality in the treatment of cancer. *Lancet Oncol*. **2000**, 1, 212–219.

13. DeRosa, M.; Crutchley, R. Photosensitized singlet oxygen and its applications. *Coord. Chem. Rev.* **2002**, *233*, 351–371.
14. Bonnett, R. Photosensitizers of the porphyrin and phthalocyanine series for photodynamic therapy. *Chem. Soc. Rev.* **1995**, *24*, 19–33.
15. Moan, J.; Berg, K. The photodegradation of porphyrins in cells can be used to estimate the lifetime of singlet oxygen. *Photochem. Photobiol.* **1991**, *53*, 543–553.
16. Plaetzer, K.; Krammer, B.; Berlanda, J.; Berr, F.; Kiesslich, T. Photophysics and photochemistry of photodynamic therapy: fundamental aspects. *Lasers Med Sci*. **2009**, *24*, 259–268.
17. Bonnett, R. *Chemical aspects of photodynamic therapy*, 1st ed.; Gordon and Breach Science Publishers: Amsterdam, 2000.
18. Sharman, W.; Allen, C.; van Lier, J. Photodynamic therapeutics: basic principles and clinical applications. *Drug Discov. Today* **1999**, *4*, 507–517.
19. Ormond, A.; Freeman, H. Dye sensitizers for photodynamic therapy. *Materials* **2013**, *6*, 817–840.
20. Ethirijan, M.; Chen, Y.; Joshi, P.; Pandley, R. The role of porphyrin chemistry in tumor imaging and photodynamic therapy. *Chem. Soc. Rev*. **2011**, *40*, 340–362.
21. Wilkinson, F.; Helman, P.; Ross, A. Quantum yields for the photosensitized formation of the lowest electronically excited singlet state of molecular oxygen in solution. *J. Phys. Chem. Ref. Data* **1993**, *22*, 113–262.
22. Henderson, B.; Dougherty, T. How does photodynamic therapy work? *Photochem. Photobiol*. **1992**, *55*, 145–157.
23. Waris, G.; Ahsan, H. Reactive oxygen species: role in the development of cancer and various chronic conditions. *J. Carcinog*. **2006**, *5* (14).
24. Usui, Y. Determination of quantum yield of singlet oxygen formation by photosensitization. *Chem. Letters* **1973**, *2*, 743–744.
25. Kimel, S.; Tromberg, B.; Roberts, W.; Berns, M. Singlet oxygen generation of porphyrins, chlorins, and phthalocyanines. *Photochem. Photobiol.* **1989**, *50*, 175–183.

26. Aveline, B.; Hasan, T.; Redmond, R. W. Photophysical and photosensitizing properties of benzoporphyrin derivative monoacid ring A (BPD–MA). *Photochem. Photobiol.* **1994**, *59*, 328–335.

27. Redmond, R.; Gamlin, J. A compilation of singlet oxygen yields from biologically relevant molecules. *Photochem. Photobiol.* **1999**, *70*, 391–475.

28. Spikes, J.; Bommer, J. Photosensitizing properties of mono–L–aspartyl chlorin e6 (NPe6): a candidate sensitizer for the photodynamic therapy of tumors. *J. Photochem. Photobiol., B* **1993**, *17*, 135–143.

29. He, J.; Larkin, H. E.; Li, Y. S.; Rihter, D.; Zaidi, S. I.; Rodgers, M. A.; Mukhar, H.; Kenney, M. E.; Oleinick, N. L. The synthesis, photophysical and photobiological properties and *in vitro* structure–activity relationships of a set of silicon phthalocyanine PDT photosensitizers. *Photochem. Photobiol.* **1997**, *65*, 581–586.

30. Fernandez, J.; Bilgin, M.; Grossweiner, L. Singlet oxygen generation by photodynamic agents. *J. Photochem. Photobiol., B* **1997**, *37*, 131–140.

31. Ni, Y.; Wu, J. Far-red and near infrared BODIPY dyes: synthesis and applications for fluorescent pH probes and bio-imaging. *Org. Biomol. Chem*. **2014**, *12*, 3774–3791.

32. Loudet, A.; Burgess, K. BODIPY dyes and their derivatives: syntheses and spectroscopic properties. *Chem. Rev*. **2007**, *107*, 4891–4932.

33. Benniston, A. C.; Copley, G. Lighting the way ahead with boron dipyrromethene (Bodipy) dyes, *Phys. Chem. Chem. Phys.* **2009**, *11*, 4124–4131.

34. Yogo, T.; Urano, Y.; Ishitsuka, Y.; Maniwa, F.; Nagano, T. Highly efficient and photostable photosensitizer based on BODIPY chromophore. *J. Am. Chem. Soc.* **2005**, *127*, 12162–12163.

35. Awuah, S. G.; You, Y. Boron dipyrromethene (BODIPY)–based photosensitizers for photodynamic therapy. *RSC Adv*. **2012**, *2*, 11169–11183.

36. Wang, Y. W.; Descalzo, A. B.; Shen, Z.; You, X. Z.; Rarack, K. Dihydronaphthalene-fused boron-dipyrromethene (BODIPY) dyes: insight into the electronic and conformational tuning modes of BODIPY fluorophores. *Chem. Eur. J.* **2010**, *16*, 2887–2903.

37. Michl, J. Magnetic circular dichroism of cyclic π–electron systems. 1. Algebraic solution of the perimeter model for the *A* and *B* terms of high–symmetry systems with a $(4N + 2)^{-}$ electron [*n*]annulene perimeter. *J. Am. Chem. Soc*. **1978**, *100*, 6801–6811.

38. Michl, J. Magnetic circular dichroism of cyclic π–electron systems. 2. Algebraic solution of the perimeter model for the *B* terms of systems with a $(4N + 2)^{-}$ electron [*n*]annulene perimeter. *J. Am. Chem. Soc.* **1978**, *100*, 6812–6818.

39. Kobayashi, N.; Muranaka, A.; Mack, J. Michl's Perimeter Model in MCD Spectroscopy. In *Circular Dichroism and Magnetic Circular Dichroism Spectroscopy for Organic Chemists*. Royal Society of Chemistry: London, 2011; pp 172–191.

40. Gai, L.; Mack, J.; Lu, H.; Yamada, H.; Kuzuhara, D.; Lai, G.; Li, Z.; Shen, Z. New 2,6-distyryl-substituted BODIPY isomers: synthesis, photophysical properties, and theoretical calculations. *Chem. Eur. J.* **2014**, *20*, 1091–1102.

41. Tram, K.; Yan, H.; Jenkins, H. A.; Vassiliev, S.; Bruce, D. The synthesis and crystal structure of unsubstituted 4,4'-difluoro-4-bora-3a,4a-diaza-*s*-indacene (BODIPY). *Dyes Pigm.* **2009**, *82*, 392–395.

42. Qin, W.; Rohand, T.; Dehaen, W.; Clifford, J.; Driesen, K.; Beljonne, D.; Van Averbeke, B.; Van der Auweraer, M.; Boens, N. Boron dipyrromethene analogues with phenyl, styryl, and ethynlphenyl substituents: synthesis, photophysics, electrochemistry, and quantum–chemical calculations. *J. Phys. Chem. A.* **2007**, *111*, 8588–8597.

43. Zhang, M.; Hao, E.; Xu, Y.; Zhang, S.; Zhu, H.; Wang, Q.; Yu, C.; Jiao, L. One–pot efficient synthesis of pyrrolylBODIPY dyes from pyrrole and acyl chloride. *RSC Adv.* **2012**, *2*, 11215–11218.

44. Wagner, R. W.; Lindsey, J. S. Boron–dipyrromethene dyes for incorporation in synthetic multi–pigment light–harvesting arrays. *Pure Appl. Chem.* **1996**, *68*, 1373–1380.

45. Gibbs, J.; Robins, L. T.; Zhou, Z.; Bobadova-Parvanova, P.; Cottam, M.; McCandless, G. T.; Fronczek, F. R.; Vicente, M. G. H. Spectroscopic, computational modeling and cytotoxicity of a series of *meso*–phenyl and *meso*–thienyl–BODIPYs. *Bioorg. Med. Chem*. **2013**, *21*, 5770–5781.

46. Lu, H.; Zhang, S.; Liu, H.; Wang, Y.; Shen, Z.; Liu, C.; You, X. Experimentation and theoretic calculation of a BODIPY sensor based on photoinduced electron transfer for ions detection. *J. Phys. Chem. A.* **2009**, *113*, 14081–14086.

47. Matsumoto, T.; Urano, Y.; Shoda, T.; Kojima, H.; Nagano, T. A thiol-reactive fluorescence probe based on donor-excited photoinduced electron transfer: key role of *ortho* substitution. *Org. Lett.* **2007**, *9*, 3375–3377.

48. Ueno, T.; Urano, Y.; Kojima, H.; Nagano, T. Mechanism-based molecular design of highly selective fluorescence probes for nitrative stress. *J. Am. Chem. Soc*. **2006**, *128*, 10640–10641.

49. Rohand, T.; Dolusic, E.; Ngo, T.; Maes, W.; Dahaen, W. Efficient synthesis of aryldipyrromethanes in water and their application in the synthesis of corroles and dipyrromethenes. *ARKIVOC* **2007**, 307–324.

50. Cui, X.; Zhang, C.; Xu, K.; Zhao, J. Application of singlet energy transfer in triplet state formation: broadband visible light–absorbing triplet photosensitizers, molecular structure design, related photophysics and applications. *J. Mater. Chem. C*. **2015**, *3*, 8735–8759.

51. Gobeze, H.; Bandi, V.; D'Souza, F. Bis(subphthalocyanine)–azaBODIPY triad for ultrafast photochemical processes. *Phys. Chem. Chem. Phys.* **2014**, *16*, 18720–18728.

52. Lee, H.; Bae, D.; Park, J.; Song, H.; Han, W.; Jung, J. A selective fluoroionophore based on BODIPY–functionalized magnetic silica nanoparticles: removal of Pb^{2+} from human blood. *Angew. Chem.* **2009**, *121*, 1265–1269.

53. Nagai, A.; Yoshii, R.; Otsuka, T.; Kokado, K.; Chujo, Y. BODIPY–based chain transfer agent: reversibly thermoswitchable luminescent gold nanoparticle stabilized by BODIPY–terminated water–soluble polymer. *Langmuir* **2010**, *26*, 15644–15649.

54. Grazon, C.; Rieger, J.; Méallet–Renault, R.; Charleux, B.; Clavier, G. Ultrabright fluorescent polymeric nanoparticles made from a new family of BODIPY monomers. *Macromolecules* **2013**, *46*, 5167–5176.

55. Li, L.; Nguyen, B.; Burgess, K. Functionalization of the 4-4'-difluoro-4-bora-3a,4a-diaza-*s*-indacene (BODIPY) core. *Bioorg. Med. Chem. Lett.* **2008**, *18*, 3112–3116.

56. Lakshmi, V.; Ravikanth, M. Brominated boron dipyrrins: synthesis, structure, spectral and electrochemical properties. *Dalton Trans.* **2012**, *41*, 5903–5911.

57. Sabatini, R. P.; McCormick, T. M.; Lazarides, T.; Wilson, K. C.; Eisenberg, R.; McCamant, D. W. Intersystem crossing in halogenated Bodipy chromophores used for solar hydrogen production. *J. Phys. Chem. Lett.* **2011**, *2*, 223–227.

58. Jiao, L.; Pang, W.; Zhou, J.; Wei, Y.; Mu, X.; Bai, G.; Hao, E. Regioselective stepwise bromination of boron dipyrromethene (BODIPY) dyes. *J. Org. Chem.* **2011**, *76*, 9988–9996.

59. Wan, C. W.; Burghart, A.; Chen, J.; Bergström, F.; Johansson, L. B. A.; Wolford, M. F.; Kim, T. G.; Topp, M. R.; Hochstrasser, R. M.; Burgess, K. Anthracene – BODIPY cassettes: syntheses and energy transfer. *Chem. Eur. J.* **2003**, *9*, 4430 – 4431.

60. Morgan, L. R.; Boyer, J. H. Boron difluoride compounds useful in photodynamic therapy and production of laser light, US Patent 5446157, 19 February, 1993.

61. Hoogendoorn, S.; Blom, A.; Willems, L.; van der Marel, G.; Overkleeft, H. Synthesis of pH-activatable red fluorescent BODIPY dyes with distinct functionalities. *Org. Lett.* **2011**, *13*, 5656–5659.

62. Rurack, K.; Kollmannsberger, M.; Daub, J. A highly efficient sensor molecule emitting in the near infrared (NIR): 3,5-distyryl-8-(*p*-dimethylaminophenyl)-difluoroboradiaza-*s*-indacene. *New J. Chem.* **2001**, *25*, 289–292.

63. Chen, J.; Burghart, A.; Derecskei–Kovacs, A.; Burgess, K. 4,4'-Difluoro-4-bora-3a,4a-diaza-*s*-indacene (BODIPY) dyes modified for extended conjugation and restricted bond rotations. *J. Org. Chem.* **2000**, *65*, 2900–2906.

64. Leen, V. Synthesis and application of reactive BODIPY dyes. PhD. Dissertation, Katholieke Univeriteit, Leuven, 2010.

65. Majumdar, P.; Yuan, X.; Li, S.; Guennic, B.; Ma, J.; Zhang, C.; Jacquemin, D.; Zhao, J. Cyclometalated Ir(II) complexes with styryl-BODIPY ligands showing near IR absorption/ emission: preparation, study of photophysical properties and application as photodynamic/ luminescence imaging materials. *J. Mater. Chem. B* **2014**, *2*, 2838–2854.

66. Son, H.; Lee, J. H.; Kim, Y.; Lee, I. S.; Han, S.; Liu, X.; Jaworski, J.; Jung, J.H. A BODIPY–functionalized bimetallic probe for sensitive and selective color–fluorometric chemosensing of Hg^{2+}. *Analyst* **2012**, *137*, 3914–3916.

67. Son, H.; Lee, H.Y.; Lim, J. M.; Kang, D.; Han, W. S.; Lee, S. S.; Jung, J. H. A highly sensitive and selective turn–on fluorogenic and chromogenic sensor based on BODIPY–functionalized magnetic nanoparticles for detecting lead in living cells. *Chem. Eur. J.* **2010**, *16*, 11549–11553.

68. He, G. S.; Liu, S. H. Optical limiting, stabilization, and reshaping. In *Physics of nonlinear optics*; He, G. S., Ed.; World Scientific: Singapore, 1999.

69. Sutherland, R. L. Elements of the theory of nonlinear optics. In *Handbook of nonlinear optics*, 2nd ed.; Marcel Dekker: New York, 2003, pp 1–34.

70. Perry, J. W. Organic and metal–containing reverse saturable absorbers for optical limiters. In *Nonlinear optics of organic molecules and polymers*; Nalwa, H.S.; Miyata, S. Eds.; CRC Press, 1996.

71. Barkana, Y.; Belkin, M. Laser eye injuries. *Surv. Ophthalmol.* **2000**, *44*, 459–478.

72. Sutherland, R. L. Nonlinear absorption. In *Handbook of nonlinear optics*, 2nd ed.; Marcel Dekker: New York, 2003, pp 579–626.

73. Sanusi, K.; Amuhaya, E. K; Nyokong, T. Enhanced optical limiting behavior of an indium phthalocyanine-single-walled carbon nanotube composite: an investigation of the effects of solvents. *J. Phys. Chem. C* **2014**, *118*, 7057–7069.

74. Mkhize, C.; Britton, J.; Nyokong, T. Enhanced nonlinear optical properties of octa–substituted lead and cadmium phthalocyanines when embedded in poly(bisphenol A carbonate) as thin films. *Polyhedron* **2014**, *81*, 607–613.

75. Calvete, M.; Yang, G. Y.; Hanack, M. Porphyrins and phthalocyanines as materials for optical limiting. *Synth. Met.* **2004**, *141*, 231–243.

76. Hollins, R. Materials for optical limiters. *Curr. Opin. Solid State Mater. Sci.* **1999**, *4*, 189–196.

77. de la Torre, G.; Torres, T.; Agulló-López, F. The phthalocyanine approach to second harmonic generation. *Adv. Mater.* **1997**, *9*, 265–269.

78. de la Torre, G.; Vazquez, P.; Agullo-Lopez, F.; Torres, T. Role of structural factors in the nonlinear optical properties of phthalocyanines and related compounds. *Chem. Rev*. **2004**, *104*, 3723–3750.

79. Mathews, S.; Chaitanya Kumar, S; Giribabu, L.; Venugopal Rao, S. Large third-order optical nonlinearity and optical limiting in symmetric and unsymmetrical phthalocyanines studied using Z-scan. *Opt. Commun*. **2007**, *280*, 206–212.

80. Kulyk, B.; Taboukhat, S.; Akdas-Kiliq, H.; Fillaut, J. -L.; Boughaleb, Y.; Sahraoui, B. Nonlinear refraction and absorption activity of dimethylaminostyryl substituted BODIPY dyes. *RSC Adv*. **2016**, *6*, 84854–84859.

81. Kulyk, B.; Taboukhat, S.; Akdas-Kilig, H.; Fillaut, J. -L.; Karpierz, M.; Sahraoui, B. Tuning the nonlinear optical properties of BODIPYs by functionalization with dimethylaminostyryl substituents. *Dyes Pigm*. **2017**, *137*, 507–511.

82. Zheng, Q.; He, G. S.; Prasad, P. N.; A novel near IR two-photon absorbing chromophore: Optical limiting and stabilization performances at an optical communication wavelength. *Chem. Phys. Lett.* **2009**, *475*, 250–255.

83. Frenette, M.; Hatamimoslehabadi, M.; Bellinger-Buckley, S.; Laoui, S.; La, J.; Bag, S.; Mallidi, S.; Hasan, T.; Bouma, B.; Yelleswarapu, C.; Rochford, J. Shining light on the dark side of imaging: excited state absorption enhancement of a bis-styryl BODIPY photoacoustic contrast agent. *J. Am. Chem. Soc.* **2014**, *136*, 15853–15856.

84. Bouit, P.; Kamada, K.; Feneyrou, P.; Berginc, G.; Toupet, L.; Maury, O.; Andraud, C. Two-photon absorption-related properties of functionalized BODIPY dyes in the infrared range up to telecommunication wavelengths. *Adv. Mater.* **2009**, *21*, 1151–1154.

85. Potamianos, D.; Giannakopoulou, P.; Kaloudi-Chantzea, A.; Pistolis, G.; Couris, S. Third-order nonlinear optical properties of some novel BODIPYs. In: Proceedings of the 16th international conference on transparent optical networks (ICTON). Graz, Austria: IEEE; **2014**.

86. Zhu, M.; Yuan, M.; Liu, X.; Ouyang, C.; Zheng, H.; Yin, X.; Zuo, Z.; Liu, H.; Li, Y. Efficient tuning nonlinear optical properties: synthesis and characterization of a series of novel

poly(aryleneethynylene)s co-containing BODIPY. *J. Polym. Sci. A. Polym. Chem.* **2008**, *46*, 7401–7410.

87. Wang, J.; Hernandez, Y.; Lotya, M.; Coleman, J.; Blau, W. Broadband nonlinear optical response of graphene dispersions. *Adv. Mater*. **2009**, *21*, 2430–2435.

88. Band, Y. Optical properties and applications of reverse saturable absorbers. In *Methods of laser spectroscopy*; Prior, Y. et al Eds.; Plenum Press: New York, 1986; pp 117–121.

89. Sheik–Bahae, M.; Said, A. A.; Van Stryland, E. W. High-sensitivity, single-beam n_2 measurements. *Opt. Lett.* **1989**, *14*, 955–957.

90. Sheik–Bahae, M.; Said, A. A.; Wei, T.; Hagan, D. J.; Van Stryland, E. W. Sensitive measurement of optical nonlinearities using a single beam. *IEEE J. Quant. Electron*. **1990**, *26*, 760 – 769.

91. Van Stryland, E. W.; Sheik–Bahae, M. Z–scan measurements of optical nonlinearities. In *Characterization Techniques and Tabulations for Organic Nonlinear Materials*; Kuzyk, M. G.; Dirk, C. W. Eds.; Marcel Dekker, 1998; pp 655–692.

92. Tsigaridas, G.; Polyzos, I.; Persephonis, P.; Giannetas, V. A novel approach for analyzing open Z–scan experiments. *Optics Commun.* **2006**, *266*, 284–289.

93. Sutherland, R. L. Optical properties of selected third order nonlinear optical materials. In *Handbook of nonlinear optics*, 2nd ed.; Marcel Dekker: New York, 2003, pp 499–578.

94. Chen, Y.; Hanack, M.; Araki, Y.; Ito, O. Axially modified phthalocyanines and naphthalocyanines for optical limting. *Chem. Soc. Rev.* **2005**, *34*, 517–529.

95. García-Frutos, E.; O'Flaherty, S.; Maya, E.; de la Torre, G.; Blau, W.; Vázqueza, P.; Torres, T. Alkynyl substituted phthalocyanine derivatives as targets for optical limiting. *J. Mater. Chem*. **2003**, *13*, 749–753.

96. Dini, D.; Hanack, M. Physical properties of phthalocyanine-based materials. In *the Porphyrin Handbook*; Kadish, K. M.; Smith, K. M.; Guilard, R. Eds.; Academic Press: USA, 2003; pp 22–31.

97. Chen, Y.; Gao, L.; Feng, M.; Gu, L.; He, N.; Wang, J.; Araki, Y.; Blau, W. J.; Ito, O. Photophysical and optical limiting properties of axially modified phthalocyanines. *Mini. Rev. Org. Chem*. **2009**, *6*, 55–65.

98. Matthes, R. Int. Comm. Non-ionizing Radiat. Protection. Revision of guidelines on limits of exposure to laser radiation of wavelengths between 400 nm and 1.4 µm. *Health Phys*. **2000**, *79*, 431–440.

99. Doyle, J.; Wang, J.; O'Flaherty, S.; Chen, Y.; Slodek, A.; Hegarty, T.; Carpenter, L.; Wöhrle, D.; Hanack, M.; Blau, W. Nonlinear optical performance of chemically tailored phthalocyanine–polymer films as solid-state optical limiting devices. *J. Opt. A* **2008**, *10*, 075101.

100. Sekhosana, K. E.; Amuhaya, E.; Nyokong, T. Nanosecond nonlinear optical limiting properties of new trinuclear lanthanide phthalocyanines in solution and as thin films. *Polyhedron* **2015**, *85*, 347–354.

101. Kololuoma, T.; Oksanen, J. A. I.; Raerinne, P.; Rantala, J. T. Dye-doped sol-gel coatings for near-infrared laser protection. *J. Mater. Res*. **2001**, *16*, 2186–2188.

102. Gaussian 09, Revision D.01, Frisch, M. J.; Trucks, G. W.; Schlegel, H. B.; Scuseria, G. E.; Robb, M. A.; Cheeseman, J. R.; Scalmani, G.; Barone, V.; Mennucci, B.; Petersson, G. A.; Nakatsuji, H.; Caricato, M.; Li, X.; Hratchian, H. P.; Izmaylov, A. F.; Bloino, J.; Zheng, G.; Sonnenberg, J. L.; Hada, M.; Ehara, M.; Toyota, K.; Fukuda, R.; Hasegawa, J.; Ishida, M.; Nakajima, T.; Honda, Y.; Kitao, O.; Nakai, H.; Vreven, T.; Montgomery, J. A. Jr.; Peralta, J. E.; Ogliaro, F.; Bearpark, M.; Heyd, J. J.; Brothers, E.; Kudin, K. N.; Staroverov, V. N.; Keith, T.; Kobayashi, R.; Normand, J.; Raghavachari, K.; Rendell, A.; Burant, J. C.; Iyengar, S. S.; Tomasi, J.; Cossi, M.; Rega, N.; Millam, J. M.; Klene, M.; Knox, J. E.; Cross, J. B.; Bakken, V.; Adamo, C.; Jaramillo, J.; Gomperts, R.; Stratmann, R. E.; Yazyev, O.; Austin, A. J.; Cammi, R.; Pomelli, C.; Ochterski, J. W.; Martin, R. L.; Morokuma, K.; Zakrzewski, V. G.; Voth, G. A.; Salvador, P.; Dannenberg, J. J.; Dapprich, S.; Daniels, A. D.; Farkas, O.; Foresman, J. B.; Ortiz, J. V.; Cioslowski, J.; Fox, D. J. Gaussian, Inc., Wallingford CT, 2013.

103. Avogadro: an open-source molecular builder and visualization tool. Version 1.1.1. http://avogadro.openmolecules.net/

104. Hanwell, M. D.; Curtis, D. E.; Lonie, D. C.; Vandermeersch, T.; Zurek, E.; Hutchinson, G. R. Avogadro: an advanced semantic chemical editor, visualization, and analysis platform. *J. Cheminform.* **2012**, *4*, 1–17.

105. Brouwer, A. M. Standards for photoluminescence quantum yield measurements in solution (IUPAC Technical Report). *Pure Appl. Chem.* **2011**, *83*, 2213–2228.

106. Ogunsipe, A.; Chen, J.; Nyokong, T. Photophysical and photochemical studies of zinc(II) phthalocyanine derivatives – effects of substituents and solvents. *New. J. Chem.* **2004**, *28*, 822–827.

107. Jiang, X.; Lo, P.; Yeung, S.; Fong, W.; Ng, D. A pH-responsive fluorescence probe and photosensitizer based on a tetraamino silicon(IV) phthalocyanine. *Chem. Commun.* **2010**, *46*, 3188–3190.

108. Lau, J. Towards dual and targeted cancer therapy with novel phthalocyanine-based photosensitizers. In *Springer Theses*; Springer, 2013, pp 35–48.

109. Magde, D.; Wong, R.; Seybold, P. Fluorescence quantum yields and their relation to lifetimes of Rhodamine 6G and fluorescein in nine solvents: improved absolute standards for quantum yields. *Photochem. Photobiol.* **2002**, *74*, 327–334.

110. Kubin, R.; Fletcher, A. Fluorescence quantum yields of some rhodamine dyes. *J. Lumin.* **1982**, *27*, 455–462.

111. O'Connor, D. Basic principles of the single photon counting lifetime measurement. In *Time-correlated single photon counting*; Academic Press: London, 1984, pp 36–54.

112. Wahl, M. PicoQuant. Time-correlated single photon counting. http://www.picoquant.com/images/uploads/page/files/7253/technote_tcspc.pdf PicoQuant Technical Note **2014** (accessed March 18, 2017).

113. Chen, R.; Wu, R.; Zhang, G.; Gao, Y.; Xiao, L.; Jia, S. Electron transfer-based single molecule fluorescence as a probe for nano-environment dynamics. *Sensors* **2014**, *14*, 2449–2467.

114. Becker, W.; Bergmann, A.; Hink, M.; Konig, K.; Benndorf, K.; Biskup, C. Fluorescence lifetime imaging by time-correlated single-photon counting. *Microsc. Res. Tech.* **2004**, *63*, 58–66.

115. Becker, W. Optical signal recording. In *Advanced time-correlated single photon counting techniques*; Springer, 2005, pp 1–9.

116. Ogbodu, R. O. Photophysicochemical properties and *in vitro* photodynamic therapy activities of zinc phthalocyanine conjugates with biomolecules and single-walled carbon nanotubes. Ph.D. Dissertation, Rhodes University, 2015.
117. Ogbodu, R.; Antunes, E.; Nyokong, T. Physicochemical properties of zinc monoamino pthalocyanine conjugated to folic acid and single walled carbon nanotubes. *Polyhedron* **2013**, *60*, 59–67.
118. Carloni, P.; Damiani, E.; Greci, L.; Stipa, P.; Tanfani, F.; Tartaglini, E.; Wozniak, M. On the use of 1,3-diphenylisobenzofuran (DPBF). Reactions with carbon and oxygen centered radicals in model and natural systems. *Res. Chem. Intermediat*. **1993**, *19*, 395–405.
119. Lau, J.; Lo, P.; Fong, W.; Ng, D. A zinc(II) phthalocyanine conjugated with an oxaplatin derivative for dual chemo- and photodynamic therapy. *J. Med. Chem.* **2012**, *55*, 5446–5454.
120. Maree, S; Nyokong, T. Syntheses and photochemical properties of octasubstituted phthalocyaninato zinc complexes. *J. Porphyrins Phthalocyanines* **2001**, *5*, 782–792.
121. Kuznetsova, N.; Gretsova, N.; Kalmykova, E.; Makarova, E.; Dashkevich, S.; Negrimovskii, V.; Kaliya, O.; Luk'yanets, E. Relationship between the photochemical properties and structure of pophyrins and related compounds. *Russ. J. Gen. Chem.* **2000**, *70*, 133–140.
122. Ogunsipe, A.; Maree, D.; Nyokong, T. Solvent effects on the photophysical and fluorescence properties of zinc phthalocyanine derivatives. *J. Mol. Struct.* **2003**, *650*, 131–140.
123. Spiller, W.; Kliesch, H.; Wohrle, D.; Hackbarth, S.; Roder, B.; Schnurpfeil, G. Singlet oxygen quantum yields of different photosensitizers in polar solvents and micellar solutions. *J. Porphyrins Phthalocyanines* **1998**, *2*, 145–158.
124. Gandra, N.; Frank, A.; Gendre, O.; Sawwan, N.; Aebisher, D.; Liebman, J.; Houk, K.; Greer, A.; Gao, R. Possible singlet oxygen generation from the photolysis of indigo dyes in methanol, DMSO, water, and ionic liquid, 1-butyl-3-methylimidazolium tetrafluoroborate. *Tetrahedron* **2006**, *62*, 10771–10776.
125. Neckers, D. C. Rose Bengal. *J. Photochem. Photobiol. A* **1989**, *47*, 1–29.

126. Harris, J.; Gai, L.; Mack, J.; Nyokong, T.; Shen, Z. Optical limiting properties of 2-thiophene substituted distyrylBODIPY dyes at 532 nm. To be submitted to *New J. Chem.* in **2017**.

127. Algi, M.; Tirkes, S.; Ertan, S.; Ergun, E.; Cilhaner, A.; Algi, F. Design and synthesis of new 4,4'-difluoro-4-bora-3a,4a-diaza-*s*-indacene based electochromic polymers. *Electrochim. Acta* **2013**, *109*, 766–774.

128. Zhou, Z.; Yang, W. Syntheses of 2-aryl benzothiazoles *via* photoinduced oxidative condensation of amines with 2-aminophenol in the presence of BODIPY derivatives. *Synth. Commun*. **2014**, *44*, 3189–3198.

129. Gottlieb, H.; Kotlyar, V.; Nudelman, A. NMR Chemical shifts of common laboratory solvents as trace impurities. *J. Org. Chem.* **1997**, *62*, 7512–7515.

130. Fulmer, G.; Miller, A.; Sherden, N.; Gottlieb, H.; Nudelman, A.; Stoltz, B.; Bercaw, J.; Goldberg, K. NMR Chemical shifts of trace impurities: common laboratory solvents, organics, and gases in deuterated solvents relevant to the organometallic chemist. *Organomettalics* **2010**, *29*, 2176–2179.

131. Gunther, H. The proton magnetic resonance spectra of organic molecules – chemical shift and spin-spin coupling. In *NMR Spectroscopy: basic principles, concepts and applications in chemistry*, 3rd ed.; Wiley-VCH: Germany, 2013; pp 37–40.

132. Jackman, L. M.; Sternhell, S. General applications: Hydrogen exchange and hydrogen bonding. In *Applications of nuclear magnetic resonance spectroscopy in organic chemistry*, 2nd ed.; Pergamon: Oxford, 1969; p 359.

133. Pinto, D.; Santos, C.; Silva, A. Advanced NMR techniques for structural characterization of heterocyclic structures. In *Recent research developments in heterocyclic chemistry*; Pinho, T. Ed.; Research Signpost: Trivandrum, India, 2007; pp 398–475.

134. Abraham, R.; Byrne, J.; Griffiths, L.; Perez, M. ^{1}H chemical shifts in NMR: Part 23, the effect of dimethyl sulphoxide *versus* chloroform solvent on ^{1}H chemical shifts. *Magn. Reson. Chem.* **2006**, *44*, 491–509.

135. Dini, D.; Barthel, M.; Hanack, M. Phthalocyanines as active materials for optical limiting. *Eur. J. Org. Chem.* **2001**, *20*, 3759–3769.

136. Ortiz, A.; Insuasty, B.; Torres, R. M.; Herranz, M. A.; Martin, N.; Viruela, R.; Orti, E. Aminopyrimidine-based donor–acceptor chromophores: push–pull versus aromatic behavior. *Eur. J. Chem.* **2008**, 99–108.

137. Marder, S. R.; Beratan, D. N.; Cheng, L. -T. Approaches for optimizing the first electronic hyperpolarizability of conjugated organic molecules. *Science* **1991**, *252 (5002)*, 103.

138. Sutherland, R. L. Characterization of second order nonlinear optical materials. In *Handbook of nonlinear optics*, 2nd ed.; Marcel Dekker: New York, 2003, pp 241–294.

139. Chen, Y.; Hanack, M.; Blau, W.; Dini, D.; Liu, Y.; Lin, Y.; Bai, J. Soluble axially substituted phthalocyanines: synthesis and nonlinear optical response. *J. Mater. Sci.* **2006**, *41*, 2169–2185.

140. Britton, J.; Litwinski, C.; Antunes, E.; Durmuş, M.; Chaukea, V.; Nyokong, T. Optical limiting analysis of phthalocyanines in polymer thin films. *J. Macromol. Sci., A* **2013**, *50*, 110–120.

141. Shi, M.; Tian, J.; Mkhize, C.; Kubheka, G.; Zhou, J.; Mack, J.; Nyokong, T.; Shen, Z. Synthesis, characterization and photodynamic therapy properties of an octa-4-tert-butylphenoxy-substituted phosphorous(V) triazatetrabenzcorrole. *J. Porphyrins Phthalocyanines* **2014**, *18*, 698–707.

142. Kobayashi, N.; Muranaka, A.; Mack, J. Michl's Perimeter Model in MCD Spectroscopy. *In Circular Dichroism and Magnetic Circular Dichroism Spectroscopy for Organic Chemists*. Royal Society of Chemistry, 2012, pp 172–191.

143. Waluk, J.; Michl, J. The perimeter model and magnetic circular dichroism of porphyrin analogues. *J. Org. Chem.* **1991**, *56*, 2729–2735.

144. Wang, S.; Liu, H.; Mack, J.; Tian, J.; Zou, B.; Lu, H.; Li, Z.; Jiang, J.; Shen, Z. A BODIPY-based 'turn-on' fluorescent probe for hypoxic cell imaging. *Chem. Commun.* **2015**, *51*, 13389–13392.